6. SITE 930[1]

Shipboard Scientific Party[2]

HOLE 930A

Date occupied: 1 April 1994

Date departed: 2 April 1994

Time on hole: 8 hr, 45 min

Position: 5°0.894′N, 47°35.743′W

Bottom felt (drill pipe measurement from rig floor, m): 3155.0

Distance between rig floor and sea level (m): 10.74

Water depth (drill pipe measurement from sea level, m): 3144.3

Penetration (m): 9.50

Number of cores (including cores having no recovery): 1

Total length of cored section (m): 9.50

Total core recovered (m): 10.05

Core recovery (%): 105

Oldest sediment cored:
Depth (mbsf): 9.50
Nature: Silty clay
Earliest age: Pleistocene

HOLE 930B

Date occupied: 2 April 1994

Date departed: 3 April 1994

Time on hole: 1 day, 8 hr, 30 min

Position: 5°0.894′N, 47°35.743′W

Bottom felt (drill pipe measurement from rig floor, m): 3154.3

Distance between rig floor and sea level (m): 10.74

Water depth (drill pipe measurement from sea level, m): 3143.6

Penetration (m): 225.30

Number of cores (including cores having no recovery): 24

Total length of cored section (m): 225.30

Total core recovered (m): 203.24

Core recovery (%): 90

Oldest sediment cored:
Depth (mbsf): 225.30
Nature: Silty clay
Earliest age: Pleistocene

HOLE 930C

Date occupied: 3 April 1994

Date departed: 4 April 1994

Time on hole: 21 hr, 30 min

Position: 5°0.905′N, 47°35.746′W

Bottom felt (drill pipe measurement from rig floor, m): 3154.3

Distance between rig floor and sea level (m): 10.74

Water depth (drill pipe measurement from sea level, m): 3143.6

Penetration (m): 259.00

Number of cores (including cores having no recovery): 18

Total length of cored section (m): 172.60

Total core recovered (m): 135.47

Core recovery (%): 78

Oldest sediment cored:
Depth (mbsf): 259.00
Nature: Silty clay
Earliest age: Pleistocene

HOLE 930D

Date occupied: 4 April 1994

Date departed: 4 April 1994

Time on hole: 13 hr, 30 min

Position: 5°1.005′N, 47°35.747′W

Bottom felt (drill pipe measurement from rig floor, m): 3156.0

Distance between rig floor and sea level (m): 10.71

Water depth (drill pipe measurement from sea level, m): 3145.3

Penetration (m): 51.50

Number of cores (including cores having no recovery): 6

Total length of cored section (m): 51.50

Total core recovered (m): 53.27

Core recovery (%): 103

Oldest sediment cored:
Depth (mbsf): 51.50
Nature: Silty clay
Earliest age: Pleistocene

Principal results: Site 930 (proposed Site AF-21) is located on the upper part of the Amazon Fan, in a slight topographic low formed between the levees of the buried Purple Channel and the recently active Amazon Channel. The primary objectives of this site were the chronology of the middle part of the Upper Levee Complex and the sedimentological and geochemical characterization of levee flank, levee crest, and hemipelagic acoustic facies.

[1]Flood, R.D., Piper, D.J.W., Klaus, A., et al., 1995. *Proc. ODP, Init. Repts.*, 155: College Station, TX (Ocean Drilling Program).

[2]Shipboard Scientific Party is as given in the list of participants in the contents.

The uppermost acoustic unit at this site is the feather edge of the western (left) levee of Amazon/Brown/Aqua (coincident at this location) Channel. Hole 930B also penetrated the underlying flank of the Purple east (right) levee about 20 km east of its corresponding channel and the crest of the Orange east (right) levee about 500 m from its channel axis. Hemipelagic sediment was predicted to overlie the Orange levee and underlie the Purple at this location. The water depth of 3144 m is well above the regional lysocline.

The site was selected from seismic profile C2514 at 0300UTC on 2 Dec. A 6-hr seismic survey was run from the *JOIDES Resolution* to precisely locate the site. The 3.5-kHz echosounder profiles show that sediment waves are present in the uppermost 30 to 35 m of the sediment column. They have an east-west orientation, heights of 1 to 4 m, and spacings of 200 to 1000 m (average 600 m).

Hole 930A overshot the mud line by 1.75 m, penetrated 9.5 m, and recovered 10.05 m.

Hole 930B cored 5.7 m below the mud line in Core 930B-1H. Advanced piston corer (APC) coring was continued to Core 930B-11H. We switched to extended core barrel (XCB) coring to recover Cores 930B-12X through -23X, with total depth (TD) at 225.3 m. No sediment was recovered in Core 930B-12X. Total recovery at Hole 930B was 203.20 m (90.2% recovery).

Advanced piston corer heat-flow coring shoe (ADARA) temperature measurements were made on Cores 930B-6H (53.2 mbsf) and -8H (72.2 mbsf), and the water sampler and temperature probe (WSTP) was used before Cores 930B-12X (100.7 mbsf) and -17X (148.7 mbsf), indicating a geothermal gradient of 31°C/km. There was gas expansion in all cores, but this was most severe in Cores 930B-2H through -4H. Methane abundance was greatest in Cores 930B-2H and -4H, with concentrations of 8000 ppm in headspace samples, and then decreased downhole. Only trace amounts of ethane were detected.

Hole 930C was offset 20 m to the north. It was designed to resample intervals in which important paleontological markers had been identified. We washed to 29.0 mbsf, APC cored to 95.5 mbsf, XCB cored to 143.7 mbsf, washed to 201.1 mbsf, and then XCB cored to TD at 259.0 m. Total recovery was 135.47 m (78.5%).

Holes 930A, B, and C were all located on the downslope flank of a sediment wave. Hole 930D was offset 185 m to the north of Hole 930C, to sample the adjacent sediment wave crest. We APC cored to a TD of 51.5 m. Total recovery was 53.27 m (103.4%).

Three lithologic units are recognized:

Unit I (0–1.65 mbsf) is a Holocene nannofossil- and foraminifer-rich clay with about 30% carbonate content. It represents deposition since the early Holocene rise in sea level, which caused the retreat of the Amazon River mouth landward across the continental shelf.

Unit II (1.65–188.42 mbsf) consists of mud with interbedded laminae and thin beds of silt and very fine sand. The mud has about 2% carbonate content. Subunit IIA (1.65–9.64 mbsf) comprises color-banded and mottled mud of latest Pleistocene to early Holocene age. Subunit IIB (9.64–43.00 mbsf) consists of mud with thin beds and laminae of silt and silty sand. It was deposited on the levee flank of the latest Pleistocene Amazon channel system and shows sedimentary structures suggesting that the subunit consists largely of overbank turbidites. Rare thin disrupted zones with slightly elevated bulk density and strength suggest local slump deposits. Individual beds can be correlated from Hole 930B on the flank of a sediment wave to Hole 930D on the adjacent crest, where the overall section is thicker and the proportion of sand is higher. Subunit IIC (43.00–66.65 mbsf) is lithologically similar to Subunit IIA and corresponds to times when the Purple Channel was active. Subunit IID (66.65–188.42 mbsf) is lithologically similar to Subunit IIB and largely corresponds to the levee crest of the former Orange Channel of the Amazon Fan. Between 110 mbsf and 180 mbsf there is a steady increase in grain density from 2.71 to 2.78 g/cm^3 that does not correlate with grain size changes and thus may indicate a change in clay mineralogy.

Unit III (188.42 242.90 mbsf) comprises muddy sand with "floating" pebble clasts, abundant plant debris, and mud clasts interbedded with thick overconsolidated clay sequences. The clays contain mixed foraminiferal faunas including cool interstadial planktonic assemblages and upper slope benthic foraminifers. High total S (1.0%) and N (0.2%) occurs in the clay, and one pore-water sample showed unusual characteristics including low chlorinity. It is unclear whether Unit III is a single debris-flow deposit, or represents several flows separated by discrete slide blocks (olistoliths).

Foraminifer abundances are low below Unit IIC, and biostratigraphic age picks are tentative. *P. obliquiloculata* is present below 137 mbsf, suggesting an age >40 ka. No evidence was found for faunas of prior interglacials except in reworked blocks in the Unit III debris-flow deposit. A distinctive magnetic excursion at about 90 mbsf in both Hole 930B and 930C is interpreted as the Lake Mungo Excursion (≈30 ka). Subunit IIC may show secular variation in natural remanent magnetization with about 15 small inclination cycles grouped in three larger cycles over 35 m. Overall sedimentation rate in Unit II is probably 4–5 m/k.y.

Pore-water profiles show rapid concentration changes in the upper 20 mbsf, including complete sulfate reduction by 13 mbsf, and suggest precipitation of carbonate and phosphate, that may be represented in part by vivianite spherules. Total organic carbon in Unit II is about 0.8% with a slight decrease downcore.

The preliminary data from Site 930 suggest that the Amazon Fan aggraded at an extremely rapid rate. Much of the exposed Upper Levee Complex of the Amazon Fan appears to date from the last glacial period (oxygen isotopic Stages 2–4). The fan contains an expanded record of foraminifers, which with shore-based studies will provide an isotope stratigraphy and paleoecological interpretation. Detrital pollen is sufficient for shore-based studies of climatic change in the Amazon Basin. There is considerable lithologic variability within acoustically defined stratigraphic units, which suggests that changes in sea level, Amazon River discharge, and levee growth patterns all may influence sediment facies development within individual channel-levee complexes.

SETTING AND OBJECTIVES

Introduction

Site 930 (proposed Site AF-21) provided one of the biostratigraphic sections for the timing of Amazon Fan depositional units. It also provided information on a range of acoustic facies. Levee flank sediment at relatively shallow depths on the fan was sampled to contrast with levee crest sediment to be drilled later in the leg. Replicate coring was planned for the expected hemipelagic section to minimize gaps and to provide enough sediment to extract microfossils. (We use the term "hemipelagic" in a loose sense throughout this volume to refer to terrigenous sediment forming relatively thin sequences that are not well resolved on seismic profiles and lack the prominent reflection architecture associated with turbidites. Corresponding cored sediment consists predominantly of clay with few foraminifers and nannofossils, but with more of an abundance than in lithologies with abundant silt turbidites.) Site 930 was chosen as our first hole on the Amazon Fan to give an indication of the ages and coring conditions that we might expect at other sites.

Setting

Site 930 (Fig. 1) is located on the crest of the buried Orange levee, 10 km west of the active Amazon Channel in a slight topographic low formed between the Purple and Amazon levees. This low extends 50 km upslope to the site of the Purple-Amazon channel avulsion. Site 930 lies just upstream from the major left (following normal convention, left and right are with respect to the downflow direction) bend of the Amazon Channel at 5°05′N that resulted from the avulsion of the Amazon Channel from the Aqua Channel (Fig. 1). The site was selected on line C2514 at 0300UTC on 2 Dec. 1984 (Fig. 2). Sediment waves are present in the uppermost 30 to 35 m of the sediment column (Fig. 3). The pre-site survey showed that these waves have an east-west orientation with heights of 1 to 4 m, and spacings of 200 to 1000 m (average 600 m).

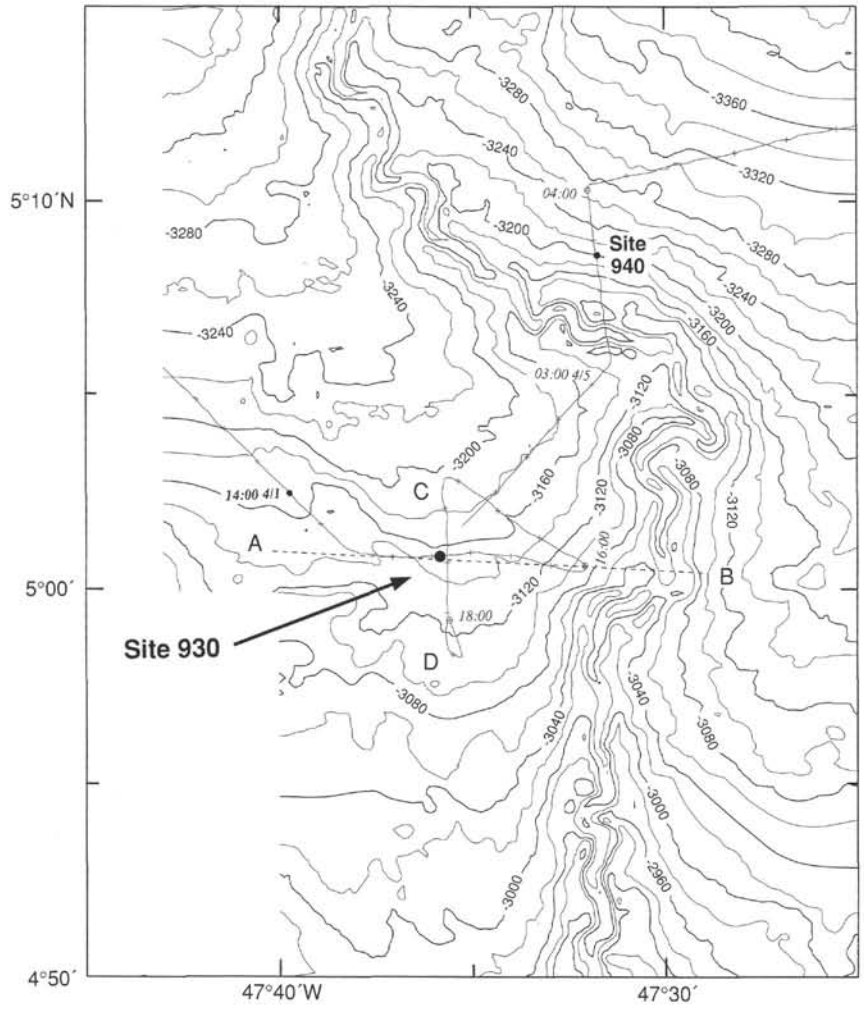

Figure 1. Location of Site 930 showing *JOIDES Resolution* tracks. SeaBeam bathymetry from Flood et al. (1991) in uncorrected meters (v = 1500 m/s). A–B is seismic profile in Fig. 2; C–D is 3.5-kHz profile in Fig. 3.

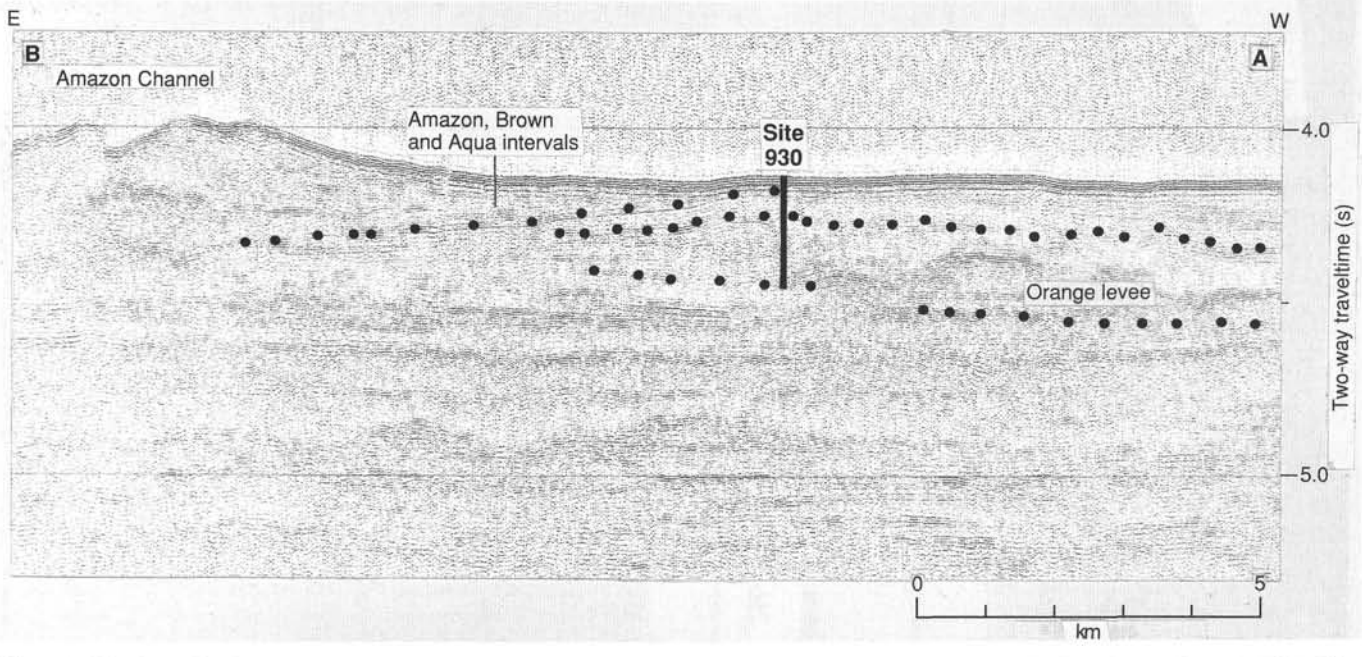

Figure 2. Seismic section through Site 930 showing interpreted correlation within the acoustic stratigraphic framework of Manley and Flood (1988). (Line C2514 at 0230–0355 UTC on 2 Dec. 1984).

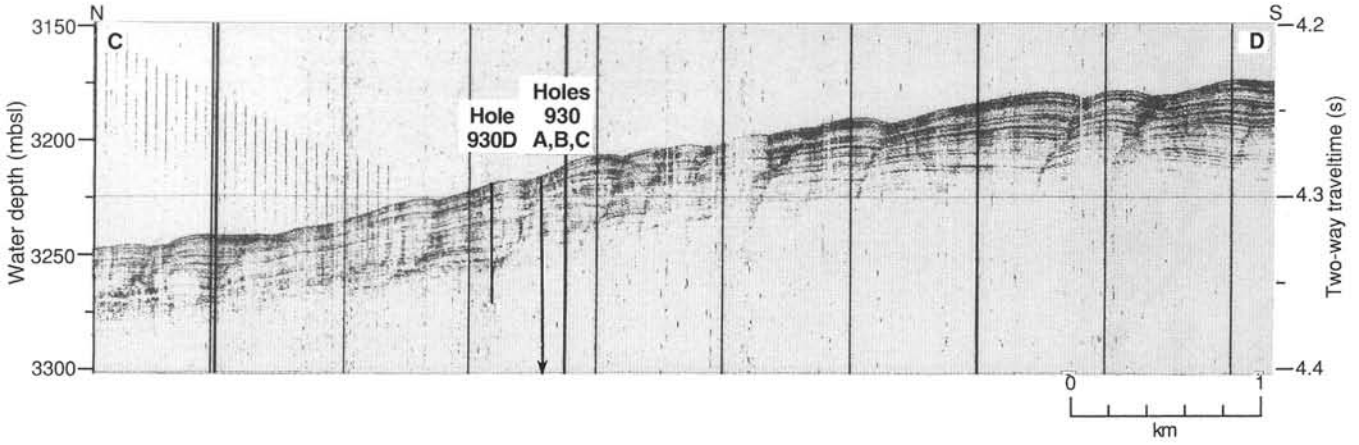

Figure 3. A 3.5-kHz profile through Site 930 showing sediment waves and location of holes. Water depths on this and subsequent profiles are calculated using a sound velocity of 1500 m/s. They thus match the bathymetric maps but do not correspond precisely to water depths measured with the drill string.

The holes penetrate several acoustic units on the fan (Figs. 2 and 3; Table 1 of "Introduction" chapter, this volume). The uppermost unit is the feather edge of the western (left) levee of the Amazon, Brown, and Aqua Channel-levee systems, which are coincident at this location because avulsion took place down-fan. The holes also penetrate the underlying flank of the Purple east (right) levee about 20 km east of its corresponding channel and the crest of the Orange east (right) levee about 500 m from its channel axis. Hemipelagic sediment was predicted to overlie the Orange levee and underlie the Purple at this location. Higher amplitude seismic reflections beyond the base of the drilled sequence may represent a HARP (high-amplitude reflection package of Manley and Flood, 1988). The water depth of 3144 m is well above the regional lysocline.

Objectives

The specific objectives at Site 930 were:

1. To sample the hemipelagic section that lies above the crest of the Orange levee. This section lies above the lysocline and in the center of the fan and should be correlative with the Blue, Yellow, and Channel 5 levees.
2. To sample the flank sediment of the Amazon/Brown/Aqua levee and the Purple levee for sedimentological and stratigraphic studies at a location well up-fan to provide a contrast to holes farther down-fan and near the crests of levees drilled at other sites.
3. To sample the near-crest levee sediment of the Orange levee for sedimentological and stratigraphic studies. The extreme flank sediment of the Orange levee was sampled in deeper water at Site 936.

OPERATIONS

Transit, Barbados to Site 930 (AF-21)

The ship departed Barbados at 1205 on 28 March. All times reported in the "Operations" sections in this volume are reported in local time. During this leg, the local time is UTC – 4 hr. The 848-nmi sea voyage to Site 930 required approximately 91.0 hr at an average speed of 9.3 kt. During the transit, we collected navigation, 3.5- and 12-kHz reflection, and magnetic data.

Site 930 Seismic Survey

The single-channel seismic survey started at 0730 on 1 April and lasted about 6 hr. The seismic gear was retrieved, and the ship returned to the global positioning system (GPS) coordinates 05°00.85′N, 47°35.78′W. The ship was on location in dynamic positioning mode at 1430 hr, and a Datasonics commandable retrievable beacon was dropped at 1515 on 1 April.

Depending on the ship's draft, the distance from sea level to rig floor was 10.74 m for Holes 930A, 930B, and 930C, and 10.71 m for Hole 930D. The 3.5-kHz depth recorder indicated a discontinuous reflector at 3159.4 meters below rig floor (mbrf) and a continuous, strong reflector at 3164.5 mbrf.

Hole 930A

A Polycrystalline Diamond Compact (PDC) APC/XCB bit was attached to monel drill collars and run to the seafloor. The monel drill collars are intended to minimize remagnetization caused by the drill collars, allowing magnetic orientation of the APC cores. Core 1H was taken with the bit at 3155.5 mbrf (3.9 m above the highest reflector), and 10.05 m of sediment was recovered (Table 1). It was interpreted that the core was taken below the mud line (later estimated to be about 1.3 m). Hole 930A was terminated and the bit pulled above the seafloor at 0000 on 2 April.

Hole 930B

The ship was not offset, and the bit was positioned at 3145.5 mbrf. The first attempt to core recovered mostly water and only a trace of clay. The bit was repositioned at 3150.5 mbrf, and Hole 930B was spudded at 0130 hr 2 April. Core 1H recovered 5.7 m; therefore, the seafloor was defined to be 3154.3 mbrf. Mud-line water samples were obtained for paleontology from the muddy water above the top of the sediment. In most of the cores recovered at Site 930, sediment began to extrude from the core liner due to gas expansion once the liner was taken out of the core barrel. Core disturbance was minimized by drilling small holes in nearly all of the core liners to allow gas to escape. During APC coring, several core liners collapsed or were extremely difficult to extract from the core barrel. In some cases this significantly disturbed the recovered sediment.

ADARA heat measurements were performed during Cores 6H and 8H at 53.2 and 72.2 mbsf. Core orientation using the Tensor tool was performed for Cores 4H through 11H. A suspected bad rechargeable battery pack rendered the data useless for Cores 4H through 10H. Non-rechargeable batteries were used for Core 11H and the tool produced good results. Using the APC, we cored 100.7 m, recovering 104.56 m (104% recovery).

Core 11H was a partial stroke (later confirmed to have approximately 2 m of flow-in at the bottom of the core) and required 35,000 lb overpull to extract the core barrel from the formation. We then de-

Table 1. Site 930 coring summary.

Core	Date (1994)	Time (UTC)	Depth (mbsf)	Length cored (m)	Length recovered (m)	Recovery (%)
155-930A-						
1H	April 2	0350	0.0–9.5	9.5	10.05	105.8
Coring totals				9.5	10.1	105.80
155-930B-						
1H	April 2	0555	0.0–5.7	5.7	5.72	100.0
2H	April 2	0650	5.7–15.2	9.5	9.24	97.2
3H	April 2	0735	15.2–24.7	9.5	10.41	109.6
4H	April 2	0740	24.7–34.2	9.5	10.50	110.5
5H	April 2	1045	34.2–43.7	9.5	10.71	112.7
6H	April 2	1200	43.7–53.2	9.5	10.15	106.80
7H	April 2	1255	53.2–62.7	9.5	10.26	108.0
8H	April 2	1410	62.7–72.2	9.5	10.42	109.7
9H	April 2	1510	72.2–81.7	9.5	10.38	109.2
10H	April 2	1610	81.7–91.2	9.5	6.34	66.7
11H	April 2	1730	91.2–100.7	9.5	10.43	109.8
12X	April 2	1940	100.7–110.2	9.5	0.00	0.0
13X	April 2	2035	110.2–119.8	9.6	8.80	91.6
14X	April 2	2140	119.8–129.5	9.7	10.00	103.1
15X	April 2	2230	129.5–139.1	9.6	8.01	83.4
16X	April 2	2325	139.1–148.7	9.6	10.19	106.1
17X	April 3	0135	148.7–158.4	9.7	8.34	86.0
18X	April 3	0240	158.4–168.0	9.6	8.14	84.8
19X	April 3	0335	168.0–177.2	9.2	10.06	109.3
20X	April 3	0445	177.2–186.8	9.6	10.12	105.4
21X	April 3	0600	186.8–196.4	9.6	6.49	67.6
22X	April 3	0745	196.4–206.1	9.7	10.36	106.8
23X	April 3	0935	206.1–215.7	9.6	2.37	24.7
24X	April 3	1105	215.7–225.3	9.6	5.80	60.4
Coring totals				225.3	203.2	90.20
155-930C-						
1H	April 3	1455	29.0–38.5	9.5	10.39	109.3
2H	April 3	1535	38.5–48.0	9.5	10.31	108.5
3H	April 3	1620	48.0–57.5	9.5	10.27	108.1
4H	April 3	1700	57.5–67.0	9.5	10.28	108.2
5H	April 3	1735	67.0–76.5	9.5	10.23	107.7
6H	April 3	1815	76.5–86.0	9.5	10.22	107.6
7H	April 3	1855	86.0–95.5	9.5	10.26	108.0
8X	April 3	2000	95.5–105.1	9.6	7.60	79.1
9X	April 3	2050	105.1–114.7	9.6	5.13	53.4
10X	April 3	2145	114.7–124.4	9.7	8.89	91.6
11X	April 3	2235	124.4–134.0	9.6	8.73	90.9
12X	April 3	2325	134.0–143.7	9.7	8.20	84.5
13X	April 4	0200	201.1–210.8	9.7	4.31	44.4
14X	April 4	0300	210.8–220.4	9.6	7.24	75.4
15X	April 4	0430	220.4–230.1	9.7	3.07	31.6
16X	April 4	0645	230.1–239.7	9.6	7.14	74.4
17X	April 4	0745	239.7–249.4	9.7	3.20	33.0
18X	April 4	0845	249.4–259.0	9.6	0.00	0.0
Coring totals				172.6	135.5	78.50
155-930D-						
1H	April 4	1245	0.0–4.0	4.0	4.03	101.0
2H	April 4	1335	4.0–13.5	9.5	8.70	91.6
3H	April 4	1425	13.5–23.0	9.5	10.34	108.8
4H	April 4	1510	23.0–32.5	9.5	9.95	105.0
5H	April 4	1550	32.5–42.0	9.5	10.10	106.3
6H	April 4	1635	42.0–51.5	9.5	10.15	106.8
Coring totals				51.5	53.3	103.40

Note: An expanded version of this coring summary table that includes lengths and depths of sections, location of whole-round samples, and comments on sampling disturbance is included on the CD-ROM in the back pocket of this volume.

cided to switch to the XCB coring method. Prior to the first XCB core, the first WSTP temperature was obtained at 100.7 m.

XCB Cores 12X through 24X were taken from 3255.0 to 3379.6 mbrf (100.7–225.3 mbsf) with 124.6 m cored and 97.18 m recovered (78.0% recovery). The first XCB core, Core 12X, apparently was washed away due to circulating seawater at 200 gpm (a low pump rate considering the sticky nature of the formation and its tendency to plug the nozzles in the bit). Subsequent cores were cut using a circulation rate of 100 gpm or less until it took more than 25 min to cut at about 190 m. No hole problems were encountered. Coring was terminated at 225.3 mbsf when the geological objectives were met. Hole 930B officially ended when the bit cleared the seafloor at 0832, 3 April.

Hole 930C

The ship was moved 20 m north, and Hole 930C was spudded at 0925 hr 3 April. The mud line was assumed to be 3154.3 mbrf, and the hole was drilled ahead, without coring, to 3183.3 mbrf (29.0 mbsf). APC Cores 1H through 7H were taken from 3183.3 to 3249.8 mbrf (29.0 95.5 mbsf) with 66.5 m cored and 71.96 m recovered (108.2% recovery). In an effort to reduce APC core disturbance due to flow-in, XCB Cores 8X through 12X were taken from 3249.8 to 3298.0 mbrf (95.5 143.7 mbsf) with 48.2 m cored and 38.73 m recovered (80.3% recovery).

Based on interesting paleontological results at the base of Hole 930B, Hole 930C was drilled (without coring) from 3249.8 to 3355.4 mbrf (143.72–201.1 mbsf), and XCB coring resumed at 201.1 mbsf. XCB Cores 13X through 18X were taken from 3355.4 to 3413.3 mbrf (201.1–259.0 mbsf) with 57.9 m cored and 24.96 m recovered (43.1% recovery). The XCB recovery for Hole 930C was 66.3%. The combined APC/XCB recovery for Hole 930C was 78.6%. Hole 930C was terminated, and the bit was pulled above the seafloor at 0600 hr 4 April.

Hole 930D

The ship was moved 186 m north of Hole 930C. The precision depth recorder (PDR) indicated a water depth of 3161.4 mbrf. The bit was positioned at 3150.5 mbrf, and Hole 930D was spudded at 0600 hr 4 April. The recovery from Core 1H was 4.03 m. The water depth is therefore defined as 3156.0 mbrf. APC Cores 1H through 6H were taken from 3156.0 to 3207.5 mbrf (0–51.5 mbsf) with 51.5 m cored and 53.27 m recovered (103.4% recovery). Hole 930D was terminated, and the bit was pulled above the seafloor at 1315 hr 4 April. The bit cleared the rig floor at 1930 hr 4 April, officially ending Site 930.

LITHOSTRATIGRAPHY

Introduction

Four holes were drilled at Site 930, reaching a maximum depth of 249.4 mbsf in Hole 930B. The composite column illustrating the lithostratigraphy (Figs. 4 and 5) incorporates data from Hole 930B for the intervals 0–100.7 mbsf and 110.2–210 mbsf (Core 930B-12X recovered no sediment), and from Hole 930C for the intervals 105.1–110.0 mbsf and from 210.8 mbsf to the base of the column. Incomplete recovery in both holes between 100 and 114 mbsf prevents determination of the lithology at these depths. There is substantial duplication of the section from the seafloor to 140 mbsf between Holes 930B and 930C. The duplication of the upper 50 m between Holes 930B and 930D provides a comparison of deposition on the upslope and downslope flanks of the sediment waves that characterizes the levee at this site (see "Setting and Objectives" section, this chapter). All of the sediment at this site is of late Quaternary age. Expansion of methane gas during core recovery commonly affected the sediment by disrupting the primary sedimentary structures in many silt and sand beds and by producing void spaces within many of the core sections (see "Lithostratigraphy" section, "Explanatory Notes" chapter, this volume).

Description of Lithostratigraphic Units

Unit I

Intervals: 155-930B-1H-1, 0–55 cm; 155-930D-1H-1, 0–68 cm
Age: Holocene
Depth: 0.00–0.55 mbsf

Unit I consists of a brown (10YR 5/3) calcareous clay containing foraminifers and nannofossils from 0.00 to 0.42 mbsf, overlying a

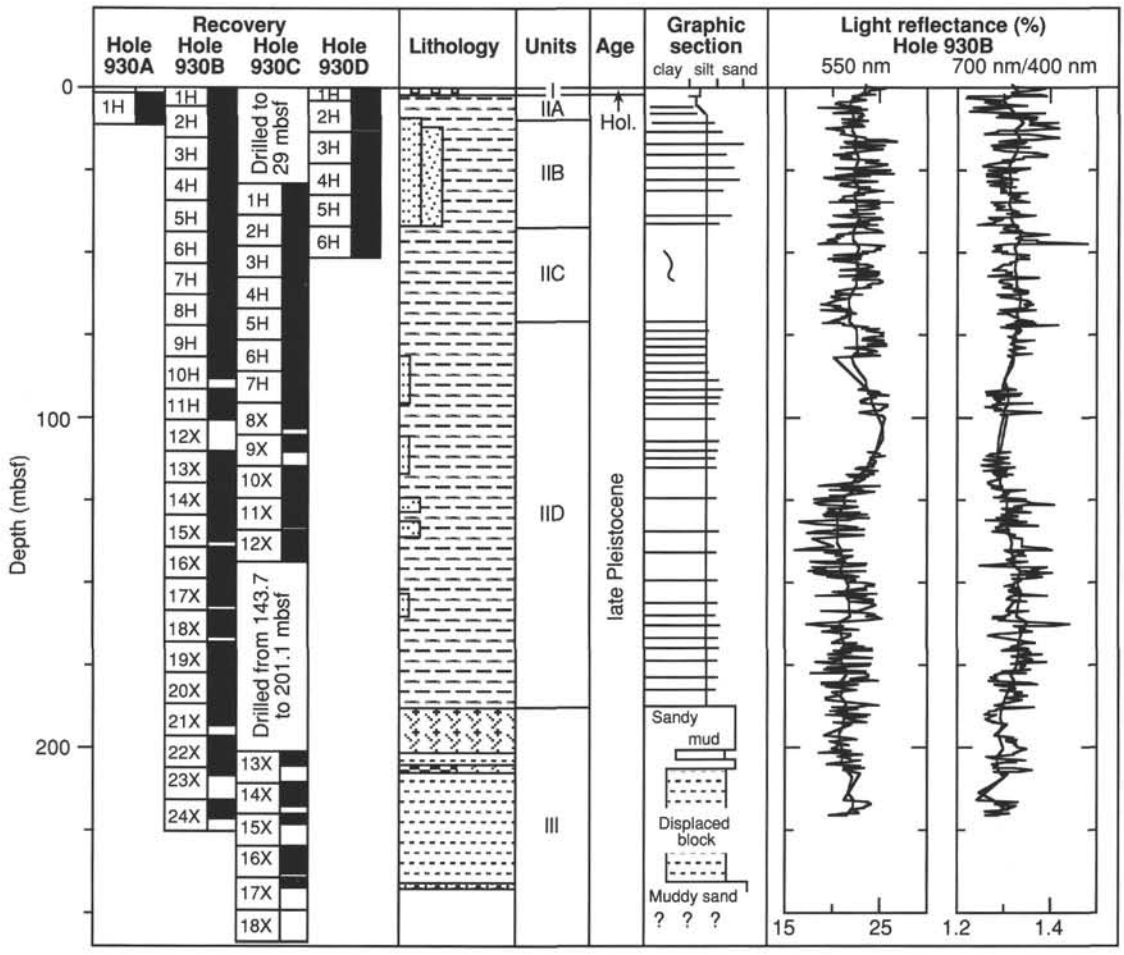

Figure 4. Composite stratigraphic section for Site 930 showing core recovery in all holes, a simplified summary of lithology, depths of unit boundaries, age, a graphic section with generalized grain size and bedding characteristics, and downhole variations in light-reflectance values for Hole 930B only. The lithologic symbols are explained in Figure 1 of the "Explanatory Notes" chapter, this volume.

gray (5Y 5/1) nannofossil- and foraminifer-rich clay at 0.55 mbsf (Figs. 5 and 6). The top of the unit was not recovered in Hole 930A; therefore, Unit I is defined from the interval recovered in Hole 930B; in Hole 930D, the same transition is found at 0.68 mbsf. The base of Unit I in both holes is taken as the transition from nannofossil-rich clay to an olive gray (5Y 3/2 to 5GY 3/2) silty clay with low carbonate content (see "Organic Geochemistry" section, this chapter). Carbonate is slightly more than 30% in the upper 0.42 m but is generally less than 4.5% below. The unit commonly shows burrow mottling. A distinctive, diagenetic, reddish brown (10YR 4/3) iron-rich crust occurs in the interval 930B-1H-1, 42–45 cm (Fig. 6; 0.42–0.45 mbsf). Similar iron-rich crusts were analyzed previously and correlated throughout the Amazon Fan and adjacent Guiana Basin (e.g., Damuth, 1977; see "Introduction" chapter, this volume), and were recovered in most other Leg 155 holes.

Unit II

Intervals: 155-930A-1H; 155-930B-1H-1, 55 cm, through -21X-2, 12 cm; 155-930C-1H through -12X-CC; 155-930D-1H-1, 68 cm, through -6H-CC

Age: Holocene to late Pleistocene (the Holocene includes only the uppermost 50 cm of this unit; see "Biostratigraphy" section, this chapter)

Depth: 0.55–188.42 mbsf

The upper and lower limits of Unit II were observed only in Hole 930B, which is used to define the unit thickness (Fig. 4). Unit II consists predominantly of terrigenous silty clay of dark olive gray (5Y 3/2) to very dark gray (5Y 3/1) color. Faint to moderately distinct color banding (Fig. 7A), mottles (on a centimeter scale; Fig. 7B), and soft micronodules (blebs) (approximately 1 mm scale) are common throughout much of Unit II. These black (5Y 2.5/1) bands and mottles are stains imparted by diagenetic hydrotroilite (see "Introduction" chapter, this volume). In general, darker banding and mottles do not appear to be associated with particular detrital grain sizes, although in some cases silt laminae are heavily stained. The carbonate content of Unit II is less than 3%. Unit II is subdivided into subunits based on the frequency of occurrence of common silt laminae, thin silt beds, and sandy silt or silty sand beds (Figs. 4 and 5).

Subunit IIA

Subunit IIA extends from the base of Unit I to a depth of 9.64 mbsf (Section 930B-2H-3, 94 cm). It consists of a dark olive gray (5Y 3/2) silty clay with common black color banding on a scale from about 1 mm to several centimeters and slight bioturbation and color mottling (Fig. 5). Carbonate content is less than 3%.

Subunit IIB

Subunit IIB extends from 9.64 to 43.00 mbsf (from Section 930B-2H-3, 94 cm, through -5H-6, 130 cm) and is characterized by silty clays with thin laminae of silt and beds of silty sand generally thinner than 2 cm (Fig. 5). The 3.5-kHz sounding profiles (Fig. 3) across the sediment waves on the levee at this site show the bedding pattern as-

sociated with this subunit. The transition from Subunit IIA to IIB is gradational and is placed at the highest recognizable silt lamina. The silty clay that dominates this subunit is dark olive gray to dark gray in color (5Y 3/1 to 5Y 3/2) and appears to be nearly identical to that in Subunit IIA, except that the black color banding, mottles, and blebs are less distinct.

Silt and sand layers compose less than 20% of Subunit IIB, with most occurring as laminae and as a few beds thicker than 1 cm (Fig. 8). In general, the bases of the coarser layers are sharp, but the silt laminae are commonly disrupted, probably as a result of bioturbation. The bed tops are more gradational, with millimeter-thick clay and silt laminae.

Both Holes 930B and 930C show evidence for sediment deformation at about the same stratigraphic level. In Hole 930B, soft sediment deformation is observed just above 27 mbsf (interval 930B-4H-2, 52–81 cm; Fig. 9) and just below 29 mbsf (interval 930B-4H-4, 20–55 cm). At the shallower level, there is an increase in bulk density and decreases in water content and porosity at about this interval. In Hole 930D, folded and disturbed sediment is observed near 32 mbsf (interval 930D-4H-7, 20–30 cm), and the GRAPE data indicate an increase in bulk density at this level (see "Physical Properties" section, this chapter).

Subunit IIC

Subunit IIC extends from 43.00 to 66.65 mbsf (from Section 930B-5H-6, 130 cm, through -8H-3, 95 cm) and consists of dark olive gray to very dark gray (5Y 3/1 to 5Y 3/2) silty clay. The transitional contact from Subunit IIB to IIC is placed below the deepest silt laminae in Subunit IIB. This subunit is nearly identical in structure and appearance to Subunit IIA with the exception that the mottles and color banding are less distinct and generally less common.

Subunit IID

Subunit IID extends from 66.65 to 188.42 mbsf (from Section 930B-8H-3, 95 cm, through -21X-2, 12 cm). This subunit consists of dark olive gray (5Y 3/2) silty clay similar to that in Subunits IIB and IIC, except for the occurrence of silt laminations and interbedded silt and sand layers (Fig. 10). Sand beds are relatively rare, generally less than 2 cm thick, and grade upward to silt (Fig. 11). Similar to Subunit IIB, the coarser intervals in Subunit IID comprise less than 20% of the section overall; however, locally within short intervals of as much as a meter, they can comprise nearly 50% of the sediment (Fig. 12). Silt laminations are most common in the intervals from about 84 to 95 mbsf, 113 to 130 mbsf, and from 155 mbsf to the base of Unit II. With rare exceptions, the fine sand beds occur in the lowest part of this subunit below 182 mbsf. The composition of the coarse grains is indistinguishable from samples examined for Subunit IIB.

X-radiographs from color-banded silty clay in Subunit IID show sharp-based couplets of sediment about 1–2 cm thick, with fine-scale internal laminations (Fig. 13A and B). A thin section from the same interval as one of the X-radiographs (Sample 930B-19X-6, 88–95 cm) contains some of these fine-scale laminae, about 0.1 mm thick, defined by slight differences in 5- to 15-mm-diameter silt (Fig. 13C). Variably oriented quartz silt and mica particles define a poorly organized fabric (Fig. 13D). This fabric suggests rapid deposition of the silt and clay fractions, perhaps as flocs that settled from high-concentration suspensions. Patches of diagenetic hydrotroilite locally overprint the lamination.

Subunit IID has disrupted and deformed bedding between 91.85 and 95.90 mbsf (interval 930C-7H-4, 135 cm, through -7H-7, 90 cm). Coincident with the interval of observed deformation, there is a 30° shift in magnetic inclination and an increase in bulk density recorded in the gamma-ray attenuation porosity evaluator (GRAPE) log (see "Paleomagnetism" and "Physical Properties" sections, this chapter). Another recognized zone of deformation in Subunit IID is in Hole 930B from 125.80 to 128.80 mbsf (interval 930B-14X-5 through -6); this interval appears to correspond to a decrease in the water content (see "Physical Properties" section, this chapter). The observations for both these intervals are consistent with local slumping but do not rule out drilling disturbance as a primary cause of the deformation.

Unit III

Intervals: 155-930B-21X-2, 12 cm, through -24X-CC; 155-930C-13X through -17X-CC
Age: late Pleistocene
Depth: 188.42–242.90 mbsf

The base of Unit III was not recovered in either Hole 930B or Hole 930C; the top of the unit is sharp in Hole 930B but was not recovered in Hole 930C because the hole was drilled without coring from the middle of Unit IID to a depth of 201.10 mbsf (155-930C-13X-1, 0 cm), which is well within Unit III. The upper part of Unit III from 188.42 to 202.00 mbsf is a very dark gray (5Y 3/1) sandy mud with subrounded quartz grains up to fine pebble size (5–10 mm diameter; Fig. 14) and plant debris. This apparently massive sandy mud interval rests on a dark gray to black (7.5Y 2.5/0 to 5Y 2.5/0) laminated clay with faint mottling. The laminated clay interval extends to 206.76 mbsf (930B-22X-CC, 74 cm), and the lowermost meter shows thin zones with convoluted lamination. The laminated clay interval lies above a 1-m-thick layer (interval 930B-23X-1, 0–103 cm) of fine sand containing well-rounded mud clasts ranging in size from 1 to 10 cm (Fig. 15). Core 930B-23X did not have full recovery, so the upper limit of the mud-clast bed is unknown.

The mud-clast interval, in turn, rests on very dark gray and dark olive gray (5Y3/1 to 5Y 3/2) massive clay that extends from 207.13 mbsf to the bottom of Hole 930B at 221.50 mbsf (Fig. 5). The clay recovered in Cores 930C-14X through -17X appears to be the same lithology found at the bottom of Hole 930B, which places its lower limit at 241.09 mbsf (930C-17X-1, 139 cm). This clay appears to be a displaced mass from the continental slope, because the clay contains bathyal benthic foraminifers (forms generally restricted to water depths less than 2000 m) (see "Biostratigraphy" section, this chapter).

The lowermost 1.70 m of recovered sediment is a muddy sand similar to, although coarser than, the upper part of Unit III (930C-17X-2 and -CC, 241.20 to 242.90 mbsf). The contact between this muddy sand layer and the overlying clay body apparently falls within the interval of a whole-round sample taken for interstitial water analysis (Sample 930C-17X-1, 139–150 cm). Unit III is thought to consist of mass-transport deposits, either a single sandy debris flow containing one or more displaced sediment slabs tens of meters thick, or a stack of sandy debris-flow deposits and interleaved slide blocks.

Mineralogy

Mineralogy was determined by estimation of mineral volume percentages in smear slides and by X-ray diffraction (XRD) analysis of fine-grained sediment samples, mostly silty clays.

Smear-slide Synthesis

Based on smear-slide examination, the coarser size fraction from Subunits IIB and IID is a well-sorted sandy silt and fine sand. Grains of quartz are angular to subangular. In general, the coarser layers consist of 50% to 60% quartz, 20% to 40% feldspar, generally plagioclase, and 5% to 10% accessory minerals. This size fraction commonly includes sponge spicules and plant debris, but not rock fragments. The accessory minerals commonly include zircon, hornblende, spinel, garnet, pyroxene, and opaque minerals (probably hydrotroilite and other iron sulfides reflecting reducing diagenetic conditions). The composition of the silt/sand fraction at Site 930 does not change between the subunits or between holes. This fraction consists of arkose from presumed continental and dissected volcanic-arc

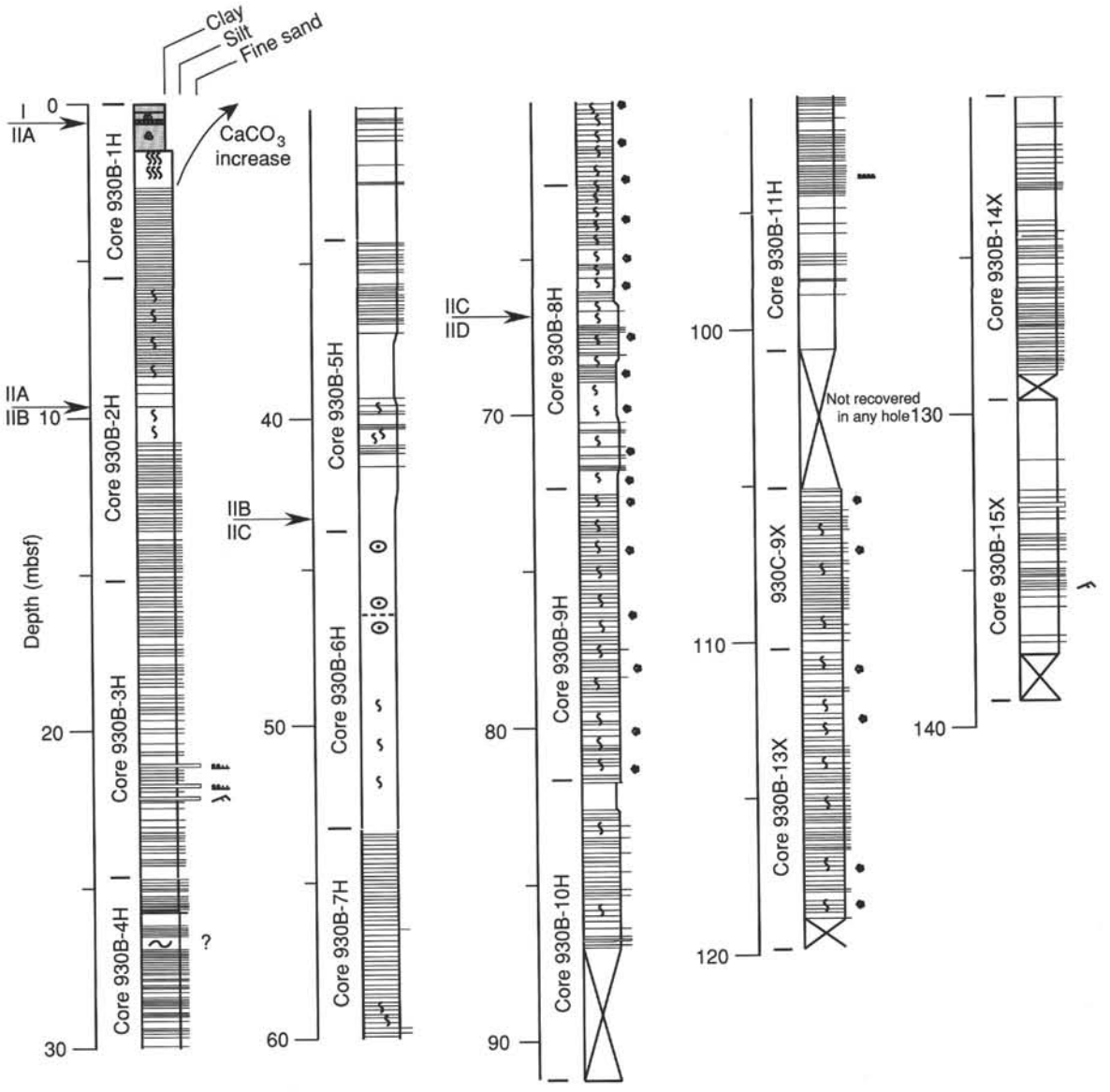

Figure 5. Graphic sedimentological columns for Site 930 showing grain-size variation (width of columns), bed thickness, and sedimentary structures; symbols and preparation of these columns are explained in the "Lithostratigraphy" section of the "Explanatory Notes" chapter, this volume. Arrows indicate the position of unit and subunit boundaries. To fit cores that suffered gas expansion into their cored intervals, the bed-by-bed columns for each core were uniformly compressed using graphics software by the amount needed to decrease their apparent length to the cored length. No compression was applied to cores for which the ODP official recovery was less than 100%, although these cores also generally showed evidence of gas expansion.

sources. The accessory mineral components, including hornblende, hypersthene, monazite, and euhedral zircon, suggest an Andean source area for much of the sediment.

XRD Data

One bulk XRD analysis was performed on a sample of the dominant lithology from most cores in Hole 930B (Table 2). The <2 µm-fraction of four of these samples was further analyzed for clay minerals; oriented mounts of these samples were run air-dried, glycolated, and after heating to 550° C for 1 hr. The heat treatment collapsed the 0.716-nm peak in all diffractograms, indicating the presence of kaolinite and absence of chlorite. Based on these four samples, other samples with a peak in the same position are reported to contain kaolinite but not chlorite. With glycolation, smectite peaks shifted as expected. Mineral abundances are expressed as relative peak intensities of the primary peaks (see "Lithostratigraphy" section, "Explanatory Notes" chapter, this volume). The most abundant mineral throughout the cored succession is quartz. Feldspars, smectite, illite (+mica), and kaolinite are common in all samples. Mafic minerals are present in small quantities. The mineralogical composition is relatively constant throughout Hole 930B.

Spectrophotometry

The reflectance data obtained using the Minolta spectrophotometer reveal only minor changes in the levels of visible light reflectance throughout the sediment column recovered at Site 930 (Fig. 4). Light-reflectance levels are low (between 20% and 25% on average) as a result of the dark color (chroma) of the sediment. The changes ob-

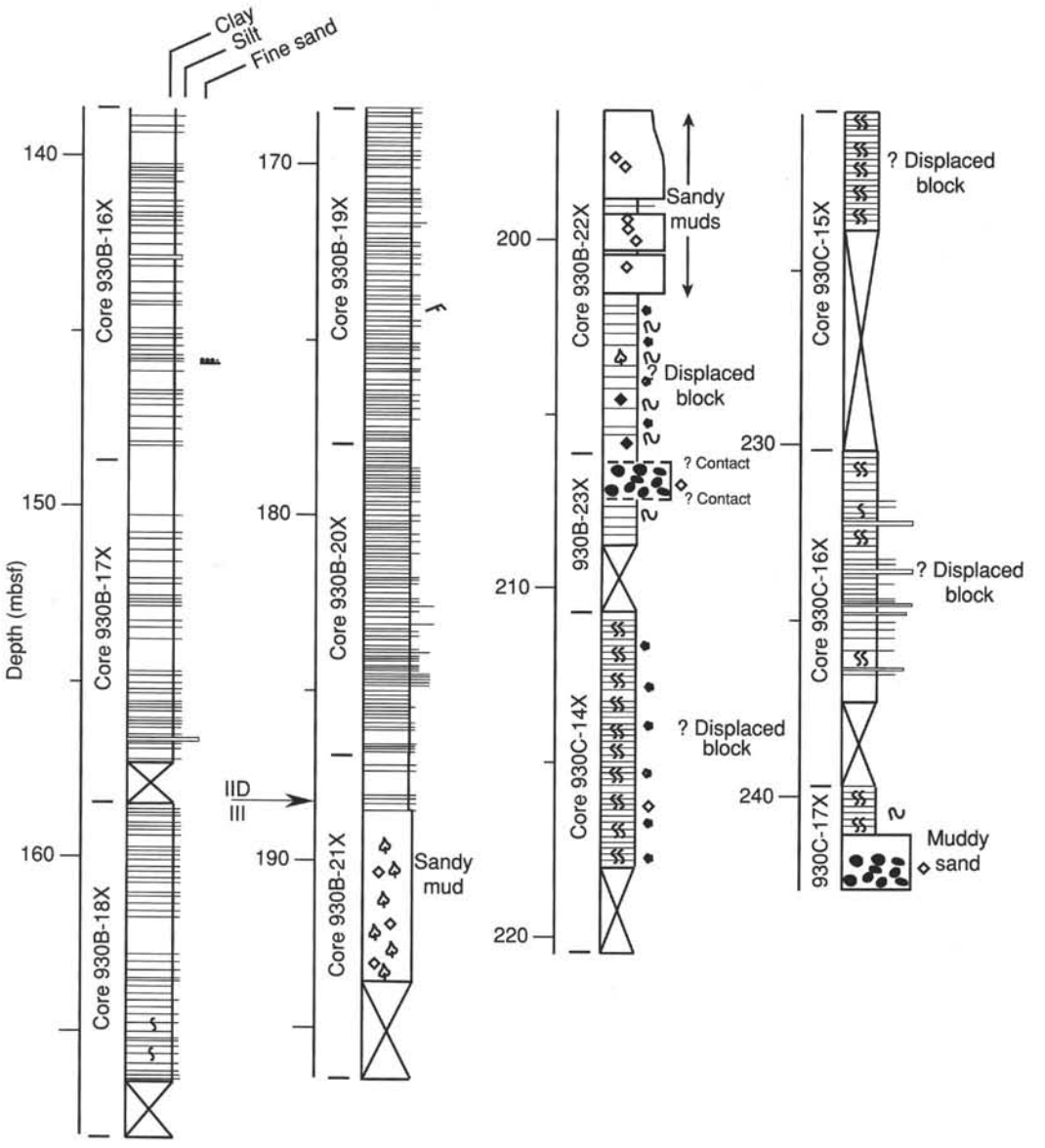

Figure 5 (continued).

served, both in the 550-nm reflectance level (average for the wavelength interval measured) and in the ratio between the blue (700 nm) and yellow (400 nm) end-member reflectance, are dominated by the common high variability between adjacent measurements taken at approximately 40-cm intervals (see Schneider et al., this volume). The fine-scale details in the reflectance fluctuations at Site 930 are not considered to be significant. The high-frequency variability can be attributed to the occurrence of small-scale (centimeter-scale) color changes in the chroma resulting from changes in the amount of iron-sulfide and organic carbon present within the sediment. The greatest variability of the 550-nm reflectance level at Site 930 is in the sediment intervals that contain the largest number of silt/sand beds (Cores 930B-2H to -5H and 930B-13X to -17X; Fig. 4).

Sediment Waves

Holes 930B and 930D penetrated the flanks of adjacent sediment waves 200 m apart on the levee slope (Fig. 3). Hole 930B is on a sediment-wave flank that slopes away from the levee crest, whereas, Hole 930D is near the crest of the adjacent downslope waveform at the top of a sediment-wave flank that slopes toward the levee crest. The basal parts of turbidity currents that overflow the levee crest would thus be flowing downslope past Hole 930B and then uphill past 930D. Unit IIB with its drape of Unit I corresponds to the primary sediment-wave interval defined in Figure 3. Comparison of the sediment recovered from the two holes shows that Hole 930D recovered a thicker interval of Unit IIB and contains more and thicker silt and sandy silt beds than at Hole 930B. In addition, there is nearly an order of magnitude difference in the number of beds that include sand-size material (Table 3). The accumulation of sediment during comparable intervals within Unit IIB shows a consistent trend between the two sections with thicker beds and more coarse material at Hole 930D. The greater depth (mbsf) to the top of Unit IIB shown in Table 3 indicates that Unit IIA also accumulated at a higher rate at Hole 930D.

Discussion

The general lithology at Site 930 is a thin carbonate-rich clay of Holocene age (Unit I) overlying a thick section of turbidite deposits

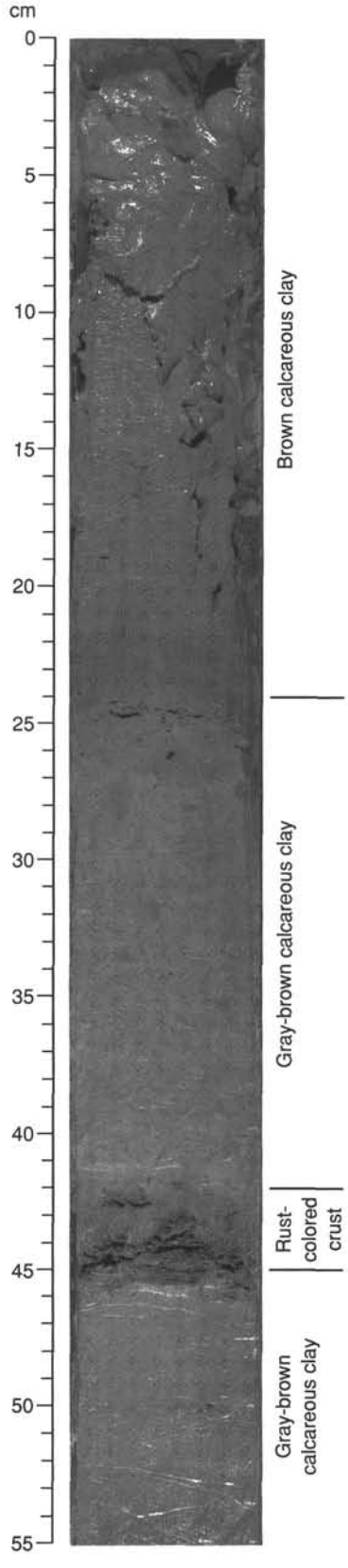

Figure 6. Unit I showing calcareous clay over the diagenetic iron-rich crust at 42–45 cm (interval 155-930B-1H-1, 0–55 cm).

of terrigenous sediment (Unit II) of late Pleistocene age. The turbidite deposits rest on mass flow deposits (Unit III) thought to be primarily of debris-flow origin (Fig. 5). The subunits within Unit II reflect changes in the amount of coarser grained sediment being delivered to the area by turbidity currents. Subunits IIB and IID are dominantly turbidity-current deposits, and Subunits IIA and IIC are more hemipelagic. Based on preliminary biostratigraphic information, the following approximate accumulation rates have been determined: 0.10 to 0.15 m/k.y. for Unit I and ~5 m/k.y. for Unit II (above 135 mbsf). It is probable that the hemipelagic intervals (Subunits IIA and IIC) have a lower accumulation rate than the more turbidite-rich intervals (Subunits IIB and IID).

BIOSTRATIGRAPHY

Calcareous Nannofossils

The Holocene calcareous clay of Site 930 contains moderately to well-preserved, diverse assemblages of calcareous nannofossils. In contrast, the Pleistocene mud and silt sections are characterized by sporadic occurrences of poorly preserved nannofossils.

The nannofossils at the mud line of Holes 930A, 930B, and 930D have a highly diversified and well-preserved assemblage representing the youngest nannofossil Zone CN15b. A similar but less well-preserved assemblage appears in Unit I in Sample 930B-1H-1, 130–131 cm (1.31 mbsf). The abundance and preservation of calcareous nannofossils decrease quickly downhole. Units II and III of Holes 930B and 930D (Samples 930B-1H-CC, 28–29 cm, and 930D-1H-CC, 28–29 cm) are characterized by the absence or a low abundance of solution-resistant nannofossil species (*Ceratolithus* sp., *Sphenolithus* sp., and *Reticulofenestra* sp.). These units lack age-diagnostic species (Fig. 16; Table 4). One exception, however, is the assemblage recovered from sediment interpreted as a debris flow at the bottom of Hole 930B in Unit III (Sample 930B-24X-CC, 36–37 cm). This assemblage includes poorly preserved species of middle Pleistocene age (Subzone CN14b) that may have been reworked from older sediment.

Reworked Tertiary nannofossils (*Discoaster* sp.) are observed in the mud-line (water collected from the top of the first core) sample of Hole 930D and in Sample 930B-1H-2, 23–24 cm.

Planktonic Foraminifers

High abundance and a diverse assemblage of planktonic foraminifers are characteristic of Unit I, whereas low abundance and a lack of diversity are characteristic of Unit II. Planktonic and benthic foraminifer abundance increases in Unit III at 193–221 mbsf (930B-21X-CC, 10 cm, to -24X-CC, 27 cm). Debris-flow deposits were identified at 129–157 mbsf (930B-14X to -17X) and 193–221 mbsf (930B-21X to -24X) (see "Lithostratigraphy" section, this chapter). These intervals are characterized by:

1. A high abundance of bathyal benthic foraminifers that are associated with organic-rich sediment. These usually occur in shelf sediment, although they can be found down to a water depth of 2000 m (van Morkhoven et al., 1986).
2. Large broken sponge spicules (siliceous and carbonate) (100–700 µm).
3. Wood fragments (100 µm to 1 cm).
4. Iron-stained and/or heavily calcified benthic and planktonic foraminifers.
5. A diverse planktonic foraminiferal assemblage.

The disappearance of *G. menardii* and *G. tumida,* which defines the base of the Z Zone (Table 5) is located at 15.02 mbsf (930B-2H-CC). However, given the likely downhole contamination of core-

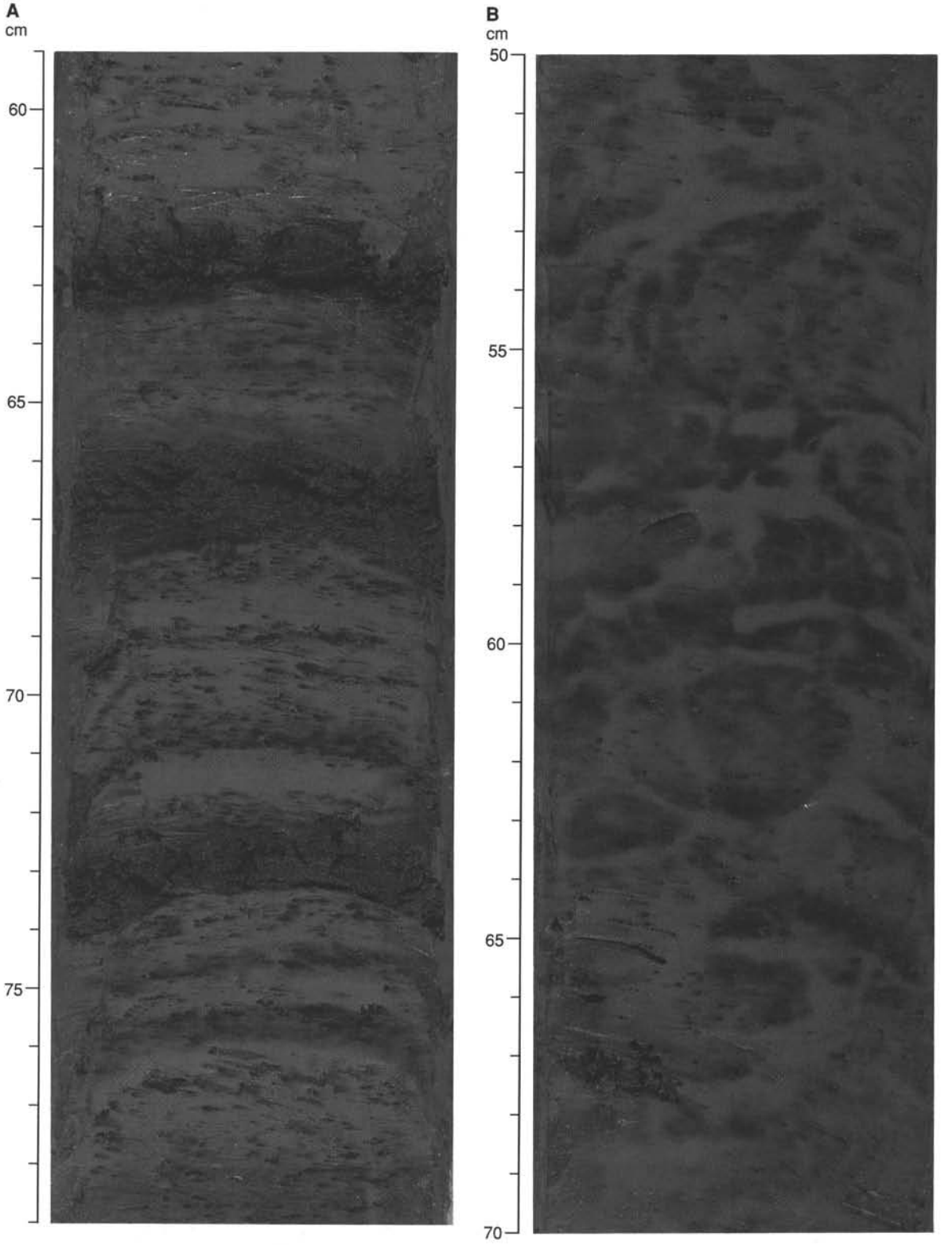

Figure 7. **A.** Color banding in upper part of Unit IIA (interval 155-930D-1H-3, 59–79 cm). **B.** Mottling in upper part of Unit IIA (interval 155-930D-1H-2, 50–70 cm).

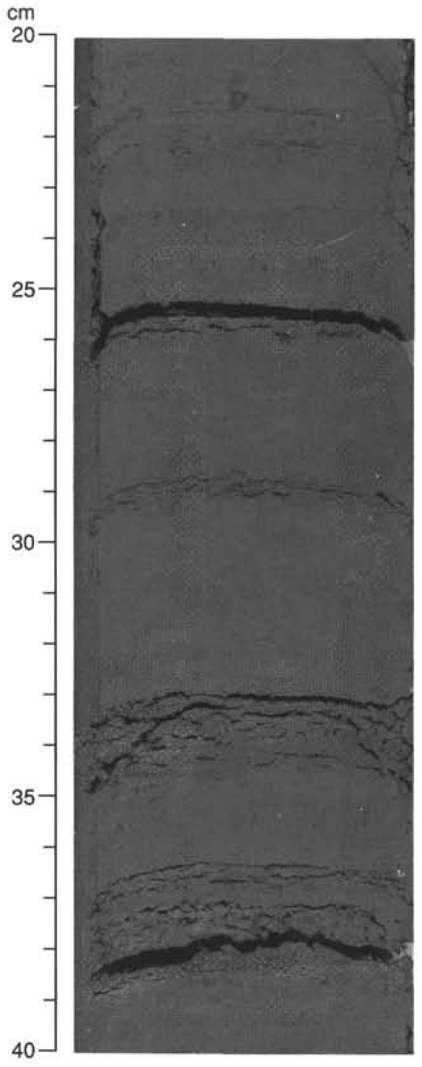

Figure 8. Silt laminae and beds from Unit IIB (interval 155-930B-4H-1, 20–40 cm). The gas expansion gaps at the base or within the silt layers are typical of those observed throughout Subunits IIB and IID (e.g., Figure 11).

catcher samples, the Z/Y zonal boundary is probably located near the base of Unit I at a much shallower depth. The $Y_{P.\ obliq.}$ datum (40 ka) was given a preliminary assignment to Sample 930B-15X-CC, 7–16 cm (137 mbsf). This assignment was based on the presence of only one well-preserved specimen of *P. obliquiloculata*. No other specimens of *P. obliquiloculata* were found in the late-Pleistocene-age sections that were not reworked.

Siliceous Microfossils

Site 930 is almost barren of diatoms except for the uppermost part of Holes 930A and 930B (Table 4). Pelagic diatoms of marine origin are rare but well preserved in the mud-line samples of Holes 930A and 930B. The assemblages include the age-diagnostic species *Pseudoeunotia doliolus* of late Pleistocene age. Diatoms decrease rapidly downhole in Holes 930B and 930D (Table 4). In Sample 930B-1H-1, 6–7 cm (0.06 mbsf), the diatom assemblage is fragmented and poorly preserved. No diatoms are present below a depth of 1.31 m in the Holocene section of Hole 930B (Sample 930B-1H-1, 130–131 cm. No diatoms were found in any of the pre-Holocene sections of Site 930.

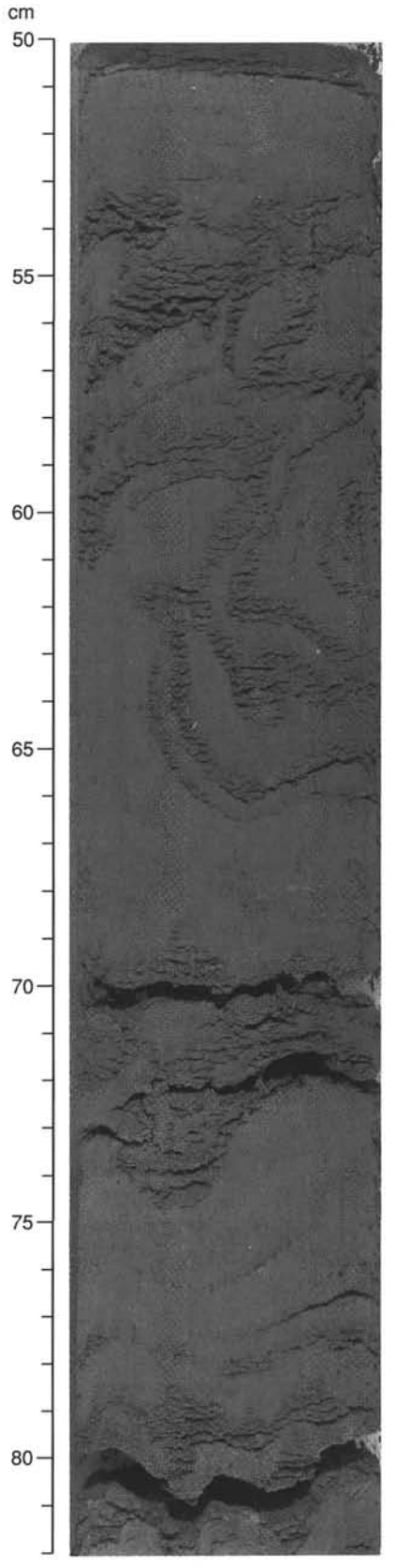

Figure 9. Soft-sediment folds in Unit IIB (interval 155-930B-4H-2, 50–82 cm).

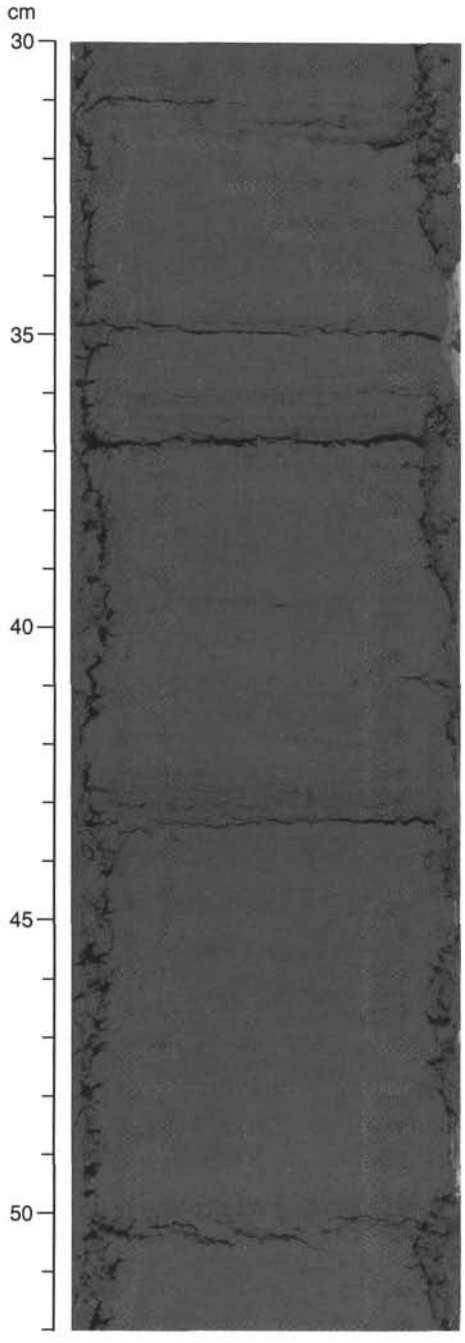

Figure 10. Silt laminations and thin-bedded muds in Unit IID (interval 155-930B-19X-6, 30–52 cm.)

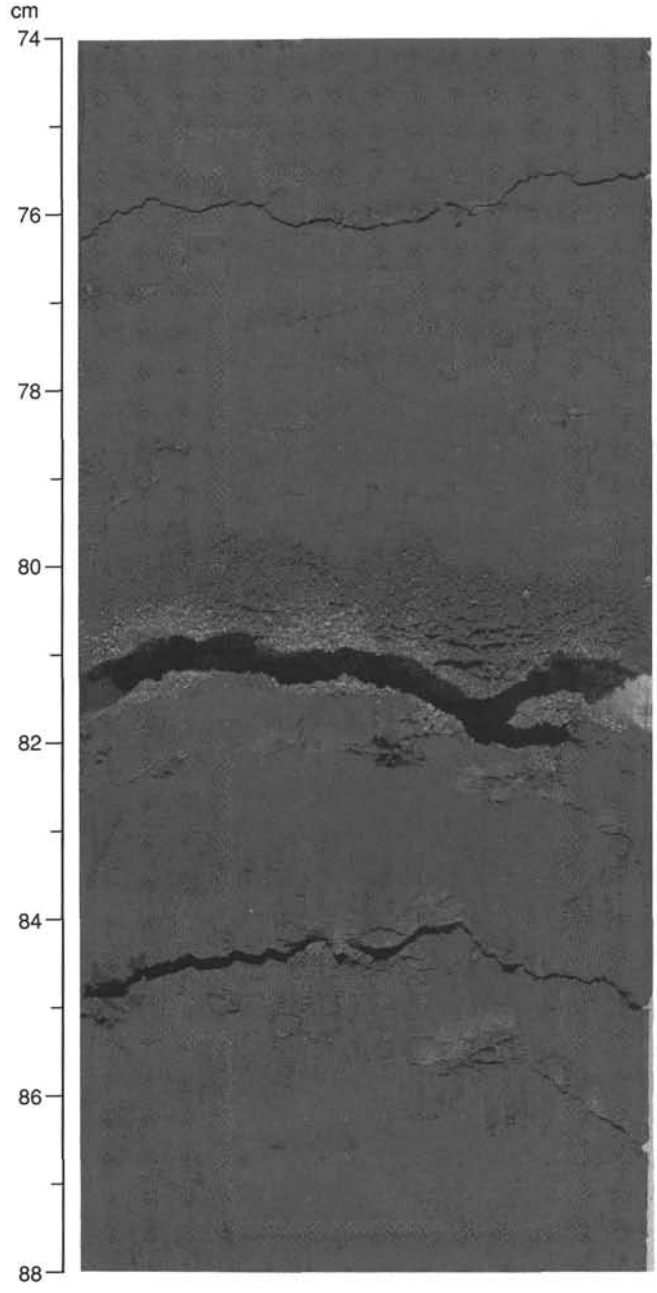

Figure 11. Typical thin sand and silt laminae from the upper part of Subunit IID (interval 155-930B-11H-3, 74–88 cm).

Freshwater diatoms from the drainage basin of the Amazon River were not observed in any of the core-catcher samples at Site 930.

Siliceous sponge spicules are the most commonly occurring form of biogenic silica at Site 930, occurring in a variety of forms. The spicules appear to be present in highest abundances in discrete patches within individual turbidite sequences (e.g., at 86.9 mbsf; Sample 930B-10H-4, 69 cm).

Radiolarians are present as fragments in the mud-line samples of Holes 930A and 930B and in the top of Hole 930B (Sample 930B-1H-1, 67 cm). Radiolarians have not been found in any of the core-catcher samples.

Authigenic Mineral Nodules

Abundant authigenic mineral nodules were observed in the sand-size fraction. These include black nodules, which are iron sulfides, and blue nodules, which are vivianite ($[Fe, Mg]_3[PO_4]_2 \cdot 8H_2O$). The vivianite nodules have an inverse abundance pattern with planktonic foraminifers (Fig. 17). Nodules were not found in the sections with abundant sand. Although common in anoxic lake sediment, vivianite is uncommon in marine sediment unless enough sedimentary Fe is present to titrate all the sulfide. Then, as pore-water Fe levels build up, the saturation level of vivianite is reached and the nodules precipitate. Pore-water phosphate concentrations increase to 7 mbsf and then rapidly decrease in Hole 930C (see "Inorganic Geochemistry" section, this chapter), which indicates that this precipitation occurs at

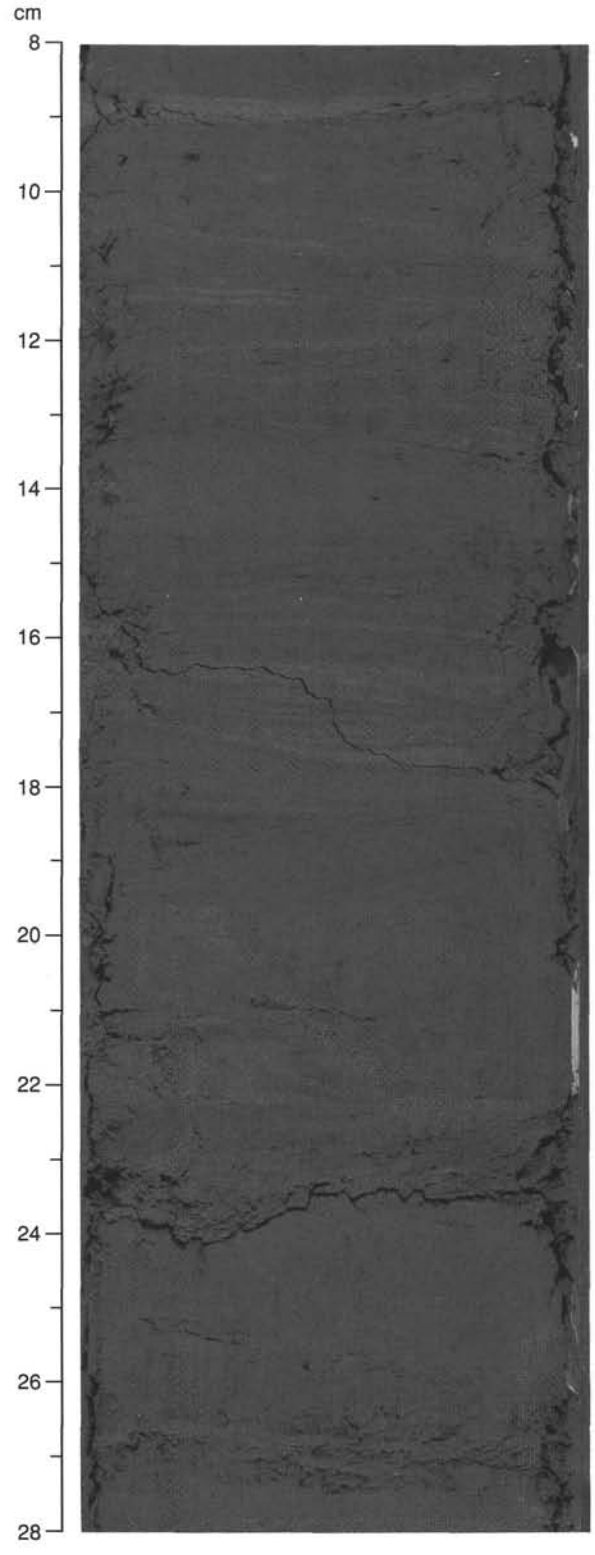

Figure 12. Thin-bedded silt and silty sand laminae and beds from Subunit IID (interval 155-930C-11X-3, 8–28 cm).

a fairly shallow level in the sediment column. The inverse abundance relationship of the vivianite nodules to the abundance of planktonic foraminifers is most likely a result of changes in sedimentation rates.

Palynology

Eight core-catcher samples were examined for palynomorphs from Hole 930B (Table 6). The Holocene pollen and spore assemblages from samples at 0 mbsf (Sample 930B-1H mud line) and 5.7 mbsf (Sample 930B-CC, 28–29 cm) have higher abundances than expected, which may represent contamination from the coring procedure. Six late-Pleistocene-age samples from 53.8 mbsf to 221.5 mbsf (Table 6) have variable pollen abundance and preservation. The pollen assemblages include Euphorbiaceae, Gramineae, tricolporate (TCP) type, Cyperaceae, and Cyatheaceae, Lycopodidae, and monolete spores. Low pollen and spore abundance in upper Pleistocene sediment may reflect periods of rapid sedimentation or sorting of pollen and spore grains. Poor to moderate preservation suggests that reworked pollen and spores from older, previously deposited sediment may be a significant element of the total palynomorph assemblage. Sand-sized wood fragments were recorded in all samples. Dinoflagellates were not well preserved and are rare or absent in the samples examined.

Stratigraphic Summary

The biostratigraphy at Site 930 was based on the planktonic foraminifer assemblage, because of the low abundance of calcareous nannofossils, diatoms, pollen, and spores. The disappearance of *G. menardii* and *G. tumida* from the foraminifer assemblage initially places the Ericson Z/Y zonal boundary at 15 mbsf. However, the actual boundary is most likely associated with the base of Unit I at a much shallower depth due to a downhole contamination of core-catcher samples. In Unit I all the microfossil groups were high in abundance. This unit was classified as the Holocene or Zone Z. In Unit II, all microfossil groups have low abundances because of the high sedimentation rates. Unit II was classified as the Y Zone on the basis of the absence of *G. menardii*. In Hole 930B, the $Y_{P.\ obliq.}$ datum (40 ka) is located at 137.5 mbsf (Sample 930B-15X-CC, 7–16 cm). This assignment was based on only one specimen and should therefore be viewed with caution.

PALEOMAGNETISM

Remanence Studies

Archive halves from all 26 APC cores from this site were measured on the pass-through cryogenic magnetometer. As expected for Neogene sediment from a low-latitude site, most cores exhibited low inclinations distributed about 0° after alternating field (AF) demagnetization. As is common for ODP cores, a strong downward component of magnetization, derived from the drill string, was present on all measured sections. However, this remanence overprint was, in general, greatly diminished or erased entirely by 10- to 25-mT AF demagnetization. No evidence of the persistent, radially directed overprint that plagued the previous leg (Curry, Shackleton, Richter, et al., in press) was observed in the APC cores.

In general, XCB cores were not measured, as breaks in the core allowed for rotation of short pieces about a vertical axis, creating biscuits. Measurements on three XCB cores (Sections 930B-14X-1, 930B-21X-3, and 930C-11X-5) revealed fluctuations in declination that corresponded to discontinuities between biscuits caused by drilling. The combination of XCB drilling biscuits and the low equatorial magnetic inclinations at this site made the XCB cores unsuitable for

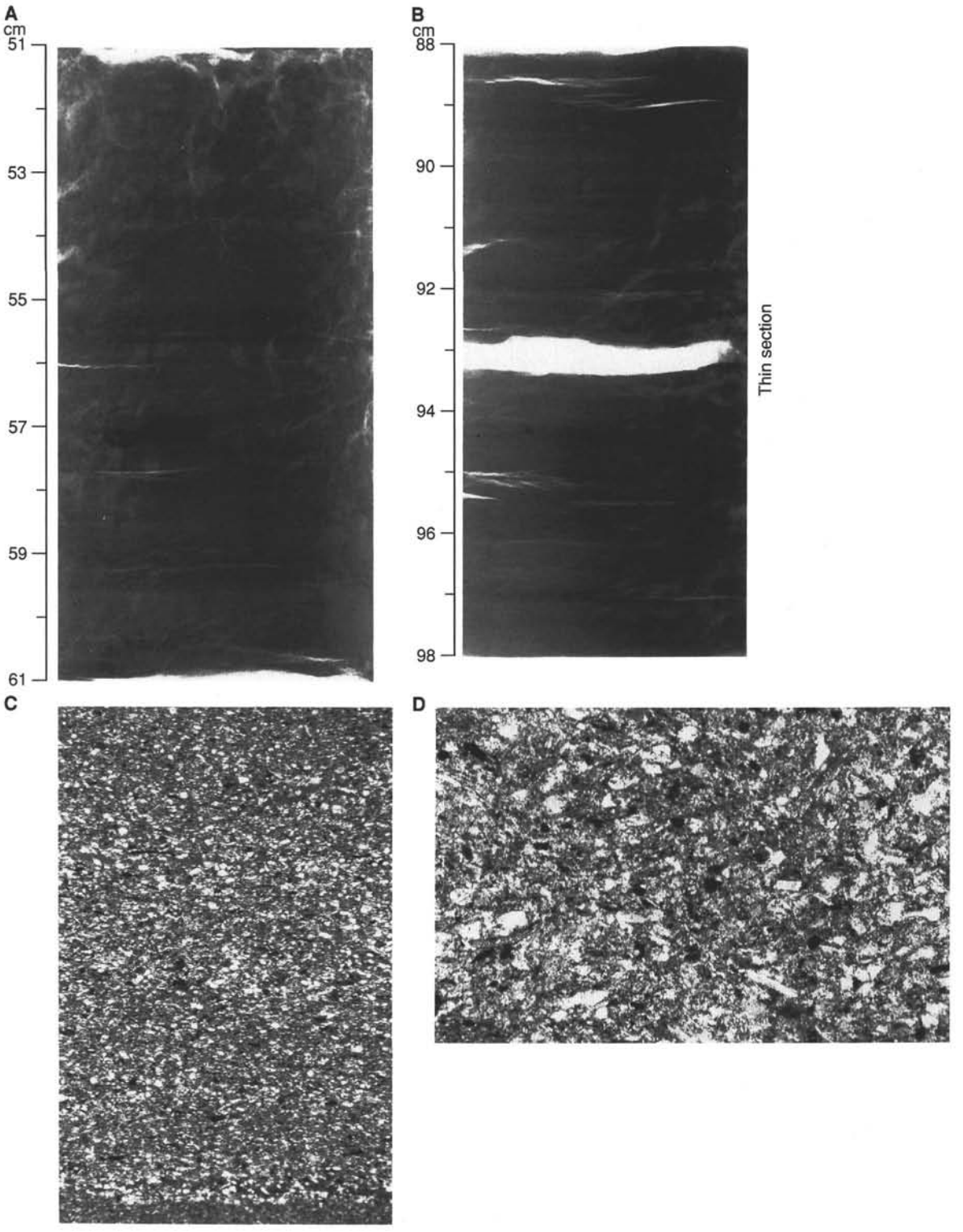

Figure 13. Characteristics of color-banded silty clay in Subunit IID. **A.–B.** Contact prints of X-radiographs showing sharp-based couplets that consist of basal, more silt-rich sediment (dark tone) and upper more clay-rich sediment (light tone). (A) = interval 155-930B-19X-6, 51–61 cm; (B) = interval 155-930B-19X-6, 88–98 cm). **C.–D.** Photomicrographs in plane-polarized light of a thin section cut from the interval shown in (B) of this figure (Sample 155-930B-19X-6, 88–95 cm): (C) Sharp-based content-graded lamina of silty clay; (D) The fabric of silty-clay laminae in color-banded sediment. The bottom of (D) is parallel to bedding; note the steep dip of the apparent long axes of some silt grains. Scale for (C) and (D): 1 mm = 43 mm on photo.

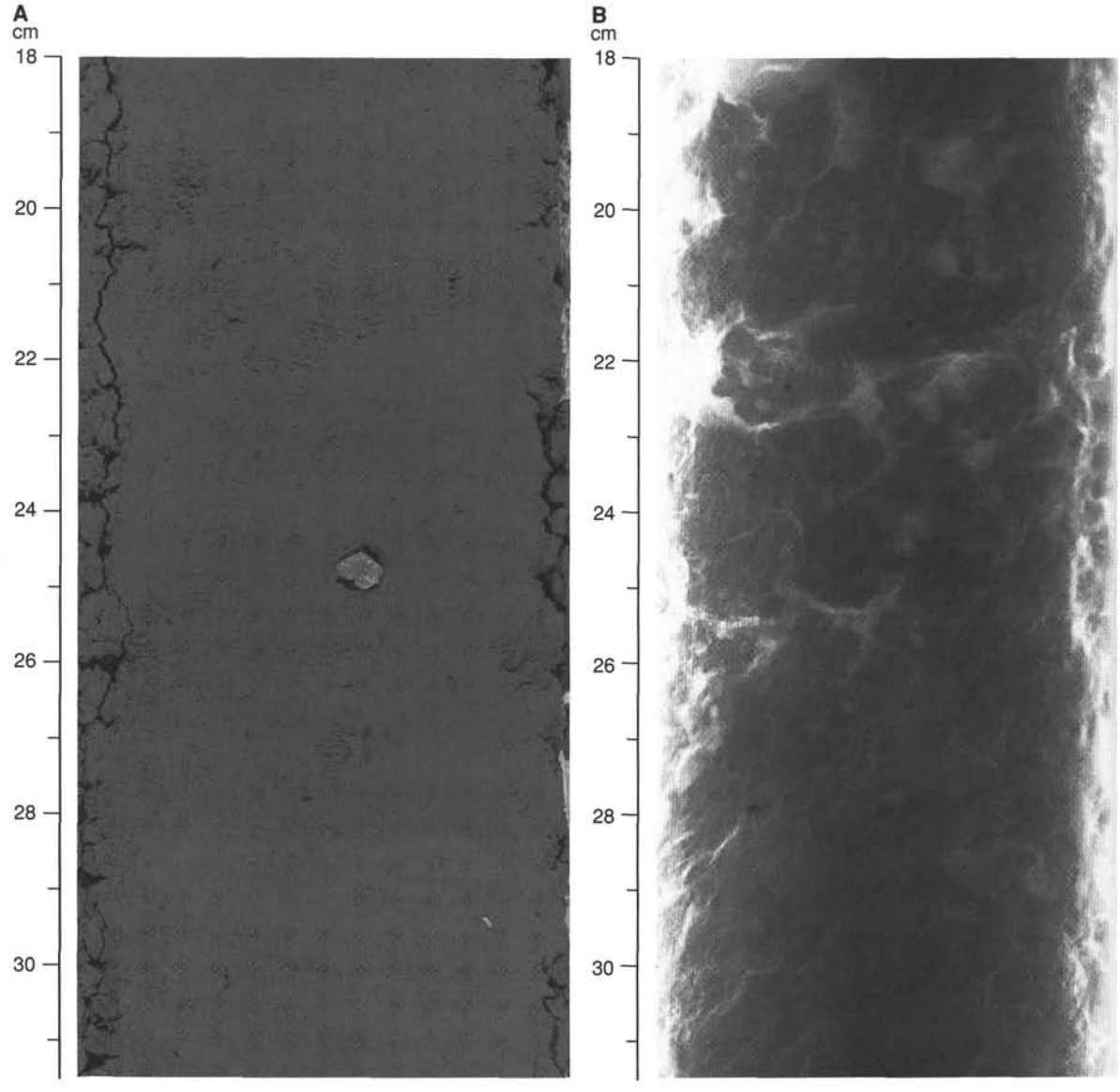

Figure 14. **A.** Subrounded quartz pebble in massive clayey silt from the upper part of Unit III (interval 155-930B-21X-4, 18–31 cm). **B.** X-radiograph of the same interval showing additional clasts within this clayey silt deposit.

detecting polarity excursions and events that could serve as chronological datums.

Azimuthal orientation with the Tensor tool was attempted for nine of the APC-drilled cores for Hole 930B. In four of the cores, the Tensor data gave inconsistent readings or unrealistic field inclinations. In five cores, the tool appeared to be functioning well, but the calculated declinations were either 90°, 180°, or 270° out of phase with the expected near 0° declinations. The cause of this phase shift is unknown; however, another (nonrechargeable) battery pack was loaded into the unit for Site 931.

Correlative changes in remanence intensity and direction are present in these two holes in Cores 930B-10H and 930C-7H, occurring at depths of 85.2 mbsf in Hole 930B and 89.3 mbsf in Hole 930C (point A in Figs. 18 and 19). Records in both holes show a peak in intensity and positive inclination at this point, with an underlying trend toward lower intensities and negative inclinations. At point B another underlying peak in intensity and positive inclination is observed in both cores. Correlation between the declination records is not as good, as the Hole 930C data swing over 180° toward the east (positive declination) immediately below point C. Both records show a sharp positive declination spike (point D) 85 cm below point C. Despite the similar character of these spikes, their absolute correlation is not clear because it occurs slightly below peak B in Hole 930B (Fig. 18) and above peak B in Hole 930C (Fig. 19).

These anomalous remanence variations may represent a polarity excursion corresponding to the Lake Mungo Excursion at ~30 ka (Stupavsky and Gravenor, 1984), because the foraminifer species *P. obliquiloculata* (~40 ka datum) was observed in Core 930B-15H (see "Biostratigraphy" section, this chapter). The bias of the inclinations toward high negative values in Core 930C-7H occurs near an interval of steeply dipping laminations visible in this core (see "Lithostratigraphy" section, this chapter). Several observations suggest that at least part of Core 930C-7H may represent a sediment slump: (1) large bedding dips visible in parts of the core; (2) poor correlation in the declination records, which could result from internal deformation, or twisting of Core 930C-7H between 89.5 and 90.0 cm (core photographs indicate rotation of the dip directions within this same interval); and (3) the 5.3-m difference in depth of this zone between Holes

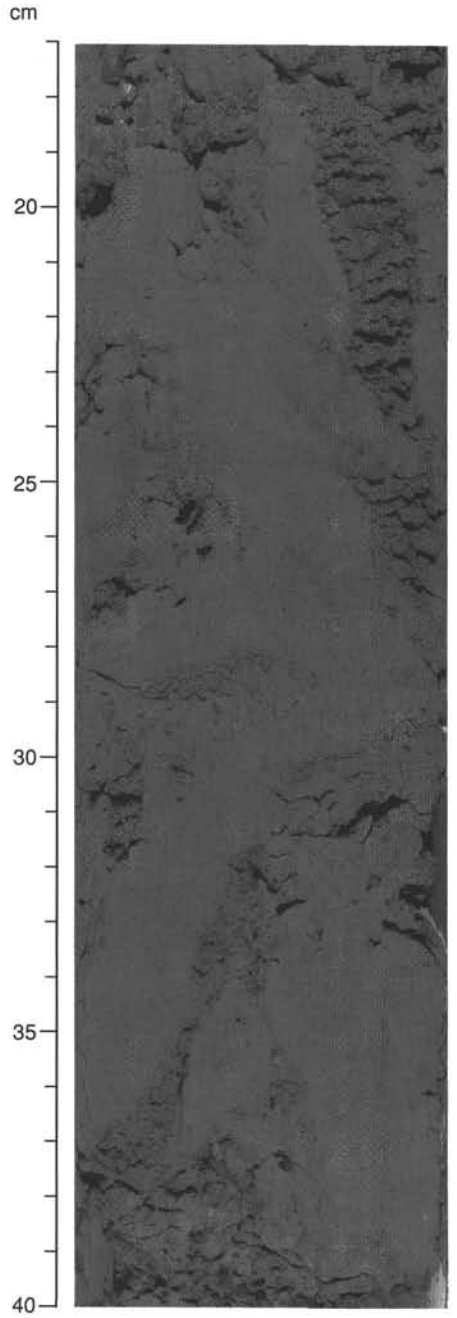

Figure 15. Rounded and deformed mud clasts in fine sand matrix from Unit III (interval 155-930B-23X-1, 17–40 cm).

930B and 930C. Note that the 5.3-m offset cannot entirely be explained by depth inaccuracies resulting from gas voids, whose total dimensions were less than 1 m in both of the interval cores.

The archive-half measurements from Hole 930C also produced a highly detailed record of inclination oscillations about 0° (Fig. 20) probably representing secular variation. At least 15 cycles can be discerned, as numbered in Figure 20 in downhole sequence from 42 to 75 mbsf.

Magnetic Susceptibility

Whole-core magnetic susceptibility was measured using the multisensor track (MST) on all core sections of Site 930 with the exception of Core 930A-1H. Cores 930B-1H and 930D-1H were interpreted to have sampled the mud line (see "Lithostratigraphy" section, this chapter) and thus were measured at 3-cm intervals. The remaining core sections were measured at 5-cm intervals. Discrete-sample magnetic susceptibility was measured on at least one sample per core, with higher sample densities (at least one sample per section) in Cores 930A-1H and 930B-1H. Two meters were added to the reported depths of the Hole 930A discrete samples to correspond to the apparent correlation depth with Hole 930B (see "Lithostratigraphy" section, this chapter). In addition, the measurement of the anisotropy of magnetic susceptibility (AMS) was attempted on three samples that contain silt laminae (Samples 930B-1H-2, 129–131 cm; -8H-7, 60–62 cm; and -8H-7, 63–65 cm). However, because of the instability of the Kappabridge instrument at range values below 7 and the relatively weak susceptibility of the sediment, the results are considered unreliable. Therefore, further measurements of AMS will not be performed aboard ship.

Both the whole-core and discrete-sample susceptibility data showed a general downhole increase in value that probably resulted from dewatering due to compaction. This trend was removed from all data using linear regression analysis of the data from Unit II, with chronology from biostratigraphic datums and the Late Mungo Excursion. The trends were removed from the whole-core and discrete-sample data separately (Fig. 21). Overall, the data are highest within the coarse-grained (sandy) debris flow of Unit III (about 200 mbsf). The basal, finer grained (clayey) debris flow has the lowest values, suggesting a relationship between sedimentologic grain size and magnetic-mineral concentration within Unit III.

The susceptibility signal does not change across subunit boundaries of Unit II. The variations in susceptibility data within Unit II can probably be related to regional environmental changes. For example, the whole-core data show apparent cyclicities within Unit II. Visual estimates between 15 and 90 mbsf suggest a first-order cycle with a period of about 5 ka (3 cycles) and a possible second-order cycle with a period of about 1.5 ka (10 cycles), based on the estimated average accumulation rate of 5 m/ka for Unit II (see "Lithostratigraphy" section, this chapter). The relationships of these cycles to sedimentologic processes require further onshore study.

ORGANIC GEOCHEMISTRY

Volatile Hydrocarbons

Gas analyses were conducted on samples from Hole 930B to a depth of 220 mbsf and three samples from the deeper horizons of Hole 930C. Headspace methane concentrations at Site 930 increased rapidly below the sediment surface and then remained moderately high (Fig. 22; Table 7), ranging from about 9000 ppm at 13 mbsf to 2000 ppm at ~240 mbsf. The sharp increase near the sediment surface reflects the onset of methanogenesis. The vacutainer samples taken from gas expansion voids displayed a C_1 concentration profile similar to the headspace analyses, although they gave higher values (Table 7). The elevated vacutainer concentrations are due to the sampling method, which minimizes dilution of sedimentary gases by air relative to the headspace sampling approach.

Low concentrations of ethane (C_2; 3 ppm) and propane (C_3; 1 ppm) were detected in only one vacutainer gas sample (Sample 930B-6H-6, 0–5 cm). The C_1/C_2 ratio in this sample was approximately 250,000. No volatile hydrocarbons larger than C_1 were measured in headspace samples. The gas compositions observed at Site 930 suggest a mainly biogenic methane source and caused no safety concerns during drilling.

Carbon, Nitrogen, and Sulfur Concentrations

Weight percentages of inorganic carbon (IC), total carbon (TC), total nitrogen (TN), and total sulfur (TS) were measured at various

Table 2. Relative peak intensities of the main minerals in representative lithologies from Site 930.

Core, section, interval (cm)	Relative intensity of primary peaks							
	Smectite	Mica + Illite	Kaolinite	Quartz	Plagioclase	K-feldspar	Augite	Hornblende
155-930B-								
1H-1, 95–96	7.4	12.8	8.6	100	8.2	*	3.6	*
1H-2, 120–122	10	13.6	9.3	100	9.2	4.4	2.8	*
2H-3, 56–57	15.1	29.6	14.2	100	8.9	*	3.5	*
3H-3, 57–58	11.7	27.4	13.7	100	10.3	4.3	2.6	*
4H-3, 58–59	9.2	15.2	8.4	100	3.1	6.8	1.4	*
5H-3, 56–57	12.9	27.6	13.7	100	5.7	10.9	2.8	*
6H-2, 86–91	9.8	14.6	10.7	100	6.4	*	3.5	*
7H-3, 56–57	14.8	27.1	13.9	100	10.3	5.3	3.6	*
8H-3, 55–56	9.4	25.8	11.8	100	9.5	4.3	2.7	*
9H-5, 39–41	7.1	15.3	9.4	100	8.6	*	3	*
10H-3, 58–60	10.4	26.6	12.6	100	8.8	*	3.1	*
11H-3, 57–59	13.9	20.6	14.5	100	21.4	*	3.5	*
12X-2, 75–76	13.7	26.6	13.5	100	16.9	6.5	2.8	1.2
13X-3, 55–56	13.5	31.5	16	100	17.7	5.6	3.1	*
14X-4, 110–111	13.3	20.9	14.6	100	10.8	5.6	3.1	*
15X-3, 60–61	9.3	16.9	11.2	100	10	4.8	2.6	1.5
16X-3, 100–101	8.8	13.5	8.3	100	6.7	4.6	2.1	*
17X-1, 125–126	10.1	19.2	15.9	100	9.8	*	3.3	*
17X-3, 60–61	15.2	28.3	17.1	100	12.6	5.7	3.2	*
18X-3, 34–35	14.7	23.7	14.5	100	11.8	*	3.5	*
19X-3, 57–58	20.6	36.5	20.8	100	11.8	17.3	3.6	*
20X-3, 60–61	13.5	33	15.5	100	10.4	11.1	*	*
21X-3, 50–51	13.6	24.1	13.9	100	8	6.3	2.5	*
22X-1, 61–62	11.9	18.5	9.9	100	22.4	5.1	2	0.9
23X-1, 87–88	15.7	20	12.5	100	16	5.8	3.2	*
24X-3, 54–55	6.2	14.5	20.5	100	9	5.3	3.4	*

Notes: See "Lithostratigraphy" section in the "Explanatory Notes" chapter, this volume, for XRD methods. * denotes non-detection.

Table 3. Comparison of sediment accumulation parameters for Unit IIB, which corresponds to the sediment-wave section, between Holes 930B and 930D.

	Hole 930B	Hole 930D
Total interval	9.8 to 43.7 mbsf	13.5 to 51.5 mbsf
Thickness	32.2 m	36.9 m
Number of silt laminae	312	289
Number of silt/sand beds	17	62
Total number of beds and laminae	329	351
Sum of silt/sand bed thicknesses	36 cm	122 cm
Number of beds with sand	>3	>25

depths in Hole 930B and at selected horizons in Holes 930A and 930C (Table 8). From these measurements the weight percentages of carbonate (calculated as $CaCO_3$) and total organic carbon (TOC) were calculated. The concentration profiles for $CaCO_3$, TOC, TN, and TS are illustrated in Figure 23.

Carbonate concentrations are high in the top 0.4 mbsf (30%) and fairly low throughout the rest of the core (<5%). In contrast, TOC displays low concentrations (<0.4%) in the first meter below the seafloor. Below this depth TOC values increase to about 1% and then steadily decrease downhole to 0.8%. Several discrete intervals (92, 125, 133, 188, and 202 to 216 mbsf) in Hole 930B display markedly lower TOC values (ranging from 0.45% to 0.7%) relative to those in sediment above or below (Fig. 23).

Total nitrogen displays a concentration profile that is generally similar to that of TOC. Low TN values (<0.07%) were observed in the top meter. Higher values (0.08% to 0.11%) were observed between 14 and 200 mbsf, with lower concentrations at the same intervals of low TOC. Unlike TOC, however, TN concentrations are distinctly higher (<0.13%) below 203 mbsf. Total sulfur concentrations range from 0.2% to 0.7% in the first 4 m of Hole 930B. Below this depth TS concentrations decrease to less than 0.2% except for two higher values measured at 203 and 216 mbsf.

The low TOC and high IC concentrations at the top of the section are from sediment in lithologic Unit I, which is mainly composed of nannofossil and foraminifer-rich clays of Holocene age (see "Lithostratigraphy" section, this chapter). The elemental compositions in these horizons reflect reduced input of terrigenous material during the Holocene.

The TS profile in the top 20 m likely reflects the degradation of organic matter by sulfate reduction. This observation is consistent with the pore-water sulfate concentrations (see "Inorganic Geochemistry" section, this chapter). Diagenesis of organic matter over longer time scales might be deduced from the slow but steady decrease in TOC and TN from 3 to 200 mbsf (lithologic Unit II). Several horizons show markedly lower TOC and TN concentrations over this sedimentary interval. There is a direct relationship between these lower values and the occurrence of silt layers, indicating a decreased organic matter content in coarser sediment.

Elevated TN and TS concentrations at depths greater than 200 mbsf are characteristic of the debris flow in Unit III and may be indicative of a different organic matter source and/or depositional environment.

Atomic ratios of organic carbon to total nitrogen, [C/N]a, range from 9 to 16 over most of Site 930. Lower ratios ranging from 6 to 8 are observed at 0.17 and below 200 mbsf. These compositions may suggest a mixture of marine and terrigenous organic matter sources. Lithologic and paleontologic results, however, indicate that the bulk of the material in this sediment is of terrigenous origin. The use of [C/N]a ratios as source indicator is controversial, particularly when sediment contains substantial amounts of inorganic nitrogen, as in the case of Site 930 (see "Inorganic Geochemistry" section, this chapter).

INORGANIC GEOCHEMISTRY

Interstitial Water Analysis

Interstitial water analyses were collected from 13 sediment samples at Site 930 (Table 9; Fig. 24). Samples are primarily from Hole 930B, between 1.45 and 220.10 mbsf, with sample frequency approximately one per 10 m for the upper 50 m and one per 30 m thereafter. One sample was collected from Hole 930A at a reported depth of 7.45 mbsf, and one sample was taken from Hole 930C at 241.10 mbsf.

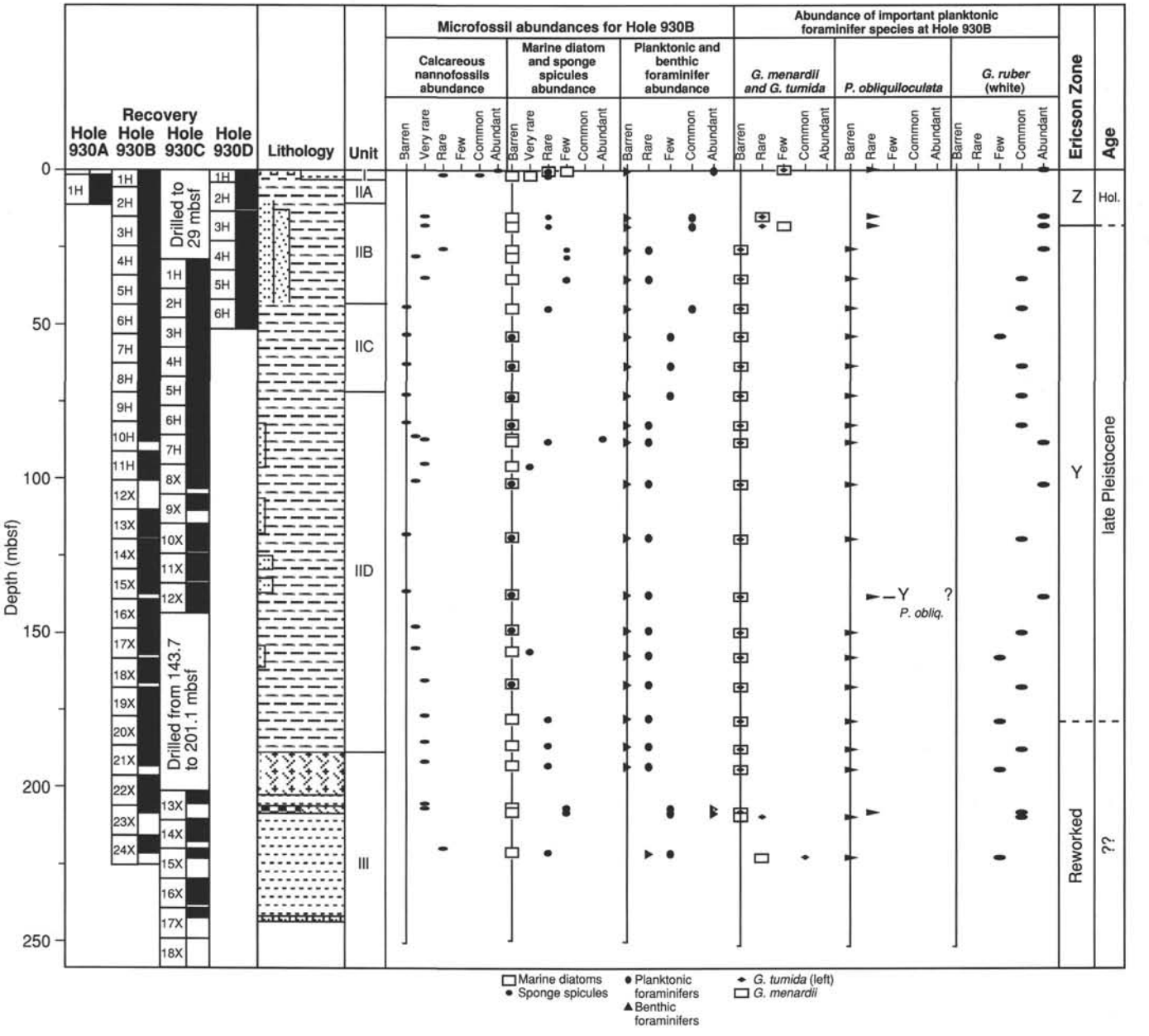

Figure 16. Biostratigraphic summary for Site 930.

Salinities of the water samples ranged from 35.5 to 31.5, though all but two samples are between 32 and 33. The maximum value is present in the shallowest sample (1.45 mbsf). Below this sample, salinity variations are minor with the exception of the sample at 220.10 mbsf, which has a slightly lower value of 31.5 (Fig. 24A).

Dissolved chloride values are initially near expected bottom water values, about 559 mM, and show a distinct increase with depth to 566 mM over the interval 22.65 41.65 mbsf (Fig. 24B). Thereafter, chlorinity decreases slightly downhole. A significant decrease to 532 mM occurs at 220 mbsf. Chlorinity of the deepest sample (241.10 mbsf) returns to near normal seawater values. The increase of chlorinity from 13.15 to 41.65 mbsf may reflect partially preserved glacial-age pore waters in the sediment. The sample at 220 mbsf also has lower salinity, pH, and magnesium concentrations, yet higher ammonium concentrations. The low concentrations may be due to pore-water dilution caused by melting of a clathrate layer.

Pore-water pH values range from 8.06 to 7.06. The values decrease with depth from 8.06 at 1.45 mbsf to 7.36 at 22.65 mbsf (Fig. 24C). Below 20 mbsf the values vary between 7.6 and 7.2, except for a value of 7.06 at 220.10 mbsf.

Observed changes in many of the other pore-water components reflect reactions directly or indirectly involving the oxidation of organic carbon within the sediment. In marine sediment, the oxidation of organic carbon is performed through a series of bacterially mediated reactions that utilize a series of different terminal electron acceptors. In general order of use, these are O_2, NO_3^-, MnO_2, FeOOH, SO_4^{2-}, and CO_2 (Froelich et al., 1979). Correspondingly, reaction products such as CO_2, NH_4^+, Mn^{2+}, Fe^{2+}, dissolved sulfide, and methane accumulate in the pore fluids and/or in solid phase precipitates. As discussed below, pore-water concentrations of various constituents are affected by these reactions.

Alkalinity in the pore-water samples has a total range of 5.9 to 18.5 mM. Alkalinity increases rapidly from the surface to 13.15 mbsf, where a maximum value of 18.5 mM is measured. Alkalinity then decreases quickly, to around 10 mM at 22.65 mbsf and in the underlying samples (Fig. 24D). The area of rapidly changing alkalinity val-

Table 4. Calcareous nannofossil and siliceous microfossil abundance data for Holes 930B and 930D.

Core, section, interval (cm)	Top interval (mbsf)	Bottom interval (mbsf)	Calcareous nannofossils			Diatoms		Sponge spicules	Radiolarians	Phytoliths	Ericson Zone	Age
			Abundance	Preservation	Zone	Marine	Freshwater					
155-930B-												
1H-MI, 0–0	0.00	0.00	a	g	CN15b	f	b	r	vr	b	Z	Holocene
1H-1, 6–7	0.06	0.07	a	g		r	b	r	vr	b	Z	Holocene
1H-1, 130–131	1.30	1.31	c	m		vr	b	r	tr	b	Z	?
1H-2, 23–24	1.73	1.74	r	p		b	b	r	b	b	Z	?
1H-CC, 28–29	5.42	5.72	vr–r	m		b	b	r	b	b	Z	?
2H-CC, 31–32	15.02	15.03	vr	p		b	b	r	b	b	Z	late Pleist.
3H-CC, 34–35	25.60	25.61	r	p		b	b	f	b	b	Y	late Pleist.
4H-3, 38–39	28.08	28.09	tr	p		b	b	f	b	b	Y	late Pleist.
4H-3, 40–41	28.10	28.11	tr	p		b	b	f	b	b	Y	late Pleist.
4H-3, 47–48	28.17	28.18	tr	p		b	b	f	b	b	Y	late Pleist.
4H-CC, 44–45	35.19	35.20	vr	p		b	b	f	b	b	Y	late Pleist.
5H-CC, 59–60	44.90	44.91	b	—		b	b	r	b	b	Y	late Pleist.
6H-CC, 94–95	53.84	53.85	b	—		b	b	b	b	b	Y	late Pleist.
7H-CC, 36–37	63.45	63.46	b	—		b	b	b	b	b	Y	late Pleist.
8H-CC, 41–42	73.11	73.12	b	—		b	b	b	b	b	Y	late Pleist.
9H-CC, 49–50	82.57	82.58	b	—		b	b	b	b	b	Y	late Pleist.
10H-4, 69–70	86.89	86.90	tr	p		b	b	a	b	b	Y	late Pleist.
10H-CC, 67–68	87.84	87.85	vr	p		b	b	r	b	b	Y	late Pleist.
11H-4, 42–43	96.12	96.13	vr	p		b	b	vr	b	b	Y	late Pleist.
11H-CC, 48–49	101.62	101.63	tr	p		b	b	b	b	b	Y	late Pleist.
13X-CC, 26–27	118.99	119.00	b	—		b	b	b	b	b	Y	late Pleist.
14X-CC, 39–40			b	—		b	b	b	b	b	Y	late Pleist.
15X-CC, 16–17	137.50	137.51	b	—		b	b	b	b	b	Y	late Pleist.
16X-CC, 17–18	149.28	149.29	tr	p		b	b	b	b	b	Y	late Pleist.
17X-CC, 22–23	156.03	157.04	tr	p		b	b	vr	b	b	Y	late Pleist.
18X-CC, 30–31	166.53	166.54	vr	p		b	b	b	b	b		
19X-CC, 40–41	178.05	178.06	vr	p		b	b	r	b	b	rw?	
20X-CC, 111–112	186.91	186.92	vr	p		b	b	r	b	b	rw?	
21X-CC, 19–20	193.28	193.29	vr	p		b	b	r	b	b	rw?	
22X-CC, 71–72	206.75	206.76	vr	p		b	b	f	b	b	rw?	
23X-CC, 33–34	208.46	208.47	vr	p		b	b	f	b	b	rw?	
24X-CC, 36–37	221.49	221.50	r	m	CN14b?	b	b	r	b	b	rw?	
155-930D-												
1H-M1, 0–0	0.00	0.00	a	g	CN15b	r	b	c	vr	b	Z	Holocene
1H-CC, 28–29	18.16	18.17	tr	p		b	b	b	b	b	Z	?
2H-CC, 31–32	15.02	15.03	b	—		b	b	b	b	b	Z	?
3H-CC, 34–35	25.60	25.61	b	—		b	b	b	b	b	Y	late Pleist.
4H-CC, 44–45	35.19	35.20	b	—		b	b	b	b	b	Y	late Pleist.
5H-CC, 59–60	44.90	44.91	tr	p		b	b	tr	b	b	Y	late Pleist.
6H-CC, 94–95	53.84	53.85	b	—		b	b	tr	b	b	Y	late Pleist.

ues is covered by only four samples, however, and much of the detail, including the alkalinity maximum, may not be captured in these data. This is also true of other pore-water constituents (calcium, magnesium, and phosphate) that show rapid concentration changes in the upper 10 to 20 mbsf. The rapid increase in the upper few meters is a response to organic carbon degradation reactions, primarily sulfate reduction, that produce alkalinity. The subsequent decrease probably reflects precipitation of diagenetic carbonate minerals (see below).

Pore-water magnesium concentrations decrease quickly from seawater values of 55 mM to a value around 40 mM by 13.15 mbsf (Fig. 24E). Deeper in the sediment, the concentration is fairly constant at 40 mM, with the exception of the sample collected at 220.10 mbsf, which has a value of 32.6 mM. Pore-water calcium concentrations show a profile similar to the magnesium concentrations (Fig. 24F). Values decrease quickly from seawater values of 10 mM, to around 5 mM at 13.15 mbsf, and are relatively constant with depth thereafter. The downcore decreases in calcium and magnesium occur in conjunction with the decrease in alkalinity, suggesting precipitation of carbonate minerals. Rapid sedimentation rates for this site (approximately 5 m/k.y.; see "Lithostratigraphy" section, this chapter), however, dilute authigenic mineral precipitation. Pore-water sulfate concentrations decrease rapidly from the top of the core downward (Fig. 24G). Sulfate concentrations are 23.9 mM at 1.45 mbsf, already below the seawater value of 28 mM. By 13.15 mbsf, sulfate has been completely removed from the pore fluids. Values remain essentially zero through the remainder of the core. The minor sulfate concentrations reported for depths below 13 mbsf are within the error of the analysis, with the possible exceptions of the samples at 124.25 and 220.10, where small sampling or sample-handling artifacts could exist. The near-surface depletion in pore-water sulfate indicates rapid organic carbon remineralization due to sulfate reduction. Bacterial sulfate reduction should result in increases in pore-water alkalinity in an approximately 1 to 2 stoichiometry. Thus, complete sulfate reduction should produce about a 50-mM increase in alkalinity. Such high values are not observed, however, because of carbonate precipitation.

Dissolved ammonium concentrations increase with depth from 0 mM at 1.45 mbsf to around 6 mM at 22.65 mbsf (Fig. 24H). Values remain about 6 mM from 22.10 to 182.70 mbsf, then increase to 9.8 mM at 220.65 mbsf.

The pore-water phosphate profile (Fig. 24I) parallels that of alkalinity. There is a rapid increase in dissolved phosphate to a sub-bottom maximum of 83 µM at 13.15 mbsf, followed by a rapid decrease to relatively constant values of just below 10 µM below 13.15 mbsf. The initial increase is due to the release of phosphate as organic material is remineralized. The subsequent decrease is likely due to precipitation of a phosphate-bearing mineral. This interpretation is supported by the presence of millimeter-sized nodules of vivianite that are common in the sediment.

Dissolved silica concentrations vary from 188 to 409 µM with no clear downhole trend (Fig. 24J). All the values are elevated above expected bottom-water values, which should be on the order of 50 µM. The higher pore-water values indicate minor dissolution of biogenic opal within the sediment.

The pore-water depth profile for potassium (Fig. 24K) is similar to the salinity profile. Concentrations are highest in the shallowest sample (13.1 mM at 1.45 mbsf), and decrease slightly with depth. Below 13.15 mbsf, potassium concentrations remain relatively constant between 6.6 and 9.3 mM, with the exception of a drop to 4.7 mM at 220.10 mbsf.

Concentrations of sodium range from 463 to 482 mM (Fig. 24L). The highest concentrations are measured in the shallowest samples. Below approximately 13.15 mbsf, there is a decrease to 479 mM. Below this, sodium varies little and exhibits no distinct downhole trend.

Dissolved iron concentrations are from 12.6 to 21.1 µM in the upper 13.15 mbsf, then quickly increase to 179.6 µM at 32.15 mbsf (Fig. 24M). Below this depth, values vary considerably, between 8.3

Table 5. Foraminifer abundance data for Holes 930B, 930C, and 930D.

Core, section, interval (cm)	Top interval (mbsf)	Bottom interval (mbsf)	*Globorotalia menardii*	*Globorotalia tumida* (left)	*Globorotalia tumida* (right)	*Globorotalia tumida flexuosa*	*Pulleniatina obliquiloculata*	*Globigerinoides ruber* (white)	*Globigerinoides ruber* (pink)	*Globorotalia hexagonus*	*Neogloboquadrina dutertrei*	*Globorotalia trilobus trilobus*	*Globorotalia inflata*	*Globorotalia truncatulinoides* (left)	*Globorotalia truncatulinoides* (right)	*Globigerina bulloides*	*Globigerinoides trilobus sacculifer*	*Globigerinoides ruber* (high)	*Orbulina universa*	*Globigerinita glutinata*	*Globigerinoides conglobatus*	*Globigerina calida*	*Neogloboquadrina pachyderma* (right)	*Neogloboquadrina pachyderma* (left)	*Globigerina quinqueloba*	*Globigerina rubescens*	*Globorotalia scitula*	*Globorotalia crassaformis*	Others	Overall foraminifer abundance	Preservation	Abundance of benthic foraminifers	Ericson Zone	Age
155-930B-																																		
1H-MI, 0–0	0.00	0.00	F	F	B	B	R	A	R	R	F	R	B	B	B	R	F	R	F	F	B	B	B	B	B	B	R		R	A	G	B	Z	Holocene
1H-CC, 19–28	5.42	5.72	F	R	R	B	R	A	F	R	F	F	R	B	F	R	F	R	R	F	F	B	B	B	B	B	R		B	C	M	B	Z	?
2H-CC, 22–31	14.93	15.02	R	R	B	B	R	A	F	R	F	F	R	R	R	B	F	B	R	R	B	R	B	B	B	B	B		F	C	G	B	Z	?
3H-CC, 25–34	25.51	25.60	B	B	B	B	B	A	R	B	C	C	B	B	B	B	F	B	R	B	R	B	B	B	B	B	B		R	R	M	B	Y	late Pleist.
4H-CC, 35–44	35.10	35.19	B	B	B	B	B	C	R	B	C	A	R	B	B	B	R	B	B	B	B	B	R	B	B	B	B		B	R	M	B	Y	late Pleist.
5H-CC, 50–59	44.81	44.90	B	B	B	B	B	C	R	B	C	C	B	B	R	B	R	B	R	B	B	B	B	B	B	B	B		B	C	G	B	Y	late Pleist.
6H-CC, 85–94	53.75	53.85	B	B	B	B	B	F	B	B	C	F	B	B	C	R	B	B	R	B	B	B	B	B	B	B	B		F	F	G	B	Y	late Pleist.
7H-CC, 27–36	63.36	63.45	B	B	B	B	B	C	R	B	C	F	R	B	C	B	B	B	B	B	B	B	B	B	B	B	B		F	F	G	B	Y	late Pleist.
8H-CC, 32–41	73.02	73.11	B	B	B	B	B	C	R	B	C	R	R	B	C	B	R	B	B	B	B	B	B	B	B	B	B		B	F	G	B	Y	late Pleist.
9H-CC, 40–49	82.48	82.57	B	B	B	B	B	C	R	B	C	R	B	B	C	B	R	B	B	B	B	B	B	B	B	B	B		B	R	G	B	Y	late Pleist.
10H-CC, 58–67	87.75	87.84	B	B	B	B	B	A	B	B	F	B	B	B	B	B	F	B	R	F	B	B	B	B	B	B	F		F	R	G	B	Y	late Pleist.
11H-CC, 39–48	101.53	101.62	B	B	B	B	B	A	B	B	C	B	B	B	B	B	B	B	B	B	B	B	B	B	B	B	B		B	R	P	B	Y	late Pleist.
13X-CC, 17–26	118.90	118.99	B	B	B	B	B	C	B	B	C	C	R	B	C	B	R	B	B	R	B	B	B	B	B	B	B		B	R	G	B	Y	late Pleist.
14X-CC, 30–39	129.8	129.3	B	B	B	B	B	A	R	R	F	C	R	B	C	B	R	B	B	F	B	B	R	B	B	B	R		F	R	G	B	Y	late Pleist.
15X-CC, 7–16	137.41	137.50	B	B	B	B	R	A	B	B	F	F	B	B	F	B	B	B	B	R	B	B	B	B	B	B	R		B	R	G	B	Y *P. obliq.*	late Pleist.
16X-CC, 8–17	149.19	149.28	B	B	B	B	B	C	R	B	R	R	B	B	C	B	R	B	B	R	B	B	B	B	B	B	B		B	R	G	B	Y	late Pleist.
17X-CC, 13–22	156.94	157.03	B	B	B	B	B	F	B	B	C	F	B	B	C	B	F	B	B	B	B	B	B	B	B	B	B		B	R	M	B	Y	late Pleist.
18X-CC, 21–30	166.44	166.53	B	B	B	B	B	C	B	B	C	C	B	B	B	C	B	B	B	B	B	B	B	B	B	B	B		B	R	M	B	Y?	late Pleist.
19X-CC, 31–40	177.96	178.05	B	B	B	B	B	F	R	B	C	C	B	B	F	B	B	B	B	B	B	B	B	B	B	B	B		B	R	G	B	Y?	late Pleist.
20X-CC, 102–111	186.82	186.91	B	B	B	B	B	C	R	B	C	F	B	B	C	B	F	B	B	B	B	B	B	B	B	B	B		B	R	P	B	Y?	late Pleist.
21X-CC, 10–19	193.19	193.28	B	B	B	B	B	F	B	B	C	R	B	R	C	B	R	B	R	B	B	B	B	B	B	B	B		B	R	M	R	RW	—
22X-CC, 62–71	206.66	206.75	B	B	B	B	R	C	B	B	C	C	B	B	C	B	R	B	B	B	B	B	B	B	B	B	B		B	F	M	A	RW	—
23X-CC, 24–33	208.37	208.46	B	R	B	B	B	C	B	B	C	F	B	B	C	B	B	B	B	B	B	B	B	B	B	B	B		B	F	M	A	RW	—
24X-CC, 27–36	221.40	221.49	R	C	B	R	B	F	B	B	C	F	B	B	B	B	R	B	R	B	B	B	B	B	B	B	B		B	F	G	R	RW/X?	—
155-930C-																																		
1H-CC, 34–43	39.29	39.38	B	B	B	B	R	C	B	B	F	C	B	B	B	B	C	B	B	B	B	B	B	B	B	B	B	B	B	B	R	M	B	Y	late Pleist.
2H-CC, 24–33	48.21	48.30	B	B	B	B	B	C	B	B	F	F	B	B	C	B	F	B	B	B	B	B	B	B	B	B	B	B	B	B	R	G	B	Y	late Pleist.
3H-CC, 21–30	58.17	58.26	B	B	B	B	B	F	R	B	C	F	B	B	C	B	F	B	R	B	B	B	B	B	B	B	B	B	B	B	R	G	B	Y	late Pleist.
4H-CC	67.39	67.48	B	B	B	B	B	C	R	B	C	F	B	B	C	B	R	B	R	B	B	B	B	B	B	B	B	B	R	R	F	G	B	Y	late Pleist.
5H-CC, 20–29	77.13	77.22	B	B	B	B	B	C	B	B	A	F	B	B	F	B	R	B	B	B	B	B	B	B	B	B	B	B	B	B	F	G	B	Y	late Pleist.
6H-CC, 18–27	86.62	86.71	B	B	B	B	B	C	B	B	A	F	B	B	F	B	F	B	B	B	B	B	B	B	B	B	B	B	B	B	F	G	B	Y	late Pleist.
7H-CC, 26–35	96.16	96.25	B	B	B	B	B	C	B	B	C	C	R	B	R	B	B	B	R	R	R	B	B	B	B	B	B	B	R	F	R	M	B	Y	late Pleist.
8X-CC, 9–18	103.00	103.09	B	B	B	B	B	C	B	B	F	C	B	B	C	B	B	B	B	B	B	B	B	B	B	B	B	B	B	B	R	M	B	Y	late Pleist.
9X-CC, 9–18	110.13	110.22	B	B	B	B	B	C	R	B	C	F	B	B	C	B	R	B	R	B	B	B	B	B	B	B	B	B	B	B	F	M	B	Y	late Pleist.
10X-CC, 31–40	123.49	123.58	B	B	B	B	B	F	B	B	C	C	B	B	C	B	F	B	B	R	R	B	B	B	B	B	B	B	B	R	R	M	B	Y	late Pleist.
11X-CC, 37–46	133.03	133.12	B	B	B	B	B	F	B	B	F	F	B	B	A	B	F	B	B	B	R	B	B	B	B	B	B	B	B	R	R	M	B	Y	late Pleist.
12X-CC, 18–27	142.10	142.19	B	B	B	B	B	C	R	B	F	C	B	R	R	B	B	B	B	B	B	B	B	B	B	B	B	B	B	B	R	G	B	Y	late Pleist.
13X-CC, 10–19	205.31	205.40	B	B	B	B	B	B	B	B	B	B	B	B	B	B	B	B	B	B	B	B	B	B	B	B	B	B	B	B	B	—	B	RW	—
14X-CC, 9–18	217.94	218.03	B	B	B	B	F	C	B	B	R	F	B	B	F	B	F	B	B	B	B	B	B	B	B	B	B	B	B	F	R	G	A	RW/Y *P. obliq.*	—
15X-CC, 28–37	223.37	223.46	B	R	B	B	F	F	B	B	F	C	B	B	B	B	B	B	B	B	B	B	B	B	B	B	B	B	B	B	R	M	A	RW	—
16X-CC, 25–34	237.14	237.23	B	R	B	B	B	C	B	B	C	F	B	B	F	B	B	B	B	B	B	B	B	B	B	B	B	B	B	R	R	M	A	RW	—
17X-CC, 31–40	242.80	242.89	B	B	B	B	B	B	B	B	B	B	B	B	B	B	B	B	B	B	B	B	B	B	B	B	B	B	B	B	R	M	B	RW	—
155-930D-																																		
1H-TOP			C	R	B	B	R	C	F	R	C	C	B	B	B	B	F	B	B	B	B	B	B	B	B	B	B	B	B	F	A	G	B	Z	Holocene
1H-CC, 7–16	3.93	4.02	R	R	B	B	R	F	B	B	C	C	B	B	R	B	F	B	R	B	B	B	B	B	B	B	B	B	B	F	R	M	B	Z	?
2H-4, 0–9	8.50	8.59	B	F	B	B	B	B	B	B	A	A	B	B	B	B	B	B	R	B	B	R	B	B	B	B	B	B	B	B	R	M	B	Z/Y	?
2H-CC, 12–21	12.60	12.69	B	B	B	B	B	A	B	B	A	A	B	B	B	B	B	B	R	B	B	B	B	B	B	B	B	B	B	B	R	M	B	Y	late Pleist.
3H-TOP	13.41	13.50	B	B	B	B	B	R	C	C	B	C	C	B	B	B	B	B	R	B	B	B	B	B	B	B	B	B	R	B	R	M	B	Y	late Pleist.
3H-CC, 27–36	23.74	23.83	B	B	B	B	B	B	B	B	C	C	B	B	B	B	C	B	B	B	B	B	B	B	B	B	B	B	R	B	R	M	B	Y	late Pleist.
4H-CC, 31–40	32.85	32.94	B	B	B	B	B	B	B	B	A	A	B	B	B	B	A	B	B	B	B	B	B	B	B	B	B	B	B	B	R	M	B	Y	late Pleist.
5H-CC, 21–30	42.50	42.59	B	B	B	B	B	F	B	B	A	F	B	B	B	B	C	B	B	B	B	R	B	B	B	B	B	B	B	F	R	M	B	Y	late Pleist.
6H-TOP	42.00	42.09	B	B	B	B	B	R	B	B	C	C	B	B	C	B	F	B	B	B	B	R	B	B	B	B	B	B	B	B	R	M	B	Y	late Pleist.
6H-CC, 24–33	52.05	52.14	B	B	B	B	B	F	R	B	C	C	B	B	C	B	R	B	R	B	B	B	B	B	B	B	B	B	B	B	C	M	B	Y	late Pleist.

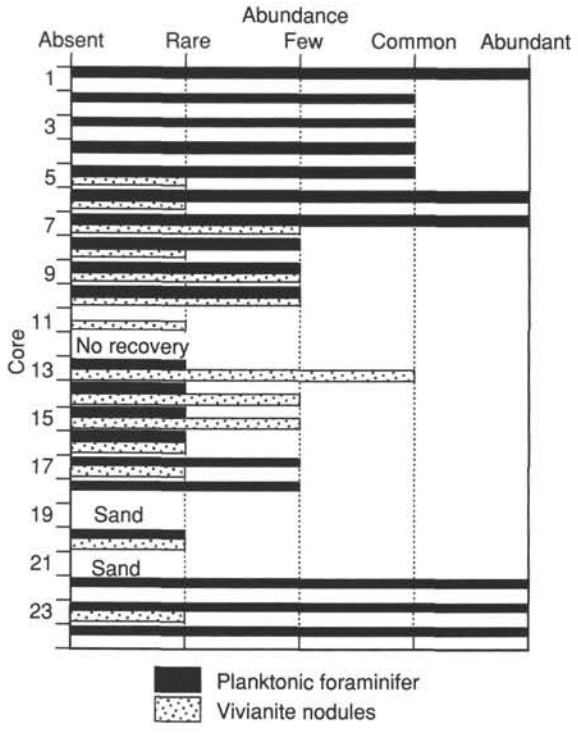

Figure 17. Vivianite and planktonic foraminifer abundances for Hole 930B.

and 119.7 µM, but show an overall trend of decreasing concentration downhole.

Pore-water manganese concentration is 11.3 µM at 1.45 mbsf. The values decrease to 2.4 µM at 13.15 mbsf, and range from 2.2 to 5.5 µM downhole (Fig. 24N).

PHYSICAL PROPERTIES

Index Properties

Index properties were measured for Holes 930A, 930B, and 930C (Table 10). Samples from Hole 930C were selected to fill in intervals that were not cored in Hole 930B.

Water content decreases downhole from 50% just below the seafloor to 25% at 190 mbsf. A change in gradient occurs in the interval between 92 and 111 mbsf. Over this interval water content increases by 6%. Differences in lithology, sedimentation rate, or consolidation behavior may be responsible for this increase. Below 190 mbsf, water content values vary considerably and are as low as 15% (Fig. 25). The dramatic change in water content at this depth correlates with the top of Unit III, a debris-flow deposit identified in Core 930B-22X. A similar decrease in water content between 126 and 129 mbsf corresponds to a thinner, suspected allochthonous block in Core 930B-14X.

Fluctuations similar to those of water content are evident in the wet-bulk density and porosity profiles (Fig. 25). The effect of the gas-induced sediment expansion is shown by the plot of the discrete-sample wet-bulk density profile and the GRAPE profiles (Fig. 26). For most of the section, the GRAPE bulk density is offset by densities 0.1 to 0.3 g/cm^3 lower than the discrete samples. Porosity values decrease gradually with depth from 75% near the seafloor to 50% at 190 mbsf. Below this depth, porosity values sharply decrease to about 35% at the base of hole. A slight decrease in wet-bulk density, 0.16 g/cm^3, and increase in porosity, 6%, occur at approximately 100 mbsf.

Grain density values are generally between 2.7 and 2.8 g/cm^3 (Fig. 25). Between 110 mbsf and 180 mbsf, grain density increases steadily from about 2.71 to 2.78 g/cm^3.

Compressional-wave Velocity

Compressional-wave velocity measurements were attempted on whole-round sections of cores using the *P*-wave logger (PWL) and on split sections using the DSV and the Hamilton Frame. Because gas expansion produced pervasive microfractures in the sediment, none of the techniques were capable of constantly transmitting an acoustic signal through the samples.

A few velocity results were obtained with the PWL in Hole 930B. Velocities ranging from 1400 m/s to 1960 m/s were obtained using only those values that had a strong transmittal signal (>100). Only 1.3% of the data met this criterion. These values are comparable to the layer velocities determined using wide-angle refraction data (see Table 10 in "Explanatory Notes" chapter, this volume).

Shear Strength

Undrained shear strength was measured using the motorized shear vane on most cores from Hole 930B and on selected sections of Hole 930C (Table 11). Below 158 mbsf, unconfined compressive strength was also measured to provide a comparison with undrained shear strength in anticipation that shear strengths would eventually exceed the capacity of the motorized shear vane. The shear-strength profile can be divided into four sections: 0 to 38 mbsf, 38 to about 100 mbsf, about 100 to 180 mbsf, and 180 mbsf to TD (Fig. 27). Between 0 and 38 mbsf undrained shear strength gradually increases from 9 to 20 kPa with little variability. Downhole from 38 mbsf the undrained shear strength increases from 15 to 61 kPa with a greater scatter in the

Table 6. Spores and pollen abundance data for Hole 930B.

Core, section, interval (cm)	Top interval (mbsf)	Bottom interval (mbsf)	Pollen and spores			Dinocysts	Wood/ carbonized particles	Ericson Zone (inferred from forams.)	Age (inferred from forams.)
			Abundance	Preservation	Major types recorded				
155-930B-									
1H-MI, 0–0	0.00	0.00	f	m	Gramineae, monolete spores	r	f	Z	Holocene
1H-CC, 28–29	18.16	18.17	a	g	Gramineae, Compositae, Labiatae, TCP, TP, SP, trilete, and monolete spores	b	a	Z	Holocene
6H-CC, 94–95	53.84	53.85	f	g	Euphorbiaceae, Cyatheaceae	r	f	Y	late Pleist.
7H-CC, 36–37	63.45	63.46	f	m	Euphorbiaceae, Cyperaceae, Cyatheaceae	b	c	Y	late Pleist.
8H-CC, 41–42	73.11	73.12	f	m	Cyatheaceae, monolete spores	r	f	Y	late Pleist.
11H-CC, 48–49	101.62	101.63	b			b	r	Y	late Pleist.
16X-CC, 17–18	149.28	149.29	a	m	Gramineae, TCP, Lycopodidae, Cyatheaceae, monolete spores	b	c	Y	late Pleist.
24X-CC, 36–37	221.49	221.50	r	m	Cyatheaceae	b	r		RW

Notes: TCP = tricolporate; TP = tricolpate; SP =stephanoporate type; RW = reworked.

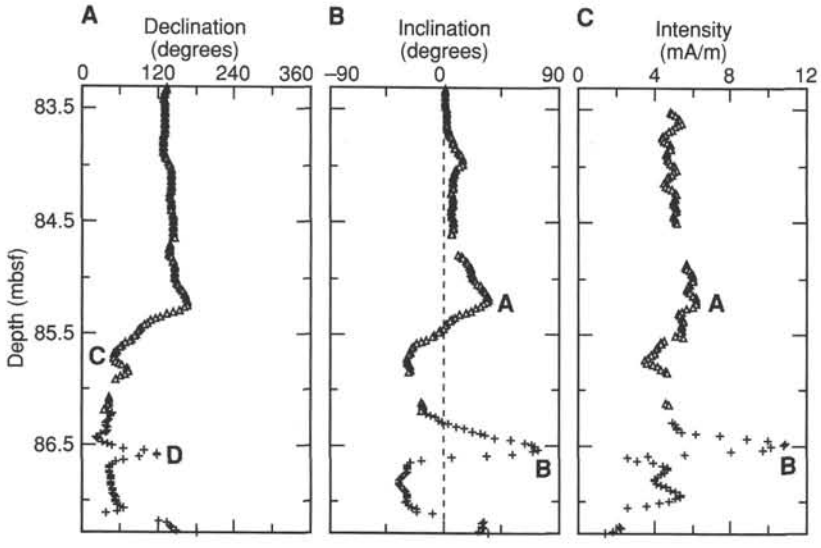

Figure 18. Uncorrected declination, inclination, and intensity for an apparent geomagnetic excursion (probably the Lake Mungo Excursion at ~30 ka) recorded in the archive half of Core 930B-10H. Measurement interval was 2 cm. Triangles = AF demagnetizations to 25 mT; crosses = AF demagnetizations to 26 mT. Erratic readings over gaps and core section breaks have been eliminated. See text for discussion of points A–D.

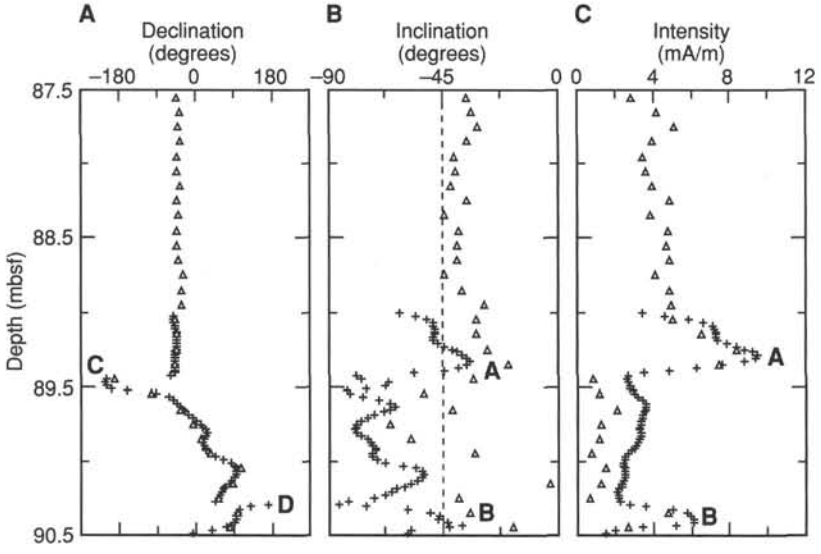

Figure 19. Declination, inclination, and intensity for an apparent geomagnetic excursion (probably the Lake Mungo Excursion at ~30 ka) recorded in the archive half of Core 930C-7H. Triangles = AF demagnetization to 25 mT; crosses = AF demagnetization to 26 mT. Note the effect of a small increase in demagnetization level on scale of inclination oscillations. See text for discussion of points A–D.

measurements. Below about 105 mbsf, measured values of undrained shear strength are between 20 and 180 kPa and are highly variable. At 180 mbsf the upper limit of the shear strength range increases rapidly, but values vary widely.

The major break at about 100 mbsf may be attributed to increased sediment disturbance accompanying the change from APC to XCB coring. However, change in water content, porosity, and density gradients at this depth also may reflect differences in sediment above and below the boundary. Below 100 mbsf shear strengths are lower and more variable. These changes are accompanied by increased frequency of shear vane failure at low strain angles (<15°). Failures at these angles imply that sediment is highly disturbed. However, the variation of index properties suggests that the change in shear strength is in part genuine.

The significant increase in shear strength below 180 mbsf correlates with lithologic Unit III, which is interpreted to be a series of debris-flow deposits and slide blocks. This unit contains the most consolidated sediment found at Site 930. This sediment is interbedded with weaker material that may be debris-flow matrix or material reworked by the coring process. There is a similar but very much smaller increase in undrained shear strength relating to the a suspected allochthonous block in Core 930B-14X (126 to 129 mbsf).

Resistivity

Longitudinal and transverse resistivity were determined for Holes 930A, 930B, and 930C (Table 12). Longitudinal resistivity increases downhole from 0.41 Ωm near the seafloor to 0.66 Ωm at the base of Hole 930C (Table 12). This increase corresponds with the downhole decrease in porosity. The variability in resistivity values increases below about 100 mbsf. Comparison of longitudinal and transverse resistivity values indicates no consistent trends in anisotropy.

Thermal Conductivity

Sediment thermal conductivity was measured on whole-core samples from Hole 930B and lower sections of Hole 930C (Table 13). A general linear trend exists between thermal conductivity and porosity for selected samples whose conductivity values are greater than 1.2 W/(m·K) and whose porosities are between 35% and 55% (Fig. 28). With increasing porosity, an associated decrease in thermal conductivity occurs as increased interstitial spacing attenuates the current. For porosities between 50% and 70% and thermal conductivities less than 1.2 W/(m·K), scatter precludes any relationship. The lack of a relationship is consistent with sediment fabric degradation by degas-

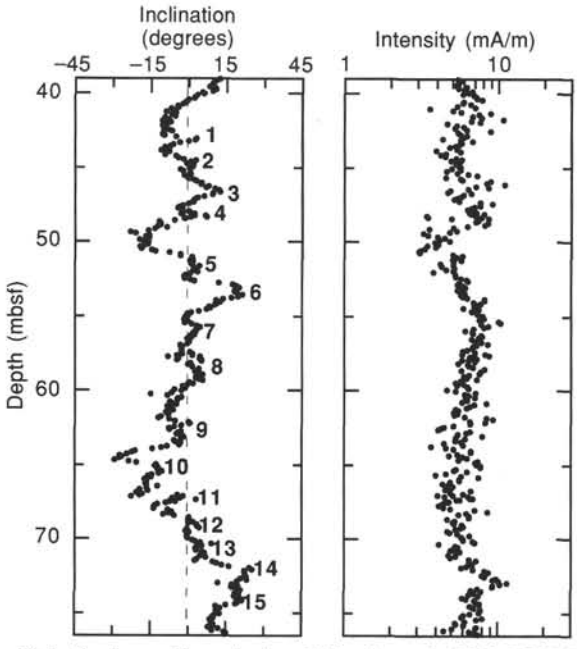

Figure 20. Inclination and intensity for a 37.5-m interval of Hole 930C. Measurement interval on these archive-half cores was 10 cm. Demagnetization level was 25 mT. Inclination cycles are numbered sequentially.

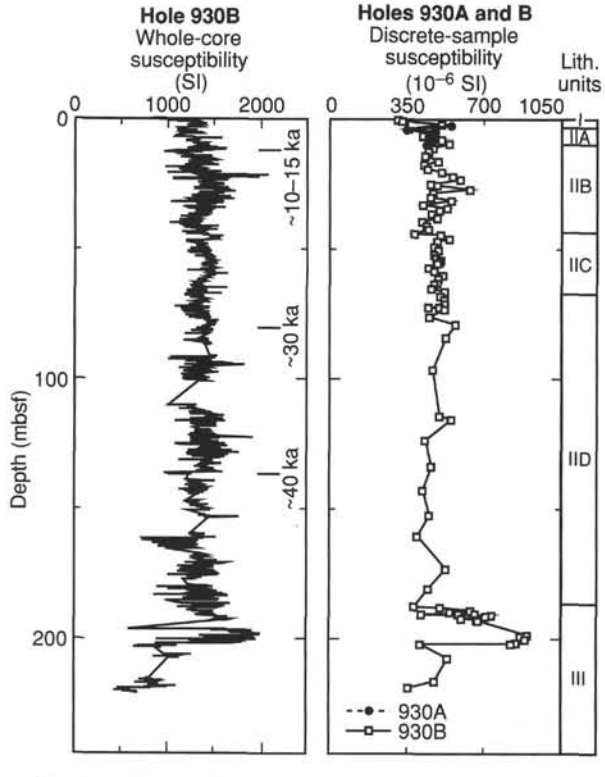

Figure 21. Downhole whole-core and discrete-sample susceptibilities for Holes 930A and 930B.

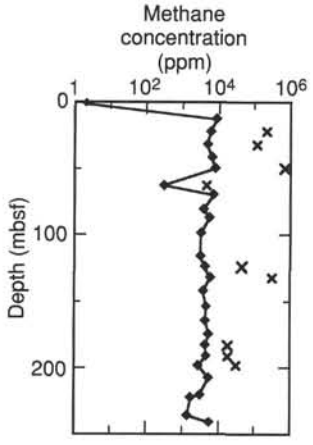

Figure 22. Methane concentrations (ppm) at Site 930. Headspace (diamond) and vacutainer (×) samples are plotted.

Table 7. Gas concentrations in sediments from Site 930.

Core, section, interval (cm)	Depth (mbsf)	Sed. temp.* (°C)	Methane HS (ppm)	Methane VAC (ppm)
155-930B-				
1H-2, 0–5	1.50	2	2	
2H-6, 0–5	13.20	2	8,737	
3H-6, 0–5	22.70	3	6,005	215,232
4H-6, 0–5	32.20	3	4,776	119,215
5H-6, 0–5	41.70	3	6,563	
6H-6, 0–5	49.90	4	8,002	724,708
7H-7, 84–89	63.04	4	296	4,656
8H-6, 0–5	70.25	4	7,185	
9H-7, 0–5	81.20		5	3,812
10H-CC, 0–5	87.17	5	5,540	
11H-6, 0–5	98.70	5	3,297	
13X-5, 0–5	116.20	6	3,075	
14X-4, 0–5	124.30	6	4,070	46,362
15X-3, 0–5	132.50	6	5,889	322,749
16X-3, 0–5	142.10	7	3,670	
17X-5, 0–5	154.21	7	4,620	
18X-5, 0–5	164.40	8	4,408	
19X-6, 0–5	174.83	8	5,243	
20X-5, 0–5	182.80	8	4,367	18,901
21X-4, 0–5	191.30	8	4,493	18,901
22X-2, 0–5	197.90	9	2,845	32,072
23X-2, 0–5	207.60	9	5,374	
24X-4, 0–5	220.20	9	3,070	
155-930C-				
15X-2, 0–5	221.90	9	1,665	
16X-5, 0–5	235.50	10	1,382	
17X-2, 0–5	241.20	10	5,729	

Notes: HS = headspace; VAC = vacutainer. Geothermal gradient = 34°C/km. Bottom-water temperature = 2°C. *See "In-situ Temperature Measurements" section, this chapter

sing. A few values plot within a region of low porosity (<45%) and low conductivity (<1.2 W/[m·K]), indicating a poor contact of the probe with the sediment.

CORE-SEISMIC INTEGRATION

Hole 930B was drilled to 241 mbsf and penetrated the levees of the Amazon, Brown, Aqua, Purple, Blue, Yellow, and crest of the Orange Channel-levee systems (Manley and Flood, 1988; Pirmez, 1994) (Figs. 29 and 2). Six discrete seismic-facies units, numbered 1 through 6, are observed in the top 300 ms of the seismic profile in the vicinity of Site 930 (Fig. 30). Five prominent moderate- to high-amplitude reflections bound these units at 40, 115, 130, 170, and 230 ms

Table 8. Elemental and organic carbon compositions of sediments from Site 930.

Core, section, interval (cm)	Depth (mbsf)	IC (%)	$CaCO_3$* (%)	TC (%)	TOC (%)	TN (%)	TS (%)	[C/N]a
155-930A-								
1H-2, 109–110	2.59	0.45	3.7	1.39	0.94	0.07	0.70	16
155-930B-								
1H-1, 17–18	0.17	3.88	32.3	4.23	0.35	0.04	0.26	11
1H-1, 39–40	0.39	3.31	27.6	3.58	0.27	0.04	0.21	7
1H-1, 110–111	1.10	0.20	1.7	0.86	0.66	0.06	0.19	12
1H-3, 63–64	3.63	0.19	1.6	1.12	0.93	0.08	0.69	13
2H-2, 39–40	7.59	0.23	1.9	1.21	0.98	0.09	0.15	13
2H-6, 89–90	14.09	0.24	2.0	1.13	0.89	0.11	0.30	10
4H-4, 96–97	30.16	0.22	1.8	1.17	0.95	0.10	0.20	12
5H-4, 96–97	39.66	0.06	0.5	0.82	0.76	0.08	0.09	11
5H-6, 99–100	42.69	0.22	1.8	1.20	0.98	0.09	0.00	13
6H-4, 20–21	47.90	0.32	2.7	1.16	0.84	0.08	0.09	12
6H-7, 41–42	51.81	0.19	1.6	1.10	0.91	0.08	0.10	13
7H-4, 97–98	58.67	0.23	1.9	1.11	0.88	0.08	0.10	13
7H-7, 24–25	62.44	0.18	1.5	1.08	0.90	0.07	0.09	14
8H-2, 80–81	65.00	0.20	1.7	1.06	0.86	0.08	0.08	13
8H-5, 80–81	69.50	0.21	1.7	1.09	0.88	0.08	0.09	12
8H-6, 25–26	70.50	0.22	1.8	1.11	0.89	0.08	0.21	13
9H-4, 45–47	77.15	0.21	1.7	1.09	0.88	0.09	0.08	12
9H-6, 116–118	80.86	0.20	1.7	1.11	0.91	0.08	0.00	14
10H-1, 80–81	82.50	0.18	1.5	1.06	0.88	0.08	0.05	13
10H-4, 35–36	86.55	0.20	1.7	1.10	0.90	0.09	0.07	12
11H-1, 55–56	91.75	0.35	2.9	0.99	0.64	0.06	0.00	13
11H-4, 115–116	96.85	0.25	2.1	1.12	0.87	0.07	0.10	15
13X-4, 62–63	115.32	0.25	2.1	1.03	0.78	0.07	0.09	12
13X-6, 40–41	118.10	0.29	2.4	1.13	0.84	0.08	0.08	13
14X-1, 44–45	120.24	0.29	2.4	1.11	0.82	0.08	0.19	12
14X-4, 79–80	125.09	0.17	1.4	0.63	0.46	0.04	0.08	15
15X-3, 50–51	133.00	0.19	1.6	0.89	0.70	0.06	0.10	14
15X-6, 29–30	137.29	0.29	2.4	1.08	0.79	0.06	0.08	14
16X-3, 52–53	142.62	0.23	1.9	1.13	0.90	0.08	0.09	13
16X-6, 60–61	147.20	0.45	3.7	1.35	0.90	0.08	0.08	13
17X-2, 89–90	150.60	0.22	1.8	1.09	0.87	0.07	0.08	14
17X-3, 50–51	151.70	0.23	1.9	1.47	1.24	0.17	0.83	9
17X-4, 41–42	153.12	0.24	2.0	1.13	0.89	0.10	0.23	11
17X-6, 50–51	156.21	0.21	1.7	1.10	0.89	0.10	0.14	10
18X-1, 50–51	158.90	0.30	2.5	1.15	0.85	0.10	0.10	10
18X-4, 107–110	163.97	0.33	2.7	1.22	0.89	0.10	0.09	11
19X-4, 32–33	172.15	0.27	2.2	1.15	0.88	0.10	0.07	10
19X-6, 96–97	175.79	0.23	1.9	1.10	0.87	0.09	0.09	11
20X-1, 40–41	177.60	0.33	2.7	1.20	0.87	0.12	0.06	9
20X-4, 10–11	181.40	0.26	2.2	1.07	0.81	0.09	0.08	10
21X-1, 124–125	188.04	0.16	1.3	0.75	0.59	0.06	0.22	11
21X-4, 55–56	191.85	0.23	1.9	1.03	0.80	0.09	0.12	11
22X-2, 50–52	198.40	0.16	1.3	0.80	0.64	0.09	0.08	8
22X-5, 86–87	203.26	0.14	1.2	0.97	0.83	0.15	1.12	7
22X-6, 50–51	204.40	0.30	2.5	1.13	0.83	0.13	0.23	7
23X-1, 144–145	207.54	0.27	2.2	1.01	0.74	0.15	0.00	6
24X-1, 34–35	216.04	0.22	1.8	0.89	0.67	0.13	1.04	6
24X-1, 85–86	216.55	0.25	2.1	0.89	0.64	0.13	0.20	6
155-930C-								
13X-1, 119–120	202.29	0.17	1.4	0.81	0.64	0.09	0.18	9

*Calculated assuming all IC is calcite.

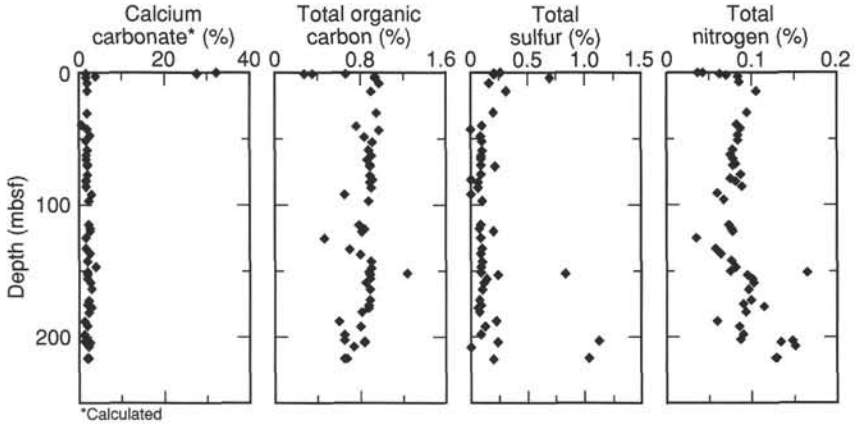

Figure 23. Concentration profiles of carbonate, total organic carbon, total sulfur, and total nitrogen in Hole 930B.

Table 9. Interstitial water chemistry, Site 930.

Core, section, interval (cm)	Depth (mbsf)	Salinity	pH	Alkalinity (mM)	Cl^- (mM)	Mg^{2+} (mM)	Ca^{2+} (mM)	K^+ (mM)	HPO_4^{2-} (μM)	SO_4^{2-} (mM)	NH_4^+ (mM)	H_4SiO_4 (μM)	Na (mM)	Fe^{2+} (μM)	Mn^{2+} (μM)
155-930A-															
1H-5, 145–150	7.45	33.0	7.81	14.56	563	40.1	4.7	9.4	20.1	0.10	4.18	357	475	89.0	2.6
155-930B-															
1H-1, 145–150	1.45	35.5	8.06	6.59	559	49.8	9.6	13.1	22.5	23.90	0.29	284	481	21.1	11.3
2H-5, 145–150	13.15	33.0	8.00	18.55	560	39.0	5.3	10.0	83.7	0.85	3.38	318	478	12.6	2.4
3H-5, 145–150	22.65	33.0	7.36	9.33	566	39.7	5.0	8.8	9.3	0.24	6.11	344	472	133.6	3.3
4H-5, 145–150	32.15	32.5	7.27	9.33	566	39.3	5.0	9.0	7.5	0.00	6.62	335	471	179.6	5.0
5H-5, 140–150	41.65	32.5	7.54	8.28	566	40.5	5.1	9.3	8.1	0.45	5.94	328	469	172.8	4.6
8H-5, 150–155	70.20	32.5	7.26	8.42	559	40.4	5.7	9.2	7.0	0.14	5.82	244	461	111.5	5.5
11H-5, 145–150	98.65	32.0	7.47	5.89	563	39.7	4.6	8.5	7.0	0.19	6.49	232	466	40.7	3.8
14X-3, 145–150	124.25	32.5	7.62	9.83	562	42.5	5.4	7.6	10.8	1.31	6.43	409	464	119.7	4.1
17X-4, 145–150	154.16	32.5	7.58	9.59	561	40.2	5.2	8.1	7.9	0.26	6.17	373	466	23.2	2.9
20X-4, 140–150	182.70	33.0	7.54	11.74	559	39.0	5.1	8.3	8.8	0.36	7.00	466	468	89.2	3.6
24X-3, 140–150	220.10	31.5	7.06	11.40	532	32.6	6.2	4.7	8.2	1.14	9.77	208	453	8.3	2.2
155-930C-															
17X-1, 140–150	241.10	32.5	7.72	11.10	558	38.2	5.7	6.6	8.8	0.69		188	476	9.1	2.9

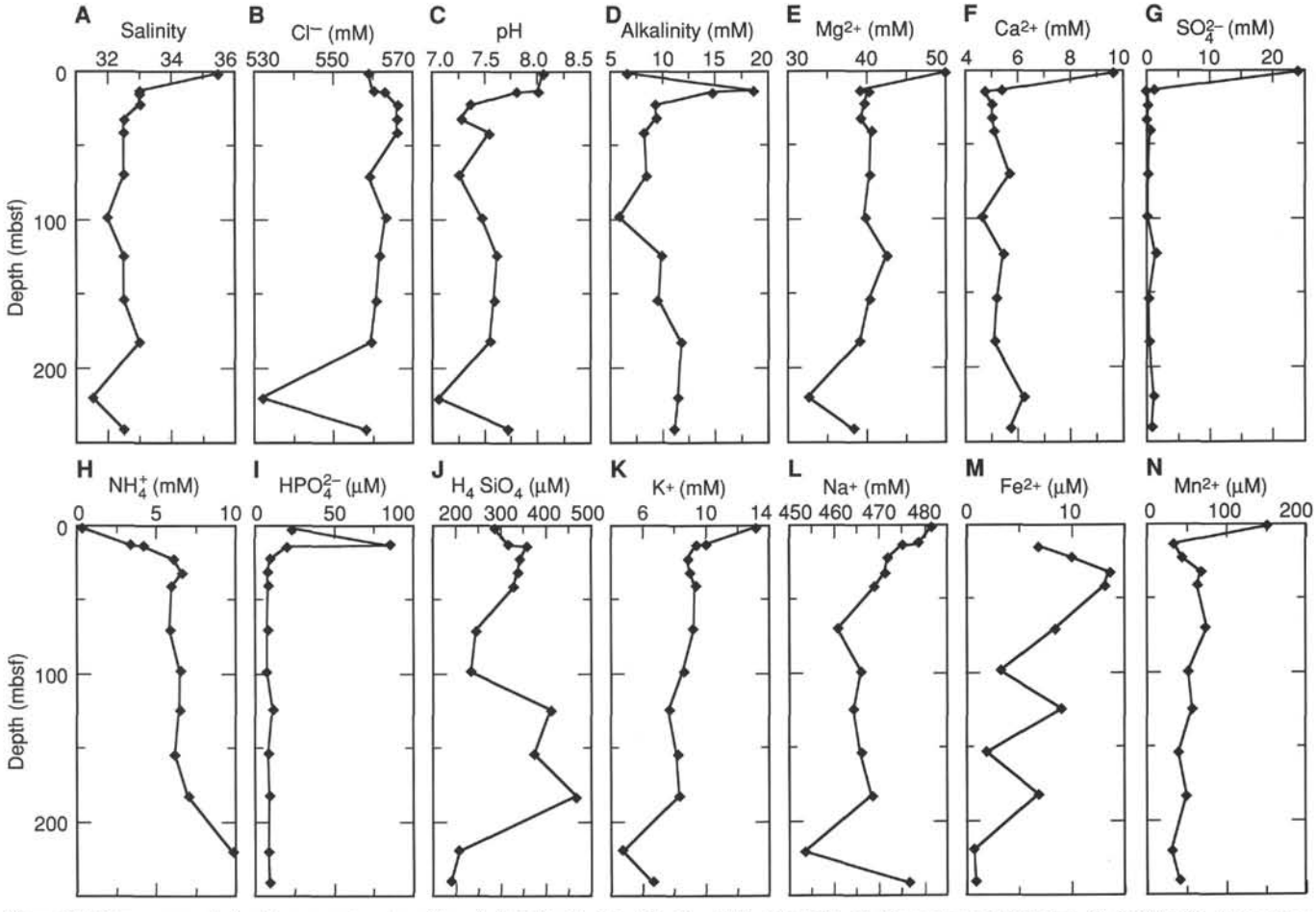

Figure 24. Downcore variation in pore-water chemistry. **A.** Salinity. **B.** Chloride. **C.** pH. **D.** Alkalinity. **E.** Magnesium. **F.** Calcium. **G.** Sulfate. **H.** Ammonium. **I.** Phosphate. **J.** Silica. **K.** Potassium. **L.** Sodium. **M.** Iron. **N.** Manganese.

sub-bottom. However, few of these reflections have been correlated regionally across the fan.

Echograms (3.5 kHz) were used to classify seismic-facies Unit 1 (0–40 ms), which thickens to the east and is characterized by continuous, subparallel, regular migrating reflections interpreted as sediment waves (Fig. 3). Seismic-facies Unit 2 (40–115 ms) is characterized by discontinuous, parallel reflections. The interface between seismic-facies Units 1 and 2 corresponds to a regional reflection at the base of the Aqua Channel-levee System (Fig. 30). Unit 2 thickens westward and corresponds to the Purple Channel-levee System. Continuous, parallel reflections from 115 to 130 ms sub-bottom characterize seismic-facies Unit 3 and are interpreted to represent sediment deposited when the Blue/Yellow Channel-levee systems were active. Seismic-facies Unit 4 (130 to 170 ms) returns continuous, subparallel, irregular reflections. The top of Unit 4 is interpreted as the top of the Orange Channel-levee System (Fig. 30). Seismic-facies Unit 5 (170 to 230 ms) is characterized by hummocky reflections. The lowermost section of the hole penetrates seismic-facies Unit 6, which is

Table 10. Index properties at Site 930.

Core, section, interval (cm)	Depth (mbsf)	Water content (%)	Wet-bulk density (g/cm^3)	Grain density (g/cm^3)	Dry-bulk density (g/cm^3)	Porosity (%)	Void ratio
155-930A-							
1H-2, 35–37	1.85	47.7	1.56	2.77	0.80	71.1	2.46
1H-4, 114–116	5.64	36.5	1.48	2.81	1.09	61.2	1.58
1H-6, 68–70	8.18	39.9	1.53	2.78	0.99	64.3	1.80
155-930B-							
1H-1, 32–34	0.32	50.2	1.52	2.81	0.75	73.5	2.77
1H-3, 38–40	3.38	47.9	1.57	2.78	0.79	71.4	2.50
2H-1, 131–133	7.01	42.3	1.65	2.77	0.93	66.4	1.98
2H-2, 81–83	8.01	35.0	1.79	2.77	1.13	59.3	1.46
2H-3, 46–48	9.16	42.3	1.66	2.78	0.93	66.6	1.99
2H-4, 71–73	10.91	41.6	1.66	2.78	0.95	65.9	1.93
2H-5, 46–48	12.16	39.0	1.67	2.75	1.01	63.2	1.72
2H-6, 72–74	13.92	37.2	1.73	2.75	1.06	61.4	1.59
3H-1, 90–92	16.10	38.3	1.70	2.72	1.03	62.2	1.65
3H-2, 33–35	17.03	37.9	1.70	2.74	1.04	62.0	1.63
3H-3, 33–35	18.53	38.3	1.71	2.71	1.03	62.2	1.64
3H-4, 98–100	20.68	38.1	1.74	2.75	1.04	62.3	1.65
3H-5, 48–50	21.68	36.0	1.78	2.77	1.10	60.3	1.52
3H-6, 93–95	23.63	32.0	1.86	2.73	1.21	55.6	1.25
3H-7, 38–40	24.58	36.0	1.74	2.74	1.09	60.1	1.50
4H-1, 70–72	25.40	36.3	1.75	2.78	1.09	60.7	1.55
4H-2, 93–95	27.13	33.7	1.81	2.75	1.16	57.7	1.37
4H-3, 37–39	28.07	35.1	1.79	2.76	1.12	59.3	1.45
4H-4, 127–129	30.47	36.5	1.74	2.81	1.09	61.2	1.58
4H-5, 69–71	31.39	34.7	1.81	3.02	1.18	61.0	1.57
4H-6, 84–86	33.04	35.6	1.78	3.07	1.15	62.3	1.66
4H-7, 38–40	34.08	34.4	1.82	2.67	1.13	57.8	1.37
5H-1, 55–57	34.75	34.0	1.79	2.83	1.17	58.8	1.42
5H-2, 117–119	36.87	34.9	1.80	2.76	1.13	59.1	1.45
5H-3, 85–87	38.05	34.8	1.82	2.82	1.14	59.5	1.47
5H-4, 98–100	39.68	36.6	1.76	2.80	1.09	61.2	1.58
5H-5, 85–87	41.05	35.1	1.77	2.78	1.13	59.5	1.47
5H-6, 11–13	41.81	34.5	1.80	2.76	1.14	58.7	1.42
5H-7, 101–103	44.21	34.2	1.81	2.79	1.16	58.6	1.41
6H-1, 124–126	44.94	34.2	1.80	2.75	1.15	58.3	1.40
6H-2, 126–128	46.46	33.4	1.82	2.79	1.18	57.8	1.37
6H-3, 80–82	47.50	37.9	1.73	2.80	1.05	62.5	1.67
6H-4, 41–43	48.11	32.6	1.86	2.74	1.19	56.4	1.29
6H-5, 69–71	49.09	34.0	1.81	2.97	1.19	59.8	1.49
6H-6, 76–78	50.66	33.0	1.84	2.88	1.21	58.1	1.39
6H-7, 108–110	52.48	32.8	1.82	2.86	1.21	57.7	1.36
7H-1, 74–76	53.94	32.7	1.84	2.81	1.21	57.1	1.33
7H-2, 117–119	55.87	32.3	1.85	2.73	1.20	55.9	1.27
7H-3, 83–85	57.03	30.9	1.86	2.82	1.27	55.2	1.23
7H-4, 13–15	57.83	31.8	1.83	2.82	1.23	56.2	1.28
7H-5, 92–94	60.12	31.2	1.87	2.84	1.26	55.7	1.26
7H-6, 38–40	61.08	32.0	1.83	2.71	1.21	55.4	1.24
7H-7, 82–84	63.02	31.6	1.84	2.70	1.22	54.9	1.22
8H-1, 120–122	63.90	32.3	1.90	2.74	1.20	56.1	1.28
8H-2, 100–102	65.20	33.3	1.85	2.66	1.16	56.4	1.29
8H-3, 105–107	66.75	31.7	1.84	2.68	1.21	54.8	1.21
8H-4, 95–97	68.15	32.0	1.83	2.67	1.20	55.1	1.23
8H-5, 95–97	69.65	30.5	1.89	2.68	1.25	53.4	1.15
8H-6, 95–97	71.20	30.8	1.88	2.70	1.24	54.1	1.18
8H-7, 41–43	72.16	31.8	1.86	2.70	1.21	55.1	1.23
9H-1, 85–87	73.05	32.4	1.85	2.73	1.20	56.1	1.28
9H-2, 110–112	74.80	31.1	1.86	2.68	1.23	54.1	1.18
9H-3, 90–92	76.10	30.8	1.89	2.72	1.25	54.2	1.18
9H-4, 95–97	77.65	30.9	1.90	2.80	1.26	55.1	1.23
9H-5, 68–70	78.88	30.2	1.90	2.69	1.26	53.2	1.14
9H-6, 35–37	80.05	30.2	1.88	2.70	1.26	53.3	1.14
10H-2, 42–44	83.62	30.3	1.90	2.77	1.27	54.1	1.18
10H-3, 46–48	85.16	30.5	1.88	2.71	1.26	53.7	1.16
10H-4, 45–47	86.65	29.5	1.88	2.75	1.29	53.0	1.13
11H-1, 41–43	91.61	27.0	1.97	2.71	1.37	49.5	0.98
11H-2, 43–45	93.13	28.7	1.94	2.73	1.32	51.7	1.07
11H-3, 90–92	95.10	27.8	1.99	2.70	1.34	50.4	1.02
11H-4, 30–32	96.00	27.9	1.98	2.69	1.33	50.3	1.01
11H-5, 40–42	97.60	29.6	1.91	2.72	1.29	52.7	1.12
11H-6, 35–37	99.05	29.9	1.94	2.75	1.28	53.4	1.14
13X-1, 102–104	111.22	32.9	1.81	2.72	1.18	56.6	1.30
13X-2, 98–100	112.68	30.4	1.85	2.69	1.25	53.5	1.15
13X-3, 106–108	114.26	28.0	1.93	2.71	1.33	50.8	1.03
13X-4, 107–109	115.77	29.5	1.91	2.71	1.29	52.6	1.11
13X-5, 107–109	117.27	30.3	1.88	2.70	1.26	53.4	1.14
13X-6, 72–74	118.42	29.6	1.90	2.74	1.29	52.8	1.12
14X-1, 141–143	121.21	29.0	1.88	2.72	1.31	52.1	1.09
14X-2, 102–104	122.32	27.7	1.95	2.72	1.35	50.3	1.01
14X-2, 140–142	122.70	29.3	1.88	2.73	1.30	52.4	1.10
14X-3, 113–115	123.93	31.0	1.87	2.74	1.24	54.7	1.21
14X-4, 133–135	125.63	30.2	1.87	2.71	1.26	53.4	1.15
14X-5, 45–47	126.25	27.1	2.01	2.78	1.38	50.3	1.01
14X-6, 132–134	128.62	25.8	2.03	2.78	1.43	48.5	0.94
14X-7, 17–19	128.97	26.5	2.00	2.76	1.40	49.2	0.97
15X-1, 22–24	129.72	29.9	1.91	2.81	1.30	53.9	1.17
15X-2, 121–123	132.21	29.5	1.93	2.77	1.30	53.1	1.13
15X-3, 73–75	133.23	29.4	1.88	2.75	1.30	52.8	1.12

Table 10 (continued).

Core, section, interval (cm)	Depth (mbsf)	Water content (%)	Wet-bulk density (g/cm^3)	Grain density (g/cm^3)	Dry-bulk density (g/cm^3)	Porosity (%)	Void ratio
15X-4, 122–124	135.22	28.8	1.92	2.77	1.32	52.2	1.09
15X-5, 59–61	136.09	30.3	1.88	2.76	1.27	54.0	1.17
15X-6, 6–8	137.06	31.1	1.85	2.78	1.25	55.1	1.23
16X-1, 131–133	140.41	30.6	1.87	2.78	1.27	54.4	1.19
16X-2, 47–49	141.07	27.8	1.95	2.77	1.36	51.0	1.04
16X-3, 28–30	142.38	28.1	1.92	2.82	1.36	51.8	1.08
16X-4, 82–84	144.42	28.5	1.92	2.78	1.34	52.0	1.08
16X-5, 72–74	145.82	28.5	1.92	2.76	1.33	51.8	1.08
16X-6, 112–114	147.72	28.6	1.92	2.80	1.34	52.3	1.10
16X-7, 76–78	148.86	27.4	1.97	2.79	1.37	50.7	1.03
17X-1, 34–36	149.04	28.0	1.99	2.79	1.35	51.4	1.06
17X-2, 127–129	150.98	28.5	1.93	2.79	1.34	52.0	1.08
17X-3, 66–68	151.87	27.8	1.93	2.78	1.36	51.1	1.05
17X-4, 101–103	153.72	28.6	1.92	2.76	1.33	51.9	1.08
17X-5, 137–139	155.58	27.7	1.94	2.77	1.36	50.9	1.04
17X-6, 100–102	156.71	26.4	1.99	2.80	1.41	49.4	0.98
18X-1, 113–115	159.53	27.1	1.96	2.79	1.39	50.3	1.01
18X-2, 87–89	160.77	28.1	1.93	2.79	1.35	51.5	1.06
18X-3, 26–28	161.66	28.3	1.95	2.78	1.34	51.8	1.07
18X-4, 66–68	163.56	29.4	1.91	2.81	1.31	53.3	1.14
18X-5, 42–44	164.82	26.8	1.99	2.80	1.40	49.9	1.00
18X-6, 25–27	166.15	28.9	2.07	2.80	1.33	52.6	1.11
19X-1, 41–43	168.41	27.4	1.99	2.79	1.38	50.7	1.03
19X-2, 104–106	169.87	26.2	1.98	2.77	1.41	49.0	0.96
19X-3, 42–44	170.75	26.7	1.97	2.78	1.40	49.7	0.99
19X-4, 81–83	172.64	26.9	1.99	3.02	1.45	52.0	1.08
19X-5, 45–47	173.78	26.8	1.98	2.83	1.41	50.2	1.01
19X-6, 56–58	175.39	26.5	1.99	2.86	1.43	50.2	1.01
19X-7, 9–11	176.42	27.3	1.99	2.77	1.37	50.4	1.02
20X-1, 97–99	178.17	25.8	2.01	2.79	1.44	48.6	0.95
20X-2, 37–39	178.67	27.0	1.99	2.76	1.38	49.9	1.00
20X-3, 47–49	180.27	28.7	1.93	2.79	1.33	52.4	1.10
20X-4, 132–134	182.62	26.4	1.96	2.81	1.42	49.6	0.98
20X-5, 87–89	183.67	25.9	1.97	2.73	1.41	48.3	0.93
20X-6, 132–134	185.62	26.3	1.95	2.75	1.40	48.9	0.96
21X-1, 88–90	187.68	29.6	1.90	2.82	1.31	53.6	1.15
21X-2, 106–108	189.36	25.7	1.95	2.72	1.42	47.9	0.92
21X-3, 114–116	190.94	23.6	2.03	2.73	1.50	45.1	0.82
21X-4, 120–122	192.50	22.0	2.06	2.73	1.56	42.9	0.75
22X-1, 63–65	197.03	20.1	2.09	2.73	1.63	40.1	0.67
22X-2, 74–76	198.64	19.2	2.12	2.71	1.67	38.6	0.63
22X-3, 66–68	200.06	19.2	2.15	2.74	1.68	38.8	0.63
22X-4, 75–77	201.65	19.4	2.14	2.71	1.66	39.0	0.64
22X-5, 84–86	203.24	21.0	1.64	2.75	1.61	41.7	0.71
22X-7, 68–70	205.22	17.4	1.85	2.76	1.76	36.2	0.57
23X-1, 128–130	207.38	17.3	1.89	2.76	1.77	36.0	0.56
24X-1, 51–53	216.21	17.6	1.89	2.75	1.75	36.5	0.58
24X-2, 61–63	217.81	16.0	1.90	2.75	1.82	33.9	0.51
24X-3, 31–33	219.01	17.4	1.90	2.75	1.76	36.2	0.57
24X-4, 35–37	220.55	19.4	1.80	2.75	1.67	39.2	0.65
155-930C-							
8X-1, 109–111	96.59	29.8	1.89	2.79	1.29	53.6	1.16
8X-2, 116–118	98.16	31.3	1.85	2.78	1.24	55.3	1.24
8X-3, 113–115	99.63	31.1	1.86	2.78	1.25	55.0	1.22
8X-4, 41–43	100.41	32.0	1.83	2.77	1.22	56.0	1.27
8X-5, 47–49	101.97	32.1	1.84	2.78	1.22	56.1	1.28
9X-1, 122–124	106.32	32.6	1.83	2.84	1.21	57.3	1.34
9X-2, 98–100	107.58	32.2	1.84	2.81	1.22	56.6	1.30
9X-3, 106–108	109.16	29.4	1.88	2.80	1.31	53.2	1.14
9X-4, 32–34	109.92	31.7	1.85	2.84	1.24	56.3	1.29
13X-1, 53–55	201.63	21.7	2.06	2.75	1.58	42.7	0.74
13X-3, 62–64	204.72	18.8	2.12	2.74	1.69	38.2	0.62
14X-1, 60–62	211.40	26.6	1.99	2.88	1.42	50.5	1.02
14X-2, 58–60	212.88	24.8	2.01	2.86	1.49	48.0	0.92
14X-3, 50–52	214.30	25.9	1.98	2.76	1.42	48.5	0.94
14X-4, 49–51	215.79	22.2	2.13	2.86	1.59	44.3	0.80
14X-5, 15–17	216.95	21.2	1.81	2.85	1.63	42.8	0.75
15X-1, 54–56	220.94	30.1	1.95	2.53	1.23	51.5	1.06
15X-2, 53–55	222.43	25.6	2.00	2.77	1.43	48.2	0.93
16X-2, 74–76	231.74	20.9	2.09	2.72	1.60	41.2	0.70
16X-3, 73–75	233.23	21.3	2.07	2.72	1.58	41.8	0.72
16X-4, 92–94	234.92	20.1	2.11	2.73	1.64	40.1	0.67
16X-5, 100–102	236.50	22.5	2.05	2.74	1.54	43.7	0.78
17X-1, 96–98	240.66	32.8	1.97	2.49	1.14	54.3	1.19
17X-2, 91–93	242.11	23.5	2.15	2.52	1.43	43.1	0.76

characterized by discontinuous, subparallel irregular reflections. Seismic-facies Units 4, 5, and 6 all occur within the Orange Channel-levee System.

The regional velocity profile derived from sonobuoy measurements did not give a satisfactory match between the core lithology and the seismic-facies units. For example, the abrupt change in lithology at 187 mbsf, associated with the top of mass transport deposits, should create a prominent reflection at 210 ms; however, no seismic horizon is observed at that depth (Fig. 30). A prominent reflection is observed at 230 ms that separates two seismic facies and contrasting lithologies. By forcing this reflection to align with the top of the debris-flow unit (lithostratigraphic Unit III), we determined a time-depth relationship with a seafloor velocity (V_0) of 1.6 km/s and a velocity gradient (k) of 0.5 km/s^2. This relationship puts the observed prominent reflections at depths of 35, 90, 105, 137, and 187 mbsf. The depths to these traveltimes change by a few meters if other rea-

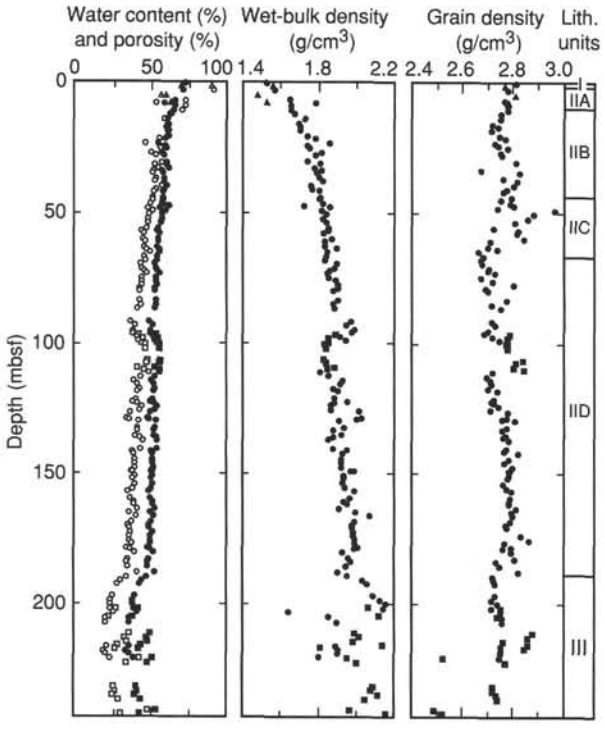

Figure 25. Water content (open symbols), porosity (solid symbols), wet-bulk density, and grain density in Holes 930A (triangles), 930B (circles), and 930C (squares).

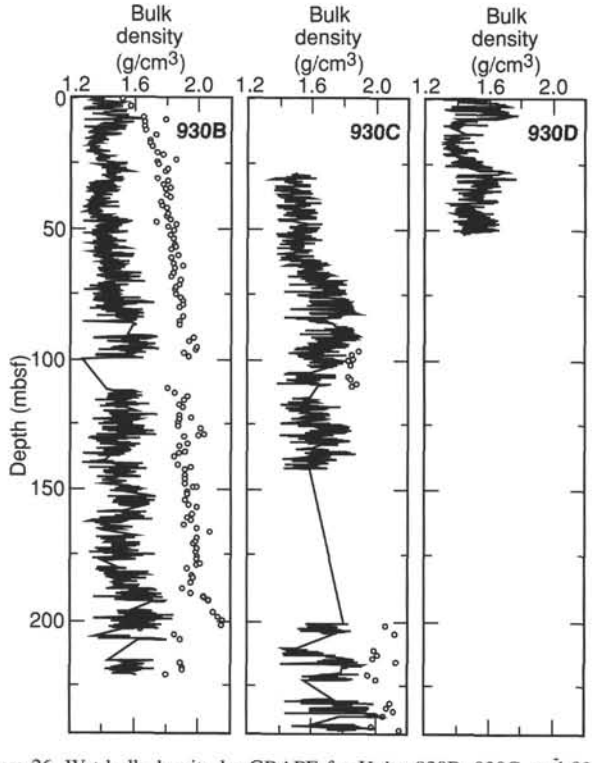

Figure 26. Wet-bulk density by GRAPE for Holes 930B, 930C, and 930D. Discrete-sample measurements of wet-bulk density (circles) for Holes 930B and 930C.

sonable velocity profiles are used. (e.g., the time-depth relationship determined at Site 931).

Not all seismic-facies units correspond directly to lithologic units. The regular migrating seismic facies of Unit 1 correlates with lithostratigraphic Subunit IIA and the upper 10 m of Subunit IIB. Internal acoustic reflections are most likely generated from thin sand and silt layers within migrating sediment waves. The discontinuous, parallel reflections of seismic-facies Unit 2 appear to encompass the lower part of Subunit IIB, all of Subunit IIC, and the upper 20 m of Subunit IID. This acoustic facies contains both laminated and bioturbated sediment. Seismic-facies Unit 3 correlates with the poorly sampled portion of lithostratigraphic Subunit IID from 90 to 105 mbsf, whereas seismic-facies Unit 4 correlates with the interval 105–138 mbsf within lithostratigraphic Subunit IID. Seismic-facies Unit 5 correlates with the lower 45 m of lithostratigraphic Subunit IID. Seismic-facies Unit 6 correlates with the mass-transport deposits (Fig. 30). Thus, the discontinuous, subparallel reflections of seismic-facies Unit 6 may be generated from the interfaces between the displaced slide blocks identified in lithologic Unit III.

IN-SITU TEMPERATURE MEASUREMENTS

In-situ temperature measurements were conducted to determine the geothermal temperature gradient and estimated heat flow at Hole 930B. These measurements aid in determining the conditions under which gas hydrates might occur and organic diagenesis takes place within the Amazon Fan.

Temperature gradients and heat flow were determined using three downhole measurements and the bottom-water (mud line) temperature. The measurements were taken using either the Advanced Piston Core (APC) heat-flow coring shoe (ADARA), used to obtain in-situ sediment temperatures during regular APC operations, or the Water-Sampler Temperature Probe (WSTP), which is a wireline tool that takes a temperature measurement between two piston-coring run operations (see "Explanatory Notes" chapter, this volume).

Two ADARA measurements were made in Hole 930B during Cores 930B-6H (at 53.2 mbsf) and -8H (at 72.2 mbsf) using instrument number 12. The mud-line temperature reading of 2.564°C from the ADARA instrument was used as the reference bottom-seawater temperature at Site 930. The in-situ measurement in Core 930B-6H was unsuccessful, possibly as a result of movement of the coring shoe, which created friction-induced temperature increases. A successful measurement in Core 930B-8H resulted in an extrapolated equilibrium temperature of 5.10°C at 72.2 mbsf. The 30-in. (0.76-m) WSTP tool, configured for temperature measurement only, was deployed at two depths in Hole 930B. WSTP measurements were made before Cores 930B-12X (at 100.7 mbsf) and -17X (at 148.7 mbsf) using probe thermistor number 108. Both measurements were successful and provided high-quality data. They yielded extrapolated equilibrium temperatures of 6.87°C at 100.7 mbsf (before Core 930B-12X), and 8.40°C at 148.7 mbsf (before Core 930B-17X). An offset of 1.185°C was applied to these equilibrium temperatures to correct for the difference in mud-line temperature recorded by the WSTP tool compared to that of the ADARA tools. We applied a correction of +1076 ohms to the raw resistance values recorded by the WSTP data logger. The WSTP values were corrected, rather than the ADARA values, because the ADARA instruments were more recently and precisely calibrated (see "Explanatory Notes" chapter, this volume).

Equilibrium temperatures, extrapolated from synthetic curves constructed to fit transient temperature data, are plotted as a function of depth (mbsf) in Figure 31. Using the ADARA mud-line temperature, and the sub-bottom temperatures from the one ADARA and two WSTP measurements downhole, the geothermal temperature gradient can be approximated by a linear mean of 31°C/km. We calculated heat flow by adopting a constant geothermal temperature gradient of

Table 11. Undrained shear strength at Site 930.

Core, section, interval (cm)	Depth (mbsf)	Unconfined compressive strength* (kPa)	Undrained shear strength (kPa)
155-930B-			
1H-1, 32	0.32		9.6
2H-3, 46	9.16		11.3
2H-3, 131	7.01		9.3
2H-4, 72	10.90		10.2
2H-5, 47	12.20		14.9
2H-6, 73	13.90		11.3
3H-2, 34	17.00		11.8
3H-3, 34	18.50		11.8
3H-4, 98	20.70		13.4
3H-5, 48	21.70		13.9
3H-7, 39	24.60		12.3
4H-1, 72	25.40		14.9
4H-2, 94	27.10		15.4
4H-3, 38	28.10		20.1
4H-4, 129	31.00		14.4
4H-5, 70	31.40		20.6
4H-6, 85	33.10		18.0
4H-7, 39	34.10		13.9
5H-1, 56	34.80		15.9
5H-2, 118	36.90		20.6
5H-3, 86	38.10		19.5
5H-4, 99	39.70		16.5
5H-5, 86	41.10		23.1
5H-6, 12	41.80		27.8
5H-7, 102	44.20		23.7
6H-1, 125	45.00		15.9
6H-2, 127	46.50		17.5
6H-4, 42	48.10		33.4
6H-5, 71	49.10		30.9
6H-6, 77	50.70		25.2
6H-7, 109	52.50		21.6
7H-1, 75	54.00		26.7
7H-2, 118	55.90		28.3
7H-3, 84	57.00		37.0
7H-4, 15	57.90		24.2
7H-5, 93	60.10		44.7
7H-6, 39	61.10		40.6
7H-7, 83	63.00		32.4
8H-1, 120	63.90		29.8
8H-2, 100	65.20		22.6
8H-3, 105	66.80		29.8
8H-4, 95	68.20		41.
8H-5, 95	69.70		38.1
8H-6, 95	71.20		33.9
8H-7, 41	72.20		26.2
9H-1, 85	73.10		38.9
9H-2, 110	74.80		33.6
9H-3, 90	76.10		41.5
9H-4, 95	77.70		39.8
9H-5, 68	78.90		42.4
9H-6, 35	80.10		37.1
10H-2, 44	83.60		55.7
10H-3, 46	85.20		58.3
10H-4, 45	86.70		45.1
11H-1, 41	91.60		61.0
11H-2, 43	93.10		53.9
11H-3, 90	95.10		47.7
11H-4, 30	96.00		39.8
11H-6, 35	99.10		38.0
11X-5, 40	97.60		61.0
13X-3, 106	114.00		33.6
13X-4, 107	116.00		30.1
13X-5, 107	117.00		19.4
14X-1, 142	121.00		38.0
14X-2, 141	123.00		31.8
14X-3, 114	124.00		23.9
14X-4, 134	126.00		38.9
14X-5, 46	126.00		29.2
14X-6, 133	129.00		39.8
14X-7, 18	129.00		42.4
15X-1, 23	130.00		23.9
15X-2, 122	132.00		35.4
15X-3, 74	133.00		38.9
15X-4, 123	135.00		31.8
15X-5, 60	136.00		23.0
16X-1, 132	140.00		22.1
16X-2, 48	141.00		30.1
16X-3, 29	142.00		50.4
16X-4, 83	144.00		38.9
16X-5, 73	146.00		30.1
16X-6, 113	148.00		42.4
17X-2, 128	151.00		33.6
17X-3, 67	152.00		46.0
17X-4, 102	154.00		54.8
17X-5, 138	156.00		61.0
17X-6, 101	157.00		71.6
18X-2, 88	161.00		51.3
18X-1, 114	160.00	98.0	44.2
18X-2, 90	162.00	112.7	
18X-3, 27	162.00	117.6	51.3
18X-4, 67	164.00	53.9	21.2
18X-5, 44	166.00	122.5	
18X-6, 26	166.00	53.9	36.2
19X-2, 105	170.00	68.6	26.5
19X-3, 43	171.00	98.0	38.0
19X-4, 82	173.00	68.6	25.6
19X-5, 46	174.00	68.6	31.8
19X-6, 57	175.00	107.8	53.0
19X-7, 11	178.00	102.9	
20X-1, 98	178.00	137.2	70.7
20X-2, 36	179.00	73.5	
20X-3, 48	180.00	73.5	34.5
20X-4, 133	183.00	98.0	47.7
20X-5, 88	184.00	127.4	47.7
20X-6, 123	186.00	73.5	38.9
21X-1, 88	188.00	127.4	36.2
21X-2, 106	189.00	156.8	52.2
21X-3, 114	191.00	181.3	72.5
21X-4, 120	193.00	186.2	71.6
22X-1, 65	197.00	166.6	
22X-2, 74	199.00	166.6	65.4
22X-3, 66	200.00	225.4	85.8
22X-4, 75	202.00	220.5	83.1
22X-5, 86	203.00	254.8	
22X-7, 68	205.00	294.0	113.2
23X-1, 129	207.00	367.5	181.2
24X-1, 52	216.00	274.4	66.3
24X-2, 62	218.00	318.5	103.4
24X-3, 32	219.00	254.8	
24X-4, 36	221.00	284.2	92.8
155-930C-			
8X-1, 110	96.60		29.2
8X-2, 117	98.17		42.4
8X-3, 114	99.64		43.3
8X-4, 42	100.42		53.0
8X-5, 48	101.98		35.4
9X-1, 123	106.33		24.8
9X-2, 99	107.59		36.2
9X-3, 107	109.17		34.5
9X-4, 33	109.93		31.8
13X-1, 53	201.63	151.9	
13X-3, 62	204.72	210.7	
14X-1, 60	211.40	215.6	3.5
14X-2, 58	212.88	308.7	87.5
14X-3, 50	214.30	171.5	
14X-4, 50	215.80	441.0	
14X-5, 15	216.95	318.5	
15X-1, 55	220.95	362.6	
15X-2, 53	222.43	240.1	
16X-2, 74	231.74	396.9	
16X-3, 74	233.24	367.5	
16X-4, 92	234.92	441.0	
16X-5, 100	236.50	441.0	
17X-1, 97	240.67	264.6	

Note: *Unconfined compressive strength (q_u) can be used to approximate undrained shear strength (S_u) by the relationship $q_u = 2S_u$.

31°C/km and a linear increase in thermal conductivity, K (as determined by the physical properties analyses), of 1.25 ± 0.15 W/(m·K) corresponding to the average depth of 100 mbsf. This results in a calculated heat flow of 38 mW/m^2. However, with regard to this heat flow calculation and those of other sites, it should be remembered that heat transfer can take place also by convection (such as pore-fluid advection), and that nonlinear variations in temperature with depth can vary depending on fluid advection processes and relative changes in the medium that the heat passes through (Carslaw and Jaeger, 1959; Menke and Abbott, 1990).

SYNTHESIS AND SIGNIFICANCE

Stratigraphic Synthesis

Surficial Nannofossil-Foraminifer Clay (Unit I)

At the mud line, 0.42 m of brown calcareous clay containing foraminifers and nannofossils (Fig. 32) overlies a brown diagenetic

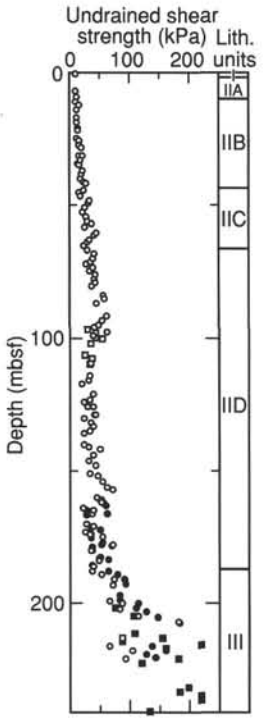

Figure 27. Undrained shear strength for Holes 930B (open circles) and 930C (open squares), and assumed undrained shear strength derived from unconfined compressive strength for Holes 930B (solid circles) and 930C (solid squares).

crust over about 0.13 m of nannofossil-rich clay. This sequence is defined throughout the region from previous piston core studies (Damuth, 1977). Because only core-catcher paleontological samples have been examined, the precise position of the base of the Holocene is uncertain. The base of the unit marks the time when terrigenous sediment supply to this part of the fan was sharply reduced as a result of rapidly rising sea level at the end of the last glacial.

Mud at Top of Levee Flank of Amazon Channel-levee System (Subunit IIA)

Subunit IIA comprises 8 m of mud with ephemeral color banding (dark/light couplets typically 8–12 mm thick), except that at the top of the unit the bands disappear and the core is intensely mottled, apparently a result of bioturbation. Foraminifers are relatively common throughout the unit. Similar lithologies are known from piston cores on levees on the upper fan and from levee flanks on the middle fan but are absent in piston cores from mid-fan levee crests and the lower fan (Flood et al., 1991). This subunit is thicker in Hole 930D on the crest of a sediment wave compared with Hole 930B on the adjacent flank, mirroring thickness variations in the underlying subunit of silt turbidites. This observation suggests that much of the deposition in Subunit IIA is in the form of gravity-driven downslope flows.

Levee Flank of the Amazon-Brown-Aqua Channel-levee System (Upper Part of Subunit IIB)

Subunit IIB consists of thin silt to silty sand beds alternating with mud. It was deposited on the levee flank of the late Pleistocene Amazon Channel system, and is largely equivalent to the Amazon, Brown, and Aqua intervals. Seismic correlation suggests that the base of this levee sequence is at 30 mbsf and that the deepest part of this subunit correlates with the Purple interval. Sedimentary structures suggest that the subunit consists largely of turbidites. Rare intervals contain disrupted bedding, with slightly elevated bulk density and strength, suggesting local slump deposits. Individual packets of beds can be correlated from Hole 930B on the flank of a sediment wave to Hole 930D on the adjacent crest, where the overall section is thicker and the proportion of sand is higher.

Mud and Silt Corresponding to the Purple, Blue, and Yellow Channel-levee System (Lower Subunit IIB to Upper Subunit IID)

Lower Subunit IIB through Subunit IID is stratigraphically equivalent to the Purple Channel (20 km distant), the Blue Channel (30 km distant), and the Yellow Channel (55 km). Much of this interval consists of mud, locally color banded or bioturbated, and silt laminae.

Tentative shipboard seismic correlation suggests that the Purple interval extends from the basal part of Subunit IIB to the upper 20 m of Subunit IID. A paleomagnetic excursion, correlated with the Lake Mungo Excursion (30 ka), is recognized at 86 mbsf.

Levee Crest of the Orange Channel-levee System (Lower Subunit IID)

Sediment of Subunit IID, corresponding to the levee crest of the Orange Channel-levee System, is lithologically similar to that of Subunit IIB, consisting of thin beds and laminae of silt and silty sand interbedded with mud. There are a few successions 1–2 m thick in which silts are almost absent. Two slumped masses are recognized from disrupted bedding and higher bulk densities. The lower part of this interval corresponds to the crest of the Orange levee. One specimen of *P. obliquiloculata* was found near the top of the Orange interval, indicating an age greater than 40 ka.

Debris-flow Deposit (Unit III)

Unit III comprises sandy mud (containing isolated pebbles, abundant plant debris, and mud clasts) interbedded with thick overconsolidated clay sequences. The clays contain mixed foraminiferal faunas including cool interstadial planktonic assemblages and upper-slope benthic assemblages. High total sulfur and nitrogen occur in this clay, and one pore-water sample showed unusual characteristics including low chlorinity. Seismic correlation suggests that the bottom of the hole was close to the base of this debris-flow unit.

Implications

Only coarse chronologic control is available from our shipboard studies at this site. The position of the Ericson Z/Y zonal boundary is not precisely located. The Lake Mungo paleomagnetic excursion at the top of Subunit IID is recognized in two holes at this site. The recognition of the *P. obliquiloculata* zonal boundary is based on a single specimen in an interval with very low foraminifer abundances. The lack of recovery of any microfossil-rich carbonate clays deep in the hole, however, suggests that no interglacial interval was penetrated.

These preliminary stratigraphic data indicate that the Upper Levee Complex formed largely or entirely during the last glacial period (oxygen isotopic Stages 2–4). Linear extrapolation of the tentative age datums in the holes suggests an age of about 50 ka for the debris flow at the base of the site (Fig. 32), that the Orange channel system was active around 40 ka (middle of oxygen-isotopic Stage 3), and the Purple channel system was active at less than 30 ka, late in oxygen-isotopic Stage 3.

Sedimentologic Implications

The typical 1- to 2-cm-thick silt or silty sand beds in Subunits IIB and IID appear to be turbidites. They have sharp bases and commonly grade up into mud with a bioturbated top. A few beds show partial

Table 12. Electrical resistivity at Site 930.

Core, section, interval (cm)	Depth (mbsf)	Longitudinal resistivity (Ωm)	Transverse resistivity (Ωm)
155-930A-			
1H-2, 37	1.87	0.412	0.331
1H-6, 70	8.20	0.412	0.350
1H-4, 111	5.61	0.376	0.331
155-930B-			
1H-1, 34	0.34	0.378	0.334
1H-3, 38	3.38	0.339	0.271
2H-1, 131	7.01	0.379	0.373
2H-3, 46	9.16	0.428	0.381
2H-4, 68	10.88	0.490	0.401
2H-5, 49	12.19	0.381	0.438
2H-6, 76	13.96	0.541	0.475
3H-1, 86	16.06	0.414	0.404
3H-2, 30	17.00	0.402	0.414
3H-3, 34	18.54	0.454	0.430
3H-4, 98	20.68	0.467	0.409
3H-5, 48	21.68	0.424	0.431
3H-7, 39	24.59	0.433	0.414
4H-1, 70	25.40	0.436	0.418
4H-2, 94	27.14	0.457	0.411
4H-3, 38	28.08	0.394	0.422
4H-4, 128	30.48	0.379	0.480
4H-5, 70	31.40	0.557	0.529
4H-6, 85	33.05	0.571	0.433
4H-7, 39	34.09	0.461	0.425
5H-1, 56	34.76	0.585	0.457
5H-2, 118	36.88	0.585	0.461
5H-3, 86	38.06	0.433	0.394
5H-4, 99	39.69	0.478	0.412
5H-5, 86	41.06	0.458	0.406
5H-6, 12	41.82	0.416	0.447
5H-7, 102	44.22	0.438	0.546
6H-1, 125	44.95	0.449	0.448
6H-2, 127	46.47	0.426	0.419
6H-3, 81	47.51	0.375	0.402
6H-4, 42	48.12	0.496	0.457
6H-5, 74	49.14	0.574	0.451
6H-6, 78	50.68	0.456	0.418
6H-7, 112	52.52	0.528	0.398
7H-1, 78	53.98	0.520	0.393
7H-2, 120	55.90	0.407	0.447
7H-3, 86	57.06	0.554	0.468
7H-4, 17	57.87	0.480	0.394
7H-5, 95	60.15	0.521	0.424
7H-6, 41	61.11	0.530	0.445
7H-7, 85	63.05	0.552	0.435
8H-1, 120	63.90	0.503	0.553
8H-2, 100	65.20	0.449	0.427
8H-3, 105	66.75	0.568	0.554
8H-4, 95	68.15	0.546	0.529
8H-5, 95	69.65	0.531	0.517
8H-6, 95	71.20	0.573	0.557
8H-7, 41	72.16	0.569	0.555
9H-1, 85	73.05	0.515	0.607
9H-2, 110	74.80	0.545	0.529
9H-3, 90	76.10	0.545	0.566
9H-4, 95	77.65	0.589	0.581
9H-5, 68	78.88	0.584	0.651
9H-6, 35	80.05	0.545	0.610
10H-2, 44	83.64	0.601	0.638
10H-3, 46	85.16	0.563	0.618
10H-4, 45	86.65	0.590	0.557
11H-1, 41	91.61	0.564	0.587
11H-2, 43	93.13	0.548	0.571
11H-3, 90	95.10	0.591	0.562
11H-4, 30	96.00	0.549	0.552
11H-5, 40	97.60	0.539	0.546
11H-6, 35	99.05	0.610	0.573
13X-1, 102	111.22	0.487	0.483
13X-2, 98	112.68	0.573	0.536
13X-3, 106	114.26	0.660	0.558
13X-4, 107	115.77	0.562	0.583
13X-5, 107	117.27	0.560	0.536
13X-6, 73	118.43	0.577	0.534
14X-1, 142	121.22	0.593	0.489
14X-2, 141	122.71	0.487	0.500
14X-3, 114	123.94	0.516	0.495
14X-4, 134	125.64	0.460	0.454
14X-5, 46	126.26	0.482	0.464
14X-6, 133	128.63	0.589	0.501
14X-7, 18	128.98	0.565	0.507
15X-1, 23	129.73	0.459	0.446
15X-2, 122	132.22	0.446	0.455
15X-3, 74	133.24	0.512	0.464
15X-4, 123	135.23	0.497	0.508
15X-5, 60	136.10	0.499	0.429
16X-1, 132	140.42	0.443	0.424
16X-2, 48	141.08	0.682	0.528
16X-3, 29	142.39	0.540	0.568
16X-4, 33	143.93	0.555	0.608
16X-5, 73	145.83	0.499	0.663
16X-6, 113	147.73	0.575	0.484
16X-7, 77	148.87	0.534	0.555
17X-1, 35	149.05	0.485	0.509
17X-2, 128	150.99	0.513	0.477
17X-3, 67	151.88	0.519	0.496
17X-4, 102	153.73	0.468	0.515
17X-5, 138	155.59	0.492	0.516
17X-6, 101	156.72	0.643	0.562
18X-1, 114	159.54	0.551	0.582
18X-2, 88	160.78	0.548	0.563
18X-3, 27	161.67	0.513	0.595
18X-4, 67	163.57	0.599	0.587
18X-5, 43	164.83	0.780	0.609
18X-6, 26	166.16	0.519	0.458
19X-2, 105	169.88	0.581	0.535
19X-3, 43	170.76	0.565	0.609
19X-4, 82	172.65	0.548	0.533
19X-5, 46	173.79	0.570	0.496
19X-6, 57	175.40	0.564	0.530
19X-7, 10	176.43	0.502	0.544
20X-1, 98	178.18	0.601	0.657
20X-2, 38	178.68	0.517	0.541
20X-3, 48	180.28	0.452	0.545
20X-4, 133	182.63	0.551	0.515
20X-5, 88	183.68	0.667	0.571
20X-6, 123	185.53	0.523	0.472
21X-1, 88	187.68	0.618	0.554
21X-2, 106	189.36	0.537	0.572
21X-3, 114	190.94	0.641	0.565
21X-4, 120	192.50	0.667	0.658
22X-1, 63	197.03	0.723	0.724
22X-2, 74	198.64	0.706	0.705
22X-3, 66	200.06	0.680	0.710
22X-4, 75	201.65	0.745	0.693
22X-5, 84	203.24	0.659	0.654
22X-7, 68	205.22	0.790	0.642
23X-1, 128	207.38	0.620	0.656
24X-1, 52	216.22	0.546	0.545
24X-2, 62	217.82	0.618	0.578
24X-3, 32	219.02	0.586	0.626
24X-4, 36	220.56	0.557	0.543
155-930C-			
8X-1, 110	96.60	0.537	0.489
8X-2, 117	98.17	0.579	0.530
8X-3, 114	99.64	0.545	0.506
8X-4, 42	100.42	0.549	0.442
8X-5, 48	101.98	0.505	0.474
9X-1, 123	106.33	0.503	0.454
9X-2, 99	107.59	0.523	0.460
9X-3, 107	109.17	0.497	0.528
9X-4, 33	109.93	0.483	0.464
13X-1, 53	201.63	0.708	0.683
13X-3, 62	204.72	0.709	0.680
14X-1, 60	211.40	0.597	0.524
14X-2, 58	212.88	0.664	0.579
14X-3, 50	214.30	0.744	0.766
14X-4, 50	215.80	0.732	0.708
14X-5, 15	216.95	0.545	0.548
15X-1, 55	220.95	0.563	0.553
15X-2, 53	222.43	0.572	0.567
16X-2, 74	231.74	0.718	0.679
16X-3, 74	233.24	0.811	0.786
16X-4, 92	234.92	0.771	0.805
16X-5, 100	236.50	0.703	0.781
17X-1, 97	240.67	0.510	0.548
17X-2, 91	242.11	0.657	0.638

Bouma sequences (T_b–T_d). Comparison of silt and sand beds from Subunit IIB shows that thicker and more frequent sand beds are deposited near the crest of the sediment wave than on the lower flank. This implies that substantial amounts of sand may bypass at least the proximal areas of the levee. Levee-crest silt and sand beds from the Orange system are more commonly lenticular or cross laminated than levee flank beds in Subunit IIB. Graded beds of interlaminated silt and mud (T3 of Stow and Shanmugam [1980]) are common. Small slump or debris-flow deposits are recognized in Subunits IIB and IID, from distorted bedding and physical properties that indicate slight overconsolidation. This is consistent with the frequent seismic evidence for slumps on levees on many modern deep-sea fans.

Table 13. Thermal conductivity at Site 930.

Core, section, interval (cm)	Depth (mbsf)	Thermal conductivity (W/[m·K])
155-930A-		
1H-1, 90	0.90	0.94
155-930B-		
1H-2, 90	2.40	1.01
1H-4, 45	4.95	1.08
2H-1, 85	16.05	0.92
2H-3, 75	18.95	0.96
2H-5, 91	22.11	1.20
2H-7, 65	24.85	0.83
3H-1, 50	25.20	1.02
3H-3, 50	28.20	1.05
3H-5, 50	31.20	1.08
3H-6, 50	32.70	0.96
4H-1, 73	34.93	0.97
5H-3, 53	37.73	0.97
5H-5, 58	40.78	1.12
5H-7, 68	43.88	0.89
6H-1, 50	44.20	0.76
6H-2, 50	45.70	1.06
6H-5, 53	48.93	1.06
6H-7, 53	51.93	0.97
7H-1, 50	53.70	1.13
7H-3, 50	56.70	1.01
7H-5, 50	59.70	1.26
7H-7, 50	62.70	0.93
8H-1, 55	63.25	0.98
8H-3, 55	66.25	0.97
8H-5, 55	69.25	1.16
8H-7, 55	72.30	0.88
9H-1, 95	73.15	0.90
9H-3, 95	76.15	0.91
9H-5, 95	79.15	1.06
9H-7, 50	81.70	1.18
10H-2, 50	83.70	1.14
10H-3, 50	85.20	1.15
10H-4, 50	86.70	1.26
11H-1, 40	91.60	1.01
11H-3, 37	94.57	1.19
11H-5, 39	97.59	1.09
11H-7, 45	100.65	1.35
11H-7, 45	100.65	1.35
13X-1, 100	111.20	1.05
13X-3, 100	114.20	1.16
13X-5, 98	117.18	1.09
14X-1, 45	120.25	1.08
14X-3, 65	123.45	1.31
14X-5, 43	126.23	1.06
14X-7, 45	129.25	1.43
15X-1, 52	130.02	1.10
15X-3, 52	133.02	1.30
15X-5, 52	136.02	1.11
16X-1, 50	139.60	0.96
16X-3, 50	142.60	0.96
16X-5, 50	145.60	1.10
17X-1, 45	149.15	1.12
17X-3, 40	151.61	1.27
17X-5, 45	154.66	1.42
18X-1, 60	159.00	0.93
18X-2, 85	160.75	1.06
18X-4, 85	163.75	1.04
18X-5, 95	165.35	1.03
19X-2, 45	169.28	0.98
19X-3, 45	170.78	1.10
19X-5, 45	173.78	1.11
19X-6, 45	175.28	1.28
20X-3, 40	180.20	0.96
20X-5, 20	183.00	1.14
20X-6, 85	185.15	1.12
21X-1, 75	187.55	1.12
21X-2, 75	189.05	1.12
21X-3, 75	190.55	1.49
21X-4, 75	192.05	1.49
22X-1, 110	197.50	1.53
22X-2, 110	199.00	1.32
22X-3, 110	200.50	1.65
22X-5, 110	203.50	1.16
24X-1, 50	216.20	1.03
24X-1, 75	216.45	1.27
24X-2, 75	217.95	1.19
24X-3, 75	219.45	1.05

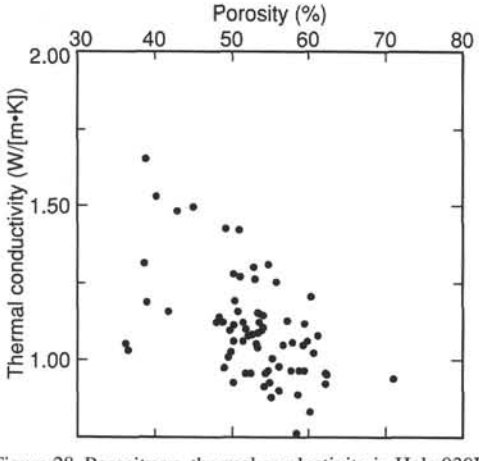

Figure 28. Porosity vs. thermal conductivity in Hole 930B.

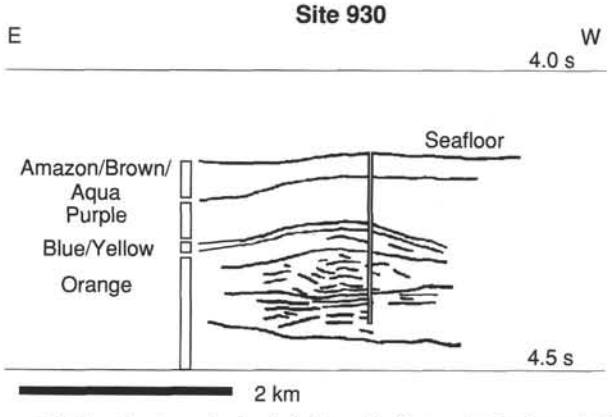

Figure 29. Line drawing of seismic-facies units from a single-channel seismic profile (*Conrad* C2514) in the vicinity of Site 930 (see Fig. 2).

The sedimentologic character of the thicker mud intervals (e.g., Subunits IIA, IIC) is difficult to determine from shipboard observations. In parts of this facies, a light-dark color banding on a 1-cm scale is visible. The darker bands resemble the muddy parts of graded silt to mud turbidites, whereas some of the light bands tend to be richer in nannofossils. Color banding is not present throughout the thick mud units, and some mottled parts of these units are clearly bioturbated. The observation that Subunit IIA varies in thickness from Hole 930B to 930D in the same manner as the turbidite Subunit IIB suggests that much of the thick mud section may consist of clay turbidites.

If the banding represents an annual feature, it implies peak sedimentation rates of 5–10 m/k.y., compared with a mean accumulation rate of 5.4 m/k.y. based on stratigraphic considerations. In this hypothesis, dark layers would correlate with peak Amazon River discharge (which currently occurs in May: Nittrouer et al. [1991]), either as discharge-related turbidity currents (as in the modern Zaire) or as settling from the river plume. The distinction between these hypotheses will be addressed at later sites and in shore-based studies.

It is unclear whether Unit III consists of a single blocky debris-flow deposit, or a series of debris-flow and interbedded slide deposits. The overconsolidation of the thicker mud sequences and the presence of iron-stained and calcified planktonic foraminifers, and upper slope benthic foraminifers suggest an original source for the debris flow on the continental slope. The sandy mud at the top of the debris-flow deposit probably masks the relief of any slide blocks, thus pos-

sibly accounting for the lack of hyperbolic diffractions at the top of this interval in the seismic profiles.

The thermal gradient is relatively low at Site 930 (31°C/km). Pore-water profiles show rapid concentration changes in the upper 20 mbsf, including complete sulfate reduction by 13 mbsf. Profiles of alkalinity, phosphate, calcium, and magnesium suggest that phosphate, calcium carbonate, and possibly a magnesium phase should be precipitated downcore. This may be represented in part by small, vivianite concretions.

Organic carbon content is remarkably uniform in Unit II, at about 0.8%, but does show a slight downhole decrease. Samples from the debris flow have higher total sulfur and nitrogen, suggesting a different source of organic matter. Pore water from a block in the debris flow at 220 mbsf has unusual composition including low chlorinity.

REFERENCES*

Carslaw, H.S., and Jaeger, J.C., 1959. *Conduction of Heat in Solids* (2nd ed.): Oxford (Clarendon Press).

Curry, W.B., Shackleton, N.J., Richter, C., et al., in press. *Proc. ODP, Init. Repts.*, 154: College Station, TX (Ocean Drilling Program).

Damuth, J.E., 1977. Late Quaternary sedimentation in the western equatorial Atlantic. *Geol. Soc. Am. Bull.*, 88:695–710.

Flood, R.D., Manley, P.L., Kowsmann, R.O., Appi, C.J., and Pirmez, C., 1991. Seismic facies and late Quaternary growth of Amazon submarine fan. *In* Weimer, P., and Link, M.H. (Eds.), *Seismic Facies and Sedimentary Processes of Submarine Fans and Turbidite Systems:* New York (Springer-Verlag), 415–433.

Froelich, P.N., Klinkhammer, G.P., Bender, M.L., Luedtke, N.A., Heath, G.R., Cullen, D., Dauphin, P., Hammond, D., Hartman, B., and Maynard, V., 1979. Early oxidation of organic matter in pelagic sediments of the eastern equatorial Atlantic: suboxic diagenesis. *Geochim. Cosmochim. Acta,* 43:1075–1090.

Manley, P.L., and Flood, R.D., 1988. Cyclic sediment deposition within Amazon deep-sea fan. *AAPG Bull.*, 72:912–925.

Menke, W., and Abbott, D., 1990. *Geophysical Theory:* New York (Columbia Univ. Press).

Nittrouer, C.A., DeMaster, D.J., Figueiredo, A.G., and Rine, J.M., 1991. AmasSeds: an interdisciplinary investigation of a complex coastal environment. *Oceanography,* 4:3–7.

Pirmez, C., 1994. Growth of a submarine meandering channel-levee system on the Amazon Fan [Ph.D. thesis]. Columbia Univ., New York.

Stow, D.A.V., and Shanmugam, G., 1980. Sequences of structures in fine-grained turbidites: comparison of recent deep-sea and ancient flysch sediments. *Sediment. Geol.*, 25:23–42.

Stupavsky, M., and Gravenor, C.P., 1984. Paleomagnetic dating of Quaternary sediments: a review. *In* Mahaney, W.C. (Ed.), *Quaternary Dating Methods:* Amsterdam (Elsevier).

van Morkhoven, F.P.C.M., Berggren, W.A., and Edwards, A.S., 1986. Cenozoic cosmopolitan deep-water benthic foraminifera. *Bull. Cent. Rech. Explor.-Prod. Elf-Aquitaine,* Mem. 11.

*Abbreviations for names of organizations and publications in ODP reference lists follow the style given in *Chemical Abstracts Service Source Index* (published by American Chemical Society).

Ms 155IR-106

NOTE: For all sites drilled, core-description forms ("barrel sheets") and core photographs can be found in Section 4, beginning on page 703. Forms containing smear-slide data can be found in Section 5, beginning on page 1199. GRAPE, index property, magnetic susceptibility, and natural gamma data are presented on CD-ROM (back pocket).

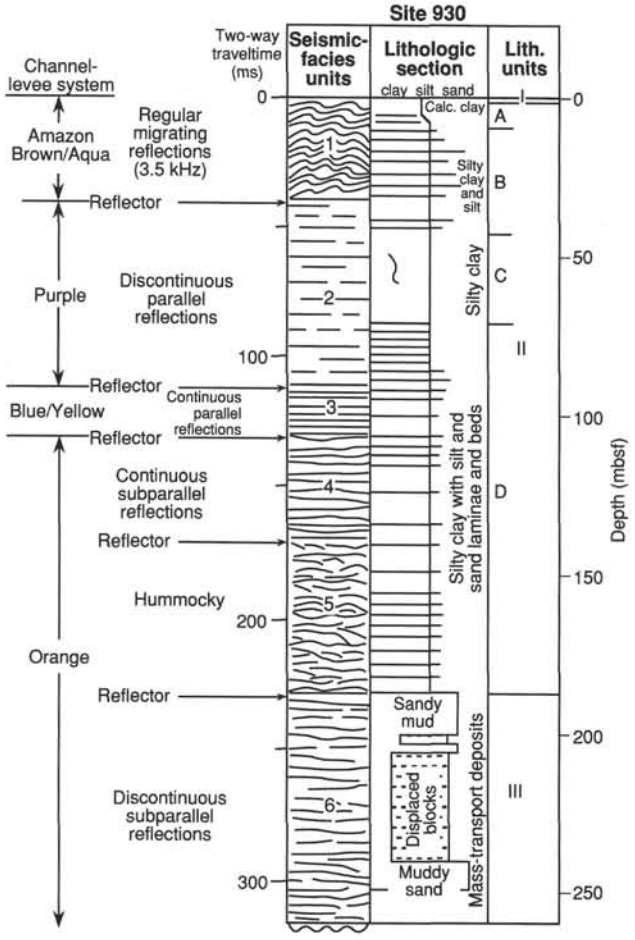

Figure 30. Correlation of lithostratigraphic observations with seismic-facies units and prominent reflections (arrows) at Site 930.

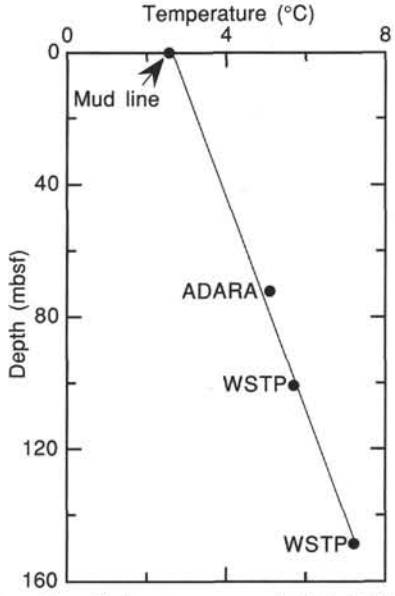

Figure 31. Estimated equilibrium temperatures in Hole 930B. A linear curve fit through the data suggests that reliable equilibrium temperatures were acquired that indicate a geothermal temperature gradient of 31.06°C/km.

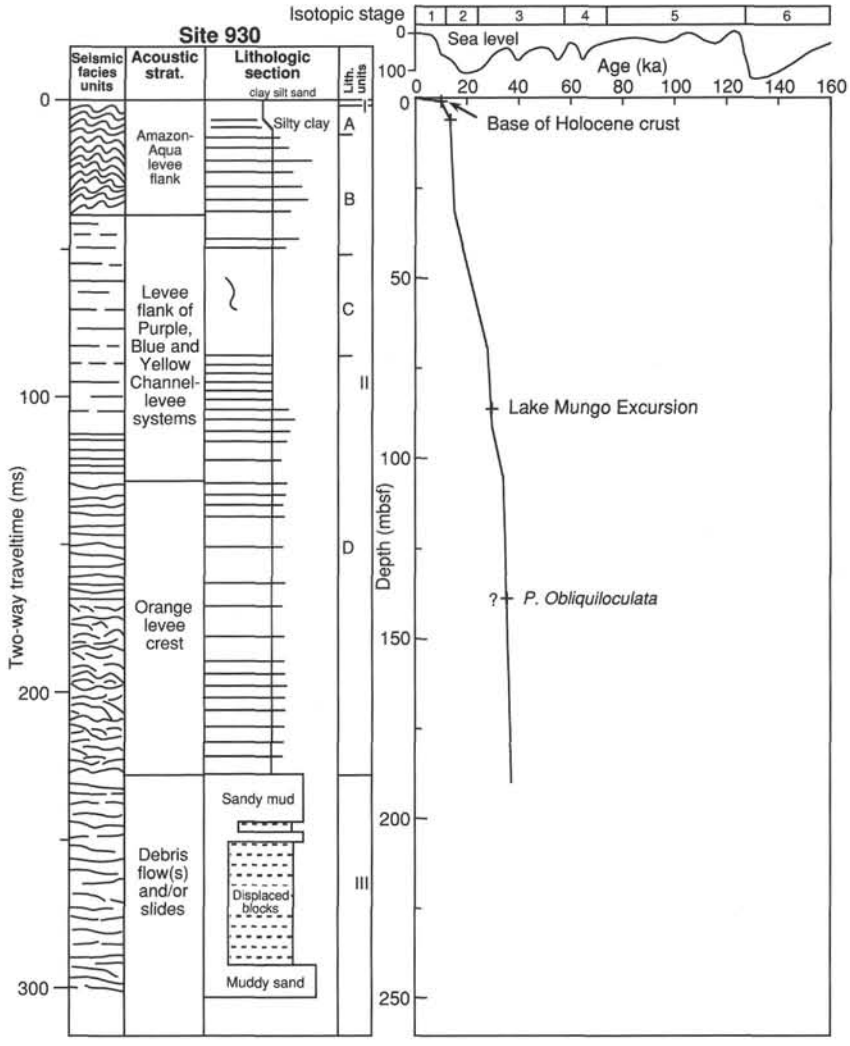

Figure 32. Summary figure showing seismic facies units, acoustic stratigraphy, schematic lithologic column, lithologic units, chronological picks, and interpreted age-depth curve.